# Exploiting Inherent Magnetic Signatures of Ferromagnetic Objects for Detection, Identification, and Position Estimation Applications

A Dissertation
SUBMITTED TO THE FACULTY OF THE GRADUATE SCHOOL
OF THE UNIVERSITY OF MINNESOTA
BY

Saber Taghvaeeyan

IN PARTIAL FULFILLMENT OF THE REQUIREMENTS
FOR THE DEGREE OF
DOCTOR OF PHILOSOPHY

Advisor: Professor Rajesh Rajamani

June 2014

## Acknowledgements

First and foremost, I wish to express my gratitude to my advisor, Prof. Rajesh Rajamani, for his continuous support and guidance throughout my doctoral study. The work presented in this dissertation would not have happened without his patience and motivation. I am especially thankful to him for his book, Vehicle Dynamics and Control, which I read during my undergraduate study through which I came to know about his research at the University of Minnesota.

I am grateful to Prof. William Durfee, Prof. Demoz Gebre-Egziabher, and Prof. Zongxuan Sun for their valuable feedback and help by serving in my preliminary oral exam and PhD defense committees. I am especially thankful to Prof. Sun for letting me use the free piston engine setup in his lab.

My further gratitude goes to Lee Alexander for his help and suggestions in developing prototypes, and Mike Gust for his help and valuable advice towards commercializing our piston position estimation system. I am thankful to my past and current lab-mates: Dr. Gridsada Phanomchoeng, Dr. Peng Peng, Dr. Kalpesh Signal, Shan Hu, Garret Nelson, Mahdi Ahmadi, Song Zhang, Ryan Madson, Woongsun Jeon, and Ye Zhang. I am also thankful to Ke Li for his help with the free piston engine experiments and Hamid Mokhtarzadeh for the academic and non-academic discussions we shared. I would like to extend special thanks to my great friends in Minneapolis and especially my first roommate, Sepehr Salehi, and his family for their help and support upon my arrival in Minneapolis.

Finally, and most importantly, I would like to thank my family for their unconditional support and undying love. I thank my parents for raising me with a passion to learn, and for motivating and encouraging me throughout my studies. I thank my brothers, Saleh and Sadegh, my sister-in-law, Khatoon, my uncle and aunt, Mahmood and Sandy Akhavan, and the rest of my family for their kindness and support. Finally, I

thank the love of my life, Golshan, the foundation of my strength, and my best friend and companion. Without her endless patience and encouragement, I would have never completed this work.

# Dedication

*To my dear parents, Aliakbar and Mahboubeh,*

*and to my lovely wife, Golshan.*

## Abstract

Many creatures in nature, such as butterflies, newts and mole rats, use the Earth's inherent magnetic field for navigation. They use magnetic field lines and magnetic field intensity variations to determine their geographical position. In this thesis, similar techniques are developed to measure the positions of individual ferromagnetic objects found all around us in everyday life. Ferromagnetic objects have inherent magnetic fields around them. It is shown here that the magnetic field variation around a ferromagnetic object can be modeled using purely the geometry of the object under consideration. Exploiting this model of the inherent magnetic field, the position of the object can be measured accurately using a small inexpensive magnetic sensor. Further, the use of one or more additional (redundant) sensors and adaptive estimation algorithms eliminates the need for pre-calibration of the measurement system. The significance and applicability of this new sensing principle is shown through three major applications: 1) Imminent automotive crash detection, 2) Non-intrusive piston position estimation, and 3) Portable road-side sensor for vehicle counting, speed measurement, and classification.

The work on imminent automotive crash detection is motivated by the need to develop an inexpensive sensor system for an automobile that can predict an imminent collision with another vehicle just before the collision occurs. The prediction needs to occur at least 100 milliseconds before the collision so that there is adequate time to initiate active occupant protection measures during the crash. A vehicle is made of many metallic parts (such as chassis, engine, and body) which have a residual magnetic field and/or get magnetized in the Earth's magnetic field. These magnetic fields create a net magnetic field for the whole vehicle which can be analytically modeled as a function of 2-D position around the vehicle. While this model can be used to estimate position and orientation, a challenge is posed by the fact that the parameters in the analytical function vary with the type and model of the encountered car. Since the type of vehicle encountered is not known a priori, the parameters in the magnetic field function are

unknown. The use of both sonar and magnetic sensors and an adaptive estimator is shown to address this problem. While the sonar sensors do not work at very small inter-vehicle distance and have low refresh rates, their use during a short initial time period leads to a reliable estimator. Extensive experimental results are presented using a laboratory wheeled car door and full scale passenger sedans. The results show that planar position and orientation can be accurately estimated for a range of relative motions at different oblique angles. A video showing a real-time demo of the system is included both in the thesis and supplementary files.

Next, the proposed sensing principle is adopted to develop a sensor system for non-intrusive measurement of piston position inside a cylinder. Piston position measurement is required for many applications in a number of industrial domains. Examples include piston position estimation for engine performance optimization, automatic earth excavation, and seeding depth control for precision farming. By modeling the magnetic field of the piston as a function of its position and using sensors to measure magnetic field intensity, the position of the piston can be estimated. A challenge arises from the fact that the parameters of the model vary from one piston to another piston and it would be cumbersome to calibrate for each piston. This challenge is addressed by utilizing two magnetic field sensors with known longitudinal separation between them. A number of estimation methods are proposed that identify and update magnetic field parameters in real time without requiring any additional reference sensor for calibration. Results of experiments with a free piston engine and a pneumatic actuator are presented showing a maximum absolute error of $0.4$ mm in both applications. A video showing a real-time demo of the system is included both in the thesis and supplementary files.

A serious challenge in the usage of magnetic sensors is the influence of disturbances caused by other ferromagnetic objects brought close to the sensors. External ferromagnetic objects can disturb the sensors signals causing large errors in position estimation. To address this issue, a method based on redundant sensors is developed to

eliminate the influence of external magnetic disturbances. Experimental results demonstrate that sub-millimeter accuracies in position measurement can be obtained with such a system in spite of disturbances from external ferromagnetic objects.

Finally, the proposed sensing principle is adopted to develop a portable roadside sensor system for vehicle counting, classification and speed measurement. The sensor system can be placed next to the road to measure traffic in the adjacent lane. The detection rate accuracy of the system is shown to be 99%. An algorithm based on a magnetic field model is proposed to make the system robust to the errors created by larger vehicles driving in the nonadjacent lane of the road. These false calls cause 8% error if uncorrected. Use of the proposed algorithm reduces this error to only 1%. A speed measurement algorithm is developed that is based on calculation of cross-correlation between longitudinally spaced sensors. Fast computation of cross-correlation is enabled by using frequency domain signal processing techniques. An algorithm to automatically correct for any small misalignment of the sensors is utilized. Using an accurate differential GPS as a reference, it is shown that maximum absolute error of the speed estimates is less than 2.5% over the entire speed range of $5-27\ \mathrm{m/s}$ $(11-60\ \mathrm{mph})$. Vehicle classification is done based on the magnetic length and an estimate of the average vertical magnetic height of the vehicle. Vehicle length is estimated from the product of occupancy and estimated speed. Average vertical magnetic height is estimated by using two magnetic sensors vertically spaced by $0.3\ \mathrm{m}$. Also, it is shown that the sensor system can be used to reliably count the number of right turns at an intersection with an accuracy of 95%. The developed sensor system is compact, portable, wireless and inexpensive. Data is presented from a large number of vehicles on a regular busy urban road in the Twin Cities in Minnesota.

The fundamental contribution of this thesis is the development of a new sensing principle that has a large number of applications in a number of different engineering domains.

# Table of Contents

# List of Tables

# List of Figures

# List of Videos

## Citations of Published Work

Some portions of this thesis have appeared in the following publications:

***Journal Publications:***

1) S. Taghvaeeyan, R. Rajamani, “Use of vehicle magnetic signatures for position estimation,” *Applied Physics Letters*, Vol. 99, no. 13, Article 134101, 2011.
2) S. Taghvaeeyan, R. Rajamani, "The development of vehicle position estimation algorithms based on the use of AMR sensors," *Intelligent Transportation Systems, IEEE Transactions on*, vol.13, no.4, pp.1845-1854, 2012.
3) S. Taghvaeeyan, R. Rajamani, Z. Sun, “Non-intrusive piston position measurement system using magnetic field measurements,” *Sensors Journal, IEEE*, vol.13, no.8, pp. 3106-3114, 2013.
4) S. Taghvaeeyan, R. Rajamani, “Portable roadside sensors for vehicle counting, classification and speed measurement,” *Intelligent Transportation Systems, IEEE Transactions on*, vol.15, no.1, pp. 73-83, 2014.
5) S. Taghvaeeyan, R. Rajamani, “Two-dimensional sensor system for automotive crash prediction,” *Intelligent Transportation Systems, IEEE Transactions on*, vol.15, no.1, pp. 178-190, 2014.
6) S. Taghvaeeyan, R. Rajamani, “Nature-inspired position determination using inherent magnetic fields,” *Technology*, Vol.2, no. 2, 2014.

***Conference Publications:***

1) S. Taghvaeeyan, R. Rajamani, “The development of AMR sensors and vehicle position estimation algorithms for imminent crash detection,” in *Proceedings of the American Control Conference*, 2011.

2) S. Taghvaeeyan, R. Rajamani, “Two-dimensional sensor system for automotive crash prediction,” in *Proceedings of the ASME Dynamic Systems and Control Conference*, 2012.
3) S. Taghvaeeyan, R. Rajamani, “Portable roadside sensors for vehicle counting and speed measurement,” in *Proceedings of Transportation Research Board 92nd Annual Meeting*, 2013.
4) S. Taghvaeeyan, R. Rajamani, Z. Sun, “Novel non-intrusive sensor for piston position measurement,” in *Proceedings of the American Control Conference*, 2013.

***Patent Application:***

S. Taghvaeeyan, R. Rajamani, “Position sensing system,” Provisional application and PCT application filed by the University of Minnesota on March 19th 2013 and March 19th 2014, respectively.

# 1. Introduction

## 1.1. Positioning and Navigation in Nature Using Magnetic Fields

The compass indicates the direction of the Earth's North Pole and has been used as a navigation tool on ships for over 900 years [1]. Only much more recently has it been found that many creatures, such as butterflies, newts, and mole rats, use magnetic fields to migrate over thousands of miles [2-4]. They use much finer navigation information from magnetic fields than merely the orientation of the North Pole.

Earth has a churning molten core that casts a magnetic field on its surface with magnetic intensity that varies with position and orientation. Many animals in nature appear to use regional variations in this magnetic field, such as variations in the magnetic field intensity and variations in the inclination of magnetic field lines, for navigation [5]. For example, loggerhead sea turtles hatch on the eastern coast of Florida and then immediately head to the North Atlantic gyre (a clockwise ocean current that flows clockwise around the Sargasso Sea). These turtles spend 5 to 10 years in the gyre's warm waters before heading back to the Florida coast. Researchers have found that loggerheads can sense both magnetic field intensity and inclination angle [6, 7]. By adjusting magnetic fields around a laboratory tank, they have been able to show that the turtles swam preferentially along their migratory path as the magnetic field around the tank was adjusted with one of three types of magnetic fields found along their migratory path.

Similarly, researchers have shown that lobsters use a magnetic map sense [8] with which they can determine their position relative to a goal and orient themselves towards the goal even after being displaced $12 - 37$ km to unfamiliar locations [9].

It has been shown that homing pigeons can sense strength, direction, and polarity to orient themselves [3, 10, 11]. In fact, solar storms as well as artificially created magnetic field anomalies greatly perturb the location sense of the birds [12, 13]. Besides pigeons, many other animals, such as European robins, songbirds, indigo buntings, spiny oysters, newts, salamanders, fishes, and bats, have been found to use magnetic strength and/or orientation for positioning and navigation [3, 14-19].

The above animals are able to exploit magnetic fields to find their position with respect to the source of the magnetic field because they contain magnetic "sensors" in their bodies. Researchers have identified an area of the mammalian brain that processes magnetic field information [20]. Pigeons and songbirds have been discovered to possess multiple magnetic sensors as well [21, 22].

In conclusion, it is evident that many creatures take advantage of the "inherent" magnetic field of the Earth for positioning and navigation by using their magnetic "sensors". This thesis seeks to apply similar techniques so as to develop methods for position estimation of individual ferromagnetic objects found all around us in everyday life by exploiting their inherent magnetic fields using magnetic sensors and estimation algorithms.

## 1.2. A New Sensing Principle for Position Estimation of Ferromagnetic Objects

The compass has long been used by humans to find their orientation with respect to the Earth's North Pole. It is used as an aid for heading determination in today's

navigation systems [23]. Hall-effect and eddy current sensors are used in the modern industrial world for distance measurement and utilize either permanent magnets or electromagnets for their operation [24, 25]. They are only able to measure position at very small distances (typically less than 1 cm) between the magnet and the sensor. In order to measure position at larger distances, several magnets have to be embedded into the moving object [26, 27].

Previously, the inherent magnetic fields of ferromagnetic objects have been exploited only for binary sensing (detection) of objects. For example, magnetic sensors embedded in highway lanes have been used to detect passing cars and to count the number of cars that travel over a sensor [28, 29]. Likewise, such sensors have also been used to detect the presence of a parked car in a parking spot [30, 31]. Both of these applications only detect the presence of a vehicle and do not measure the distance to the vehicle from the sensor. Recently, methods have also been proposed to extract location information from the inherent magnetic field of a building or the Earth for indoor or outdoor navigation [32-36]. However, these proposed methods rely on survey magnetic maps. Therefore, other types of positioning sensors have to be used in advance in order to create such survey maps of a desired area.

The position estimation principle described in this thesis differs fundamentally from the aforementioned approaches; it exploits the inherent magnetic fields of ferromagnetic objects for accurate position estimation without requiring the use of any electromagnets or permanent magnets. Neither line of sight nor close proximity between sensor and object are required. Also, using magnetic field models and adaptive estimation methods, there would be no need for pre-calibrated magnetic maps or lookup tables.

Objects with ferromagnetic parts, such as cars, pistons, and spool valves, have inherent magnetic fields which vary as a function of position around the object. Figure 1-1 shows magnetic field around a sphere magnetized in a uniform magnetic field.

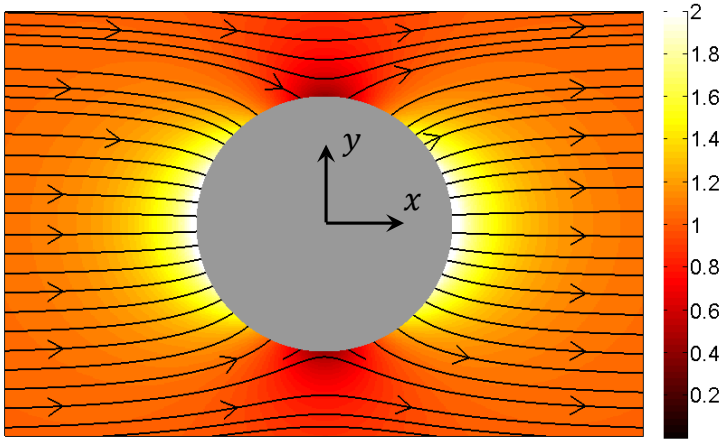


Figure 1-1. Magnetic field around a ferromagnetic sphere magnetized in a uniform magnetic field.

The spatial variation of an object's magnetic field is specific to its shape and can be mathematically modeled as a function of position around the object and the object's specific geometric and magnetic parameters. If the parameters in the model are known, position can be estimated by measuring magnetic field. However, the model parameters vary from one object to another even if the objects have the same shape and size, but a different level of magnetization. Furthermore, the functions relating magnetic field $B$ of an object to its position $x$ are generally nonlinear of the forms of $B \sim 1/x$, $1/x^2$, or $1/x^3$. These nonlinear relations add another level of complexity in the development of position estimation sensors based on the proposed sensing principle. Nevertheless, it is shown in this thesis that using (a) a mathematical model of the magnetic field, (b) measurements of magnetic field at a few discrete locations with inexpensive magnetic sensors, and (c) adaptive estimation techniques, the position of a ferromagnetic object can be accurately estimated.

In Chapter 2, the proposed sensing principle is applied to the problem of imminent automotive crash detection. A vehicle is made of many metallic parts (for example, chassis, engine, and body) which have a residual magnetic field and/or get magnetized in

the Earth's magnetic field. These magnetic fields create a net magnetic field for the whole vehicle which can be analytically modeled as a function of vehicle-specific parameters and position around the vehicle. Therefore, the proposed sensing principle can be applied to estimate a vehicle's position, velocity, and orientation relative to another vehicle so as to predict and classify an imminent unavoidable crash. When it is predicted that a crash is unavoidable, the crash information such as impact location, impact angle, and severity of the crash, can be highly effective in mitigating the effect of the crash on the occupants by using active safety systems.

Another major benefit of the proposed position estimation principle is that since no permanent magnets or electromagnets are used, no installation is required inside the object whose position needs to be measured. For example, the position of a piston inside an engine cylinder can be measured from outside the cylinder without requiring any installation inside the cylinder, as discussed later in Chapter 3. Therefore, being non-contact and non-intrusive, the developed sensor has an advantage over position sensors that require contact such as the linear variable differential transformer (LVDT) and the potentiometer. This advantage is significant when the environment around the object whose position needs to be measured is harsh like the hot environment in an engine cylinder or the environment inside a hydraulic cylinder operating by high-pressure fluid.

The sensing principle proposed in this thesis and the methods developed for adaptive parameter estimation can be used in a variety of applications where the position of or distance to a ferromagnetic object is required to be continuously measured. On the other hand, even with the binary detection applications, some of the performance metrics can be improved if magnetic field models are used. As an example, consider the case where magnetic sensors are used to count the vehicles passing in a lane. A common source of error in this case is false calls due to larger vehicles passing in the other lanes. In Chapter 4, a portable sensor system is developed which can be placed on the side of the

road to measure traffic flow in the adjacent lane. It is shown that using magnetic field models, the error due to false calls can be reduced from 8% to only 1%.

Finally, it is worth mentioning that if the object of interest lacks an inherent magnetic field, a magnet can be attached to it and exactly the same developed methods be applied by modeling the magnetic field of the attached magnet. An example of this case is presented in Chapter 3 where the position of a piston lacking inherent magnetic field is measured by attaching a small magnet to the head of the piston.

## 1.3. Magnetic Materials

In this section, we briefly introduce different types of materials based on their magnetic behavior. This brief introduction can help to understand what types of objects might have inherent magnetic field and what types of objects might lack it. Materials can be classified into five categories according to their magnetic behavior: diamagnetic, paramagnetic, antiferromagnetic, ferrimagnetic and ferromagnetic [37]. While all of these materials get magnetized by an external magnetic field, the magnetization is far more considerable for ferromagnetic (like Fe) and ferrimagnetic materials. These two types of materials have the same behavior at room temperature. They can be distinguished from one another by magnetic measurements only if the measurements are made over a range of temperatures.

The amount of magnetization depends on magnetic susceptibility $\chi$ of the material - the higher the magnetic susceptibility, the higher the amount of magnetization. The magnetic behavior of different materials can be characterized based on their corresponding values of $\chi$:

1. Empty space; $\chi = 0$, since there is no matter to magnetize.
2. Diamagnetic; $\chi$ is small and negative.

3. Para- and antiferromagnetic; $\chi$ is small and positive.
4. Ferro- and ferrimagnetic; $\chi$ is larger and positive.

Table 1-1 shows typical values of magnetic susceptibility of some common materials [38-40]. Note that the susceptibility of ferromagnetic materials is several orders of magnitude larger than the susceptibility of diamagnetic and paramagnetic materials.

Table 1-1. Magnetic susceptibility of some common materials.

| Material | Type | $\chi$ | Material | Type | $\chi$ |
|---|---|---|---|---|---|
| Bismuth | Dia | $-1.6 \times 10^{-4}$ | Aluminum | Para | $2.1 \times 10^{-5}$ |
| Gold | Dia | $-3.4 \times 10^{-5}$ | Platinum | Para | $7.8 \times 10^{-5}$ |
| Silver | Dia | $-2.4 \times 10^{-5}$ | Stainless Steel (Type 303) | Para | $2 \times 10^{-2}$ |
| Copper | Dia | $-9.7 \times 10^{-6}$ | Iron (99Fe) | Ferro | $6 \times 10^{3}$ |
| Water | Dia | $-9.0 \times 10^{-6}$ | Iron (99.9Fe) | Ferro | $3.5 \times 10^{5}$ |
| Oxygen | Para | $1.9 \times 10^{-6}$ | Mild Steel | Ferro | $1.1 \times 10^{3}$ |
| Sodium | Para | $8.5 \times 10^{-6}$ | Silicon-iron (96Fe-4Si) | Ferro | $7 \times 10^{3}$ |

Considering Figure 1-1, the magnetic field at an arbitrary point $A = (x_A, y_A)$ on the $XY$ plane outside the sphere placed in a uniform magnetic field $B = B_0\hat{x}$ has the following form [41]:

$$\begin{cases} B_x(x_A, y_A) = B_0\big(1 + \alpha f_x(x_A, y_A, R)\big) \\ B_y(x_A, y_A) = B_0\left(\alpha f_y(x_A, y_A, R)\right) \end{cases} \quad \text{for } (x_A + y_A)^2 \geq R^2, \tag{1-1}$$

where $f_x$ and $f_y$ are functions of position and radius of the sphere $R$, and $\alpha = \frac{\chi}{\chi + 3}$. For materials with small values of $\chi$ we have:

$$\chi \cong 0 \quad \Longrightarrow \quad \alpha \cong 0 \quad \Longrightarrow \quad \begin{cases} B_x(x_A, y_A) \cong B_0 \\ B_y(x_A, y_A) \cong 0 \end{cases} \qquad \text{for } (x_A + y_A)^2 \geq R^2. \tag{1-2}$$

Therefore, the magnetic field around the sphere remains uniform. However, for materials that have large values of $\chi$ ($\alpha \cong 1$), the magnetic field at an arbitrary point $A = (x_A, y_A)$ would be a function of position around the sphere and the parameters $R$, $\alpha$, and $B_0$. Thus, if the magnetic field is measured using magnetic sensors and the parameters are known, one can find the position of point $A = (x_A, y_A)$ from the magnetic field model described by (1-1).

It can be noticed from this example that the magnetic field around the sphere is a function of its size, level of magnetization, and position around it. The same observation is true for other ferromagnetic objects. As a part of this research work, simple models of magnetic fields of different objects as a function of position around them are derived. It is shown that by measuring the magnetic field with sensors, using a magnetic field model of the object, and adaptive estimation techniques, the position of the object can be accurately estimated.

## 1.4. Thesis Contributions and Outline

This thesis proposes a new fundamental sensing principle for detection, identification, and position estimation of ferromagnetic objects based on exploiting the inherent magnetic signature of these objects. It is shown that for an individual ferromagnetic object, using (a) a mathematical model of the magnetic field around the object, (b) measurements of magnetic field at a few discrete locations around the object with inexpensive magnetic sensors, and (c) adaptive estimation techniques, the position of the ferromagnetic object can be accurately estimated.

In Chapter 2, the proposed sensing principle is adopted to develop an inexpensive sensor system for a vehicle that can predict an imminent collision with another vehicle just before the collision occurs. A vehicle is made of many metallic parts (for example, chassis, engine, and body) which have a residual magnetic field and/or get magnetized in the Earth's magnetic field. These magnetic fields create a net magnetic field for the whole vehicle which can be analytically modeled as a function of vehicle-specific parameters and position around the vehicle. In order to verify this hypothesis, the problem of 1-D vehicle position estimation is first considered (Section 2.2). The following steps are taken:

- Modeling a vehicle as a rectangular block of magnets, a function is analytically derived which models the magnetic field along the longitudinal axis of the vehicle as a function of distance from the vehicle and specific vehicle parameters (Section 2.2.1).
- The developed model is verified through experiments with several vehicles. It is shown that the developed model accurately fits the experimental data (Section 2.2.2).

The magnetic field model relates the magnetic field of the vehicle to distance from the vehicle and includes vehicle-specific parameters. If the parameters are known, distance to the vehicle can be estimated from magnetic field measurements. However, the specific-vehicle parameters vary from one vehicle to another vehicle and are unknown a priori. Therefore, the following approach is taken:

- Using an additional redundant magnetic sensor, an adaptive estimator is developed that can estimate both model parameters as well as vehicle distance as a vehicle approaches the sensors (Section 2.2.3).
- In the next step, to speed up the parameter convergence of the developed estimator, sensor fusion with a sonar sensor is used (Section 2.2.4).

- Several experiments with vehicles and laboratory test rigs are performed to verify the performance of the estimator (Section 2.2.5). It is shown that the position estimation accuracy is 1.3 cm.

In general, a crash can occur anywhere around the 2-D plane of a vehicle. Thus, after proof of concept by the developed 1-D position estimation system, the problem of 2-D position estimation is considered next (Section 2.3). The following steps are followed in order to develop such a 2-D system:

- The magnetic field model developed earlier is expanded to model the field over the 2-D plane of a vehicle (Section 2.3.1).
- A sonar system is developed that can measure both the distance to a vehicle as well is its orientation (Section 2.3.2).
- A sensor configuration is proposed for the estimation of 2-D position and orientation based on magnetic sensors and the developed sonar system (Section 2.3.3).
- An estimator is developed that adopts both magnetic sensors and the sonar system measurements to estimate relative 2-D position and orientation of an approaching vehicle in real time.
- The estimator is implemented using a PC and embedded microcontrollers for real-time 2-D position estimation and achieves a refresh rate of 500 Hz.
- The developed sensor system is verified through experiments with both a real vehicle and laboratory test rigs (Section 2.3.4).

In Chapter 3, the proposed new sensing principle is applied for non-intrusive estimation of piston position inside a cylinder. As a first case study, a sensor system is developed to measure outer piston position in a free piston engine (FPE, Section 3.2). First, the following step is taken:

- The magnetic field of the piston is modeled as a function of distance along the axis of the motion of the piston (Section 3.2.1).

The model includes unknown piston-specific parameters. In order to estimate piston position from magnetic sensors measurements using the developed model, the unknown parameters should be identified. When model parameters are identified, piston position can be continuously estimated from the magnetic sensors measurements. Five different methods are proposed for identification of the model parameters. The first two methods take advantage from the LVDT already installed in the FPE. They use measurements from the LVDT and one magnetic sensor:

- Method 1 is developed based on the least squares method to identify the model parameters (Section 3.2.2.1).
- Method 2 is developed based on minimizing the maximum error to identify the model parameters (Section 3.2.2.2).

The other three methods are based on using only the measurements from two longitudinally spaced magnetic sensors. Therefore, no other reference sensor is required for identification and calibration of the parameters:

- Method 3 is based on a one-time full-stroke motion of the piston and identifying the model parameters from the measurements by applying the iterated nonlinear least squares method (Section 3.2.3).
- Method 4 is based on the extended Kalman filter. The model parameters as well as piston position are adaptively estimated in real time during the regular motion of the piston (Section 3.2.4.1).
- Method 5 is similar to the fourth method, with the difference that the information about the stroke length of the piston is included in the measurements to improve convergence speed of the estimator (Section 3.2.4.2).

- It is shown through experiments that the maximum absolute error of the position estimation system is 0.4 mm.

Next, the problem of piston position estimation in a pneumatic actuator is considered (Section 3.3). The specific pneumatic actuator considered in this thesis is made of paramagnetic materials (e.g. the piston and the piston rod are made of aluminum and type 303 stainless steel, respectively) and lacks an inherent magnetic field. Therefore, a small magnet is attached to the piston head so as to create a change in magnetic field with the motion of the piston. The following steps are taken in order to develop a sensor system for piston position estimation:

- An experimental setup is developed which includes the pneumatic actuator, an LVDT used as a reference sensor, magnetic sensors, and required electronics for capturing sensors measurements (Section 3.3.1).
- The magnetic field due to the attached magnet is modeled as a function of distance along the axis of motion of the piston (Section 3.3.2).
- The derived model includes model parameters that are identified using estimation Method 3 developed earlier (Section 3.3.3).
- The sensor system is implemented using a PC and an embedded microcontroller. The magnetic sensors measurements are sent to a PC and the piston position is estimated and displayed in real time. The position estimation accuracy is shown to be 0.4 mm.

A challenge in the use of magnetic sensors for position estimation is the effect of external disturbances on the magnetic sensors due to unexpected presence of other ferromagnetic objects. The external disturbances may cause inaccuracies in piston position estimation. This problem is considered in Section 3.5 and a method is proposed to estimate the disturbance on the sensors to be subtracted from sensor readings. To show the validity of the proposed method, two different sensor configurations are implemented and their performance is evaluated:

- A sensor system consisting of four magnetic sensors placed as in the corners of a square (Sections 3.5.1-3.5.3).
- A sensor system consisted of three longitudinally spaced magnetic sensors (Section 3.5.5).
- Using an electromagnet to create a step disturbance on the sensors, it is shown that the developed method can reduce the error due to the disturbance to less than $1$ mm in $45$ ms.

In Chapter 4, a portable magnetic sensor system is developed that can be placed adjacent to a road for vehicle counting, speed measurements, and classification by analyzing the magnetic signatures of passing vehicles. Existing measurement systems based on magnetic sensors require the sensors to be embedded into the pavement. The sensor system developed here, on the other hand, is portable and can be placed on the sidewalk next to the road. The developed system consists of four magnetic sensors arranged in a specific configuration described in Section 4.2 and has the following key features:

- The accuracy achieved in detection rate is $99\%$ (Section 4.3).
- The error due to false calls caused by larger vehicles passing in the nonadjacent lane is only $1\%$ compared with $8\% - 15\%$ error in existing systems (Section 4.4).
- The maximum absolute speed estimation error is $2.5\%$ over the speed range of $5 - 27$ m/s or $11 - 60$ mph (Section 4.5).
- Vehicles are classified into 4 classes; Class I: sedans, Class II: SUVs, pickups and vans, Class III: Buses and 2-3 axle trucks, and Class IV: articulated buses and 4-6 axle trucks (Section 4.6).
- Vehicles in Classes III and IV are accurately classified due to their distinct magnetic length which is estimated by the sensor system.

- Vehicles in Classes I and II are classified separately based on an estimate of their magnetic height in addition to their magnetic length. The classification accuracy achieved is 83% compared with existing systems with classification accuracy of 63%.

Later in Chapter 4 and in Section 4.7, the magnetic sensors are used in a different configuration to develop a new sensor system which can be placed at the corner of an intersection to count the number of right turns in the adjacent lanes. The number of vehicles making right turns is used to adjust the traffic signals and this counting is currently performed manually. The developed sensor system has the following features:

- The right turn detection rate is 95%.
- The challenge in counting the number of right turns is the false calls created by larger straight-driving vehicles which, if uncorrected, cause 31% overdetection. Two methods are developed which eliminated this error completely.

Concluding comments to this thesis are summarized in Chapter 5.

# 2. Imminent Automotive Crash Detection

## 2.1. Introduction

The work presented in this chapter is motivated by the need to develop an inexpensive sensor system for an automobile that can predict an imminent collision with another vehicle just before the collision occurs. The prediction needs to occur at least 100 ms before the collision so that there is adequate time to initiate active occupant protection measures during the crash. Examples of simple occupant protection measures that can be initiated based on the prediction include pre-tightening of seat belts and gentler inflation of air bags. In addition, active crush space enhancement systems such as active bumpers [42, 43] and rapid active seat back control [44] can be utilized.

Active occupant protection measures involve considerable cost, discomfort and even a small risk to the occupants. For example, deployment of air bag is an expensive action resulting in considerable cost. Likewise, rapid seatback motion control during driving can be a significant annoyance and a danger to the driver if triggered unnecessarily. Therefore, these measures can be initiated only if the collision prediction system is highly reliable. A false prediction of collision has highly unacceptable costs.

Traditionally, radar and laser systems have been used on cars for adaptive cruise control and collision avoidance [45-50]. These sensors typically work at inter-vehicle spacing greater than 1 m. They do not work at very small inter-vehicle spacing and

further have a very narrow field of view at small distances [47]. Collision prediction based on sensing at large distances is unreliable. For example, even if the relative longitudinal velocity between two vehicles in the same lane is very high, one of the two vehicles could make a lane change resulting in no collision. An imminent collision can be predicted reliably enough to inflate air bags only when the distance between vehicles is very small and when it is clear that the collision cannot be avoided under any circumstances. Radar and laser sensors are not useful for such small distance measurements. Moreover, radar or laser sensors can cost well over $1000. Thus, it is inconceivable that a number of radar and laser sensors be distributed all around the car in order to predict all the possible types of collisions that can occur. It should be noted that camera based image processing systems suffer from some of the same narrow field of view problems for small distances between vehicles. Finally, another limitation in usage of the aforementioned type of sensors is the high refresh rate necessary for predicting a crash at least 100 ms before the collision. Therefore, we focus on development of a sensor system that can measure relative vehicle position, velocity and orientation at very small inter-vehicle distances with a high refresh rate.

The main idea of the new proposed sensing system is to use the inherent magnetic field of a vehicle for position estimation. A vehicle is made of many metallic parts (such as chassis, engine, and body) which have a residual magnetic field and/or get magnetized in the Earth's magnetic field. These magnetic fields create a net magnetic field for the whole vehicle which can be analytically modeled as a function of vehicle-specific parameters and position around the vehicle. By measuring the magnetic field using magnetic sensors such as anisotropic magnetoresistive (AMR) sensors, the position of the vehicle can be estimated if the vehicle-specific parameters are known. However, the specific parameters vary from one type of vehicle to another type of vehicle, both due to varying amounts of ferromagnetic material and varying levels of magnetization. Therefore, these parameters need to be estimated along with the position for every encountered vehicle. This challenge is addressed by the use of both sonar and magnetic

sensors and an adaptive estimator. While the sonar sensors do not work at very small inter-vehicle distance and have low refresh rates, their use during a short initial period of time leads to a reliable estimator. Use of magnetic sensors enables the sensing system to be able to work at very small distance down to zero, have a very high refresh rate, and be inexpensive and compact.

This chapter is organized as follows: In Section 2.2, we present a sensing system developed for 1-D vehicle position estimation based on the proposed method. While the developed system can be used for real-time estimation of position just prior to a frontal or rear-end collision, an impact due to collision can occur at any location around the car body. Thus, a new sensing system has been developed based on the work presented in Section 2.2 to estimate not only the relative position, but also the orientation of the colliding vehicle anywhere in the 2-D plane. This new system is described in Section 2.3. Technical challenges in implementation of the developed system and potential future work are discussed in Section 2.4. Finally, this chapter is concluded in Section 2.5.

## 2.2. One-dimensional Position Estimation

In order to check the feasibility of the proposed concept for crash detection, we first focus on the problem of 1-D position estimation. In general, a crash can occur anywhere around a vehicle with different angles and thus, 2-D position estimation is needed to predict a crash correctly. However, considering the simplified problem of 1-D position estimation helps gaining insight for the more complex problem of 2-D position estimation discussed later in Section 2.3.

This section is organized as follows: In Section 2.2.1 we derive an analytical relation which models the magnetic field generated by a vehicle as a function of its position. Several tests were performed to verify this model and the results are presented in Section 2.2.2. Since the model includes parameters that vary from one vehicle to another

vehicle and thus unknown a priori, we develop an estimator to estimate both model parameters and the position in real time. The developed estimator is described in Section 2.2.3. In order to improve the convergence of the estimator, a sonar sensor is used and its measurements are fused with the magnetic sensors measurements resulting in a new estimator described in Section 2.2.4. Experimental results are presented in Section 2.2.5.

### 2.2.1. Analysis of Vehicle Magnetic Signature

The first step in order to check if magnetic sensors can be used for position measurements is to see if there exists a reliable relation between magnetic field and position around vehicle. Consider the scenario shown in Figure 2-1 where the vehicle moves toward the magnetic sensors in a 1-D motion. We want to find an analytical relation between the measured magnetic field along the $X$-axis of the sensor and the distance of the car to the sensor.

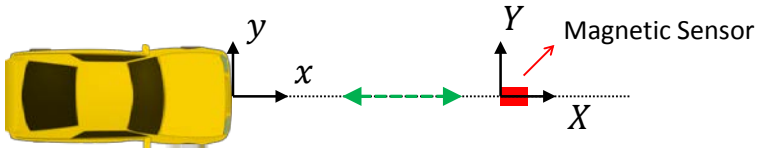


Figure 2-1. General scenario of 1-D position estimation problem.

To derive the desired relation, we model the vehicle as a rectangular block of magnetic material as shown in Figure 2-2.

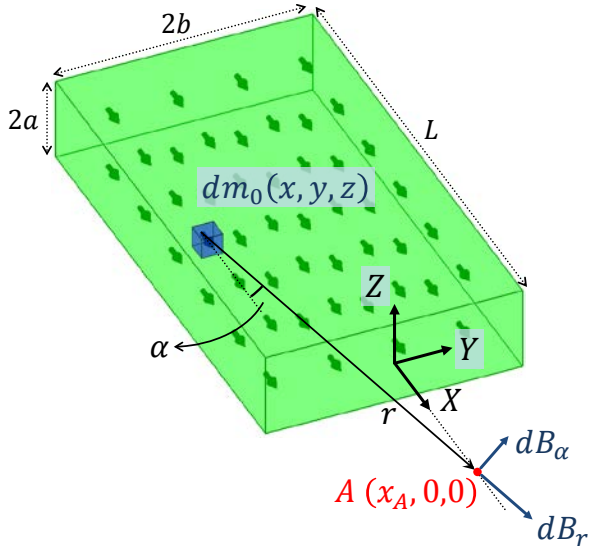


Figure 2-2. Analysis of magnetic field around a rectangular block.

According to [41], the planar components of the magnetic field generated by the element $dm_0$ at the point $A$ are given by:

$$dB_r = \frac{\mu_0 dm_0}{2\pi r^3}\cos\alpha, \tag{2-1}$$

$$dB_\alpha = \frac{\mu_0 dm_0}{4\pi r^3}\sin\alpha. \tag{2-2}$$

Assuming that point $A$ is at distance $x_A$ from the surface of the cube, we can express $r$ and $\alpha$ in terms of $x_A$, $y$, and $z$:

$$r^2 = y^2 + z^2 + (x_A - x)^2, \tag{2-3}$$

$$|\alpha| = \operatorname{atan}\left(\frac{\sqrt{y^2+z^2}}{x_A - x}\right), \tag{2-4}$$

$$\sin^2\alpha = \frac{y^2+z^2}{y^2+z^2+(x_A-x)^2}, \tag{2-5}$$

$$\cos^2\alpha = \frac{(x_A - x)^2}{y^2 + z^2 + (x_A - x)^2}. \tag{2-6}$$

Therefore, the magnetic field generated by $dm_0$ along $X$-axis can be written as

$$dB_x = dB_r \cos\alpha - dB_\alpha \sin\alpha = \frac{\mu_0 dm_0}{4\pi}\left(\frac{2(x_A - x)^2 - (y^2 + z^2)}{((x_A - x)^2 + y^2 + z^2)^{\frac{5}{2}}}\right). \tag{2-7}$$

As a result, the magnetic field generated by the front surface of the block can be obtained from the following integral:

$$B_x = \frac{\mu_0 m_0}{4\pi}\int_{-L}^{0}\int_{-b}^{b}\int_{-a}^{a}\frac{2(x_A - x)^2 - (y^2 + z^2)}{((x_A - x)^2 + y^2 + z^2)^{5/2}}\,dzdydx. \tag{2-8}$$

Assuming that $b \gg a$ (which is acceptable looking at a sedan from the front), the solution to the integral of (2-8) would be:

$$B_x = \frac{\mu_0 m_0 ab}{\pi}\left(\frac{1}{x_A(b^2 + x_A^2)^{\frac{1}{2}}} - \frac{1}{(x_A + L)(b^2 + (x_A + L)^2)^{\frac{1}{2}}}\right). \tag{2-9}$$

Considering the size of a sedan, it is reasonable to ignore the second term ($x_A + L \gg x_A$) for measurements close to the car. Also, for small values of $x_A$, we can use the following approximation:

$$B_x \cong \frac{\mu_0 m_0 ab}{\pi}\frac{1}{x_A(b^2 + x_A^2)^{\frac{1}{2}}} = \frac{\mu_0 m_0 a}{\pi}\frac{1}{x_A\left(1 + \left(\frac{x_A}{b}\right)^2\right)^{\frac{1}{2}}} \cong \frac{\mu_0 m_0 a}{\pi x_A} = \frac{p}{x_A}. \tag{2-10}$$

where the definition of $p$ is apparent. If there is any existing magnetic field at point $A$, like the Earth's magnetic field, a constant needs to be added to (2-10) to obtain the total magnetic field, resulting in:

$$B_x \cong \frac{p}{x_A} + q. \tag{2-11}$$

In the next section, we verify the model expressed by (2-11) through experimental data.

### 2.2.2. Verification of the Analytical Model

A number of tests with different vehicles were performed in order to experimentally verify the derived analytical model of magnetic field vs. vehicle distance. Figure 2-3 shows a general schematic of the tests.

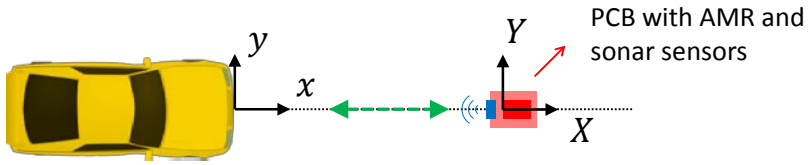


Figure 2-3. General scenario of 1-D position estimation experiments.

An anisotropic magnetoresistive (AMR) sensor and a sonar sensor (working at ultrasonic frequency of 40 KHz) are packaged on a printed circuit board (PCB) together with a microprocessor that reads the sensor signals and transmits their values to a computer. Figure 2-4 shows the developed PCB.

| |
|---|
| 1: Magnetic sensor |
| 2: Sonar sensor |
| 3: Microcontroller |
| 4: USB/Serial converter (for wired communication) |
| 5: Wireless transmitter |

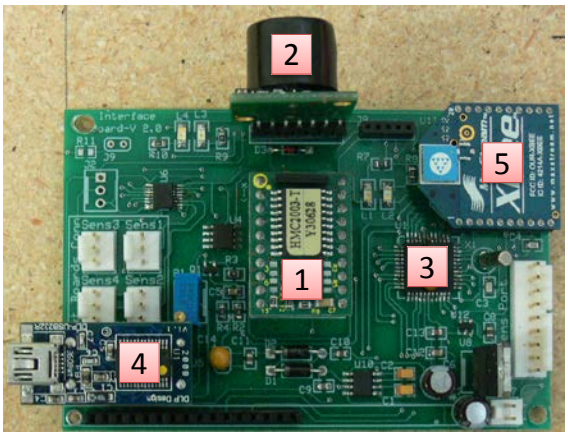


Figure 2-4. The developed PCB for experiments.

An AMR sensor has a silicon chip with a thick coating of piezoresistive nickel-iron. The presence of a magnetic object (in this case, a vehicle) in close range to an AMR sensor causes a change in magnetic field that changes the resistance of the nickel-iron layer. Measuring the resistance, the magnetic field caused by the object can be measured. The HMC2003 three-axis magnetic sensor boards from Honeywell are utilized for the system developed in this chapter. Each sensor board contains core HMC100x AMR sensing chips which cost about $10. Application note AN218 from Honeywell describes the use of the AMR chips for vehicle detection and traffic counting applications (neither of which involves vehicle position estimation) [51].

The outputs of the AMR and sonar sensors are sampled at the rate of 2 KHz using a dsPIC microcontroller from Microchip with 12-bit analogue-to-digital converter (ADC) and transferred to PC in real time through serial port. Wireless communication is also possible at a lower sampling rate.

Figure 2-5 shows the relationship between the magnetic field measured by the AMR sensor (along the $X$-axis) and actual distance measured by the sonar sensor in a test using a Chevrolet Impala vehicle. Magnetic field is plotted in arbitrary voltage units, the same as what was read from the ADC of the microcontroller. It can be seen that there is obviously a nonlinear relation between the measured magnetic field and distance.

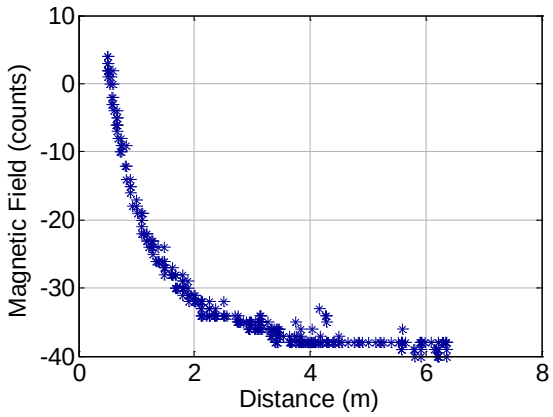


Figure 2-5. Result of the experiments with Chevrolet Impala showing magnetic field in $X$-axis versus distance obtained from sonar sensor.

Based on the model derived in Section 2.2.1 and the experimental data, it is observed that below a threshold distance $x_{th}$, the following relation holds between magnetic field and distance:

$$B_x \cong \frac{p}{x_A} + q \qquad\qquad x \leq x_{th}. \tag{2-12}$$

This equation was fit to experimental data from various vehicles. Figures 4 and 5 show the fitting results from two experiments with a Chevrolet Impala and a Volkswagen Passat. In both of the experiments, the vehicle was moved from an initial distance toward the sensors. In these figures, data set 1 is the set of data points obtained after a certain time that the vehicle gets closer than $x_{th}$ to the sensors. This data set was used for curve fitting. Data set 2 is the set of data points from the same experiment where the vehicle was further than $x_{th}$ from the sensors and is plotted for comparison.

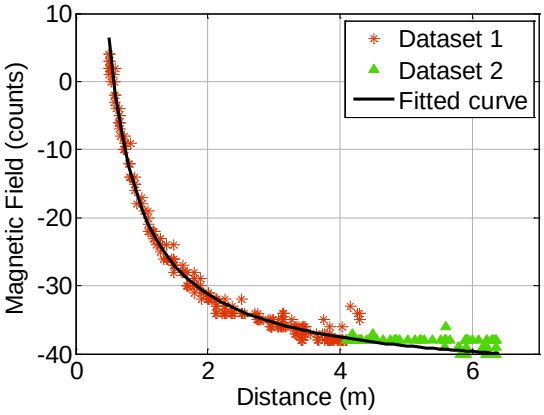


Figure 2-6. Results of the experiment with Chevrolet Impala and fitted curve.

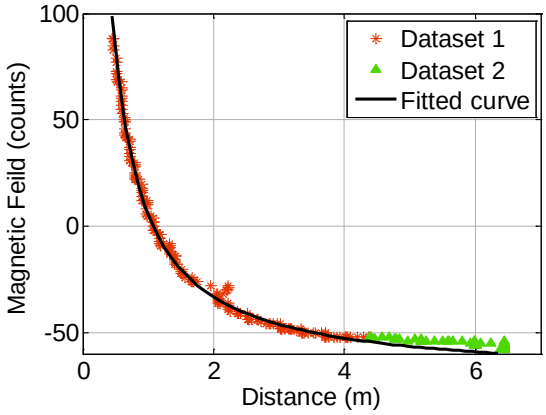


Figure 2-7. Results of the experiment with Volkswagen Passat and fitted curve.

An estimate of $x_{th}$ can be obtained either by visually inspecting the graphs or from the fact that:

$$\begin{cases} B_x = B_{stat} & x \geq x_{th}\,, \\ B_x \cong \dfrac{p}{x_A} + q & x \leq x_{th}\,, \end{cases} \tag{2-13}$$

where $B_{stat}$ is the static magnetic field measured by the magnetic sensor when there is no vehicle close to it. Therefore, at $x = x_{th}$, we have:

$$B_{stat} = \frac{p}{x_{th}} + q. \tag{2-14}$$

One can obtain an estimate of $x_{th}$ by the following equation:

$$x_{th} = \frac{p}{B_{stat} - q + \epsilon} + q. \tag{2-15}$$

where $\epsilon$ is a positive constant used to assure that the change in magnetic field is caused by the vehicle and not quantization error and noise. Table 2-1 summarizes the results of the experiments where (2-12) was applied to the magnetic field around various vehicles.

The table shows the coefficient of determination ($R^2$) of the fitted curves and estimated $x_{th}$ for various vehicles.

Table 2-1. Results from applying the model expressed by (2-12) to experimental data

| Vehicle | $\lvert p \rvert$ | $B_{stat} - q$ | $R^2$ | $x_{th}$ |
|---|---|---|---|---|
| Chevrolet Impala | 25.23 | 3.23 | 0.997 | ~4.8 |
| Honda Accord | 28.42 | −6.79 | 0.999 | ~3.2 |
| Volkswagen Passat | 74.38 | 14.38 | 0.997 | ~4.5 |
| Hyundai Elantra | 10.2 | −3.21 | 0.999 | ~3 |

The next step would be to use the proposed model in (2-12) for relative position measurement. We can solve (2-12) for $x_A$ and if the model parameters $p$ and $q$ are known, get an estimate of $x_A$ by measuring magnetic field. However, as can be seen from Table 2-1, the values of $p$ and $q$ vary with the vehicle, being constant for a specific vehicle but changing from one vehicle to another. Since the type of vehicle encountered is not known a priori, these parameters have to be adaptively updated in real time.

Furthermore, from different experiments, it was observed that the speed of the approaching vehicle has a slight but noticeable effect on measured magnetic field. This is shown in Figure 2-8. The offsets in the magnetic fields, $B_{stat}$, has been subtracted from the measured data so that the difference can be illustrated better. The same trend was also seen in experiments with the Chevrolet Impala and the Hyundai Elantra vehicles. In these experiments, the speed could not be accurately controlled and was measured from the sonar sensor.

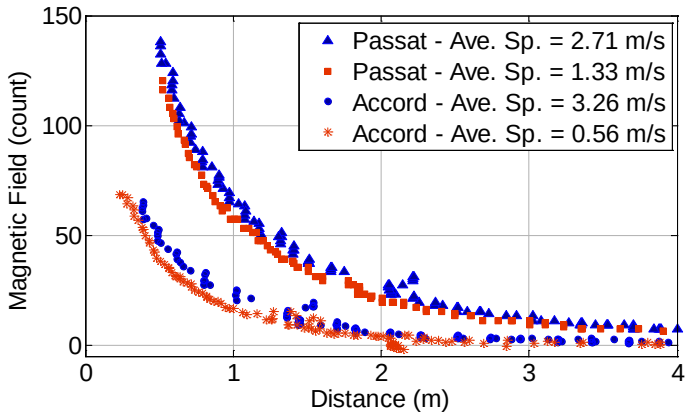


Figure 2-8. Effect of vehicle speed on measured magnetic field.

Finally, the magnetic field generated by the vehicle also changes with changing the global position and orientation of the experiment. One possible explanation is that some of the metal in the vehicle body is magnetized by the Earth's magnetic field and affects the total magnetic field seen by the sensors.

As a result of the aforementioned challenges, we develop an estimator to estimate both model parameters and relative position in real time as a new vehicle approaches the sensors. The estimator is described in the following section.

### 2.2.3. Iterated Extended Kalman Filter (IEKF) for Adaptive Position Estimation

In Sections 2.2.1 and 2.2.2, we derived an analytical relation between distance and magnetic field expressed by (2-12) and we verified it through multiple experiments with vehicles. If the parameters $p$ and $q$ are known, one would be able to estimate the distance by using only one magnetic sensor:

$$B_x = \frac{p}{x_A} + q \qquad x \le x_{th}$$
$$\Rightarrow\ x_A = \frac{p}{B_x - q} \qquad x \le x_{th}. \tag{2-16}$$

However, the parameters $p$ and $q$ change from one vehicle to another vehicle and from one location to another location. Therefore, in order to estimate the distance to an approaching vehicle using magnetic sensor measurements, these parameters should be estimated accurately and quickly in real time, and then be used to estimate the distance to the approaching vehicle.

To address this challenge, we use two magnetic sensors located apart from each other by a distance $d$ as shown in Figure 2-9. Based on the distance $d$, the two magnetic sensors can be either on one PCB or two separate PCBs. The approaching vehicle is assumed to be close enough to affect both magnetic sensors. The use of two sensors enables the estimation of both of the parameters $p$ and $q$. The vehicle position can be subsequently obtained from (2-16).

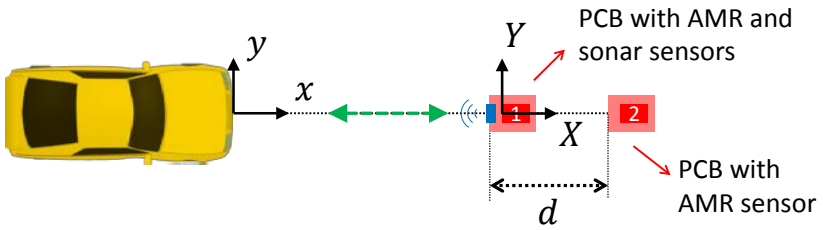


Figure 2-9. Use of two magnetic sensors to estimate both model parameters as well as position.

Based on the model expressed by (2-12), we have the following equations for the two magnetic sensors measurement:

$$\begin{cases} B_1(t_k) = \dfrac{p}{x(t_k)} + q_1 + n_1, \\ B_2(t_k) = \dfrac{p}{x(t_k) + d} + q_2 + n_2. \end{cases} \tag{2-17}$$

where $B_1$ and $B_2$ are the measured magnetic fields along the $X$-axis of the sensors, and $n_1$ and $n_2$ are the noise on each sensor. It should be noted that $q_1$ and $q_2$ are not necessarily equal since $B1_{stat}$ and $B2_{stat}$ can be quite different. However considering the fact that $x_{th}$ is the same for both of the equations, we have:

$$\begin{cases} B1_{stat} = \dfrac{p}{x_{th}} + q_1 \\ B2_{stat} = \dfrac{p}{x_{th}} + q_2 \end{cases} \Longrightarrow q_2 = q_1 + \Delta B_{stat}, \tag{2-18}$$

where $\Delta B_{stat} = B2_{stat} - B1_{stat}$. Eliminate $x$ from equations (2-17) and dropping the time index, we have:

$$\begin{aligned} dB_1(B_2 - \Delta B_{stat}) = \big(B_1 - (B_2 - \Delta B_{stat})\big)p + d\big(B_1 + (B_2 - \Delta B_{stat})\big)q_1 \\ -dq_1^2 + \big(-p - dq_1 + d(B_2 - \Delta B_{stat})\big)n_1 \\ +(p + dB_1 - dq_1)n_2 - dn_1 n_2 \,. \end{aligned} \tag{2-19}$$

This equation can be used to estimate $p$ and $q_1$, and subsequently an estimate of $x$ be obtained by using equations (2-16). Among the various estimators, the iterated extended Kalman filter (IEKF, [52, 53]) seems a reasonable choice for this nonlinear estimation problem. It should be noted that since we are not considering the dynamic equations of the vehicle, there would be no time updates for IEKF, only measurement updates.

#### 2.2.3.1. Iterated Extended Kalman Filter Equations

Next, we derive the equations for IEKF. The state to be estimated is

$$X = [p \quad q_1]^T. \tag{2-20}$$

and the measurement equations are

$$Z = h(X, n) \qquad n \sim (0, R), \tag{2-21}$$

$$Z = dB_1(B_2 - \Delta B_{stat}), \tag{2-22}$$

$$\begin{aligned} h(X, n) = {} & \big(B_1 - (B_2 - \Delta B_{stat})\big)p + d\big(B_1 + (B_2 - \Delta B_{stat})\big)q_1 - dq_1^2 \\ & + \big(-p - dq_1 + d(B_2 - \Delta B_{stat})\big)n_1 + (p + dB_1 - dq_1)n_2 - dn_1n_2 . \end{aligned} \tag{2-23}$$

The measurement update is performed as

$$K_k = P_{k-1}H_k^T(H_kP_{k-1}H_k^T + M_kR_kM_k^T)^{-1}, \tag{2-24}$$

$$\hat{X}_k = \hat{X}_{k-1} + K_k\big[Z_k - h_k\big(\hat{X}_{k-1}, 0\big)\big], \tag{2-25}$$

$$P_k = (I - K_kH_k)P_{k-1}, \tag{2-26}$$

$$\begin{aligned} H_k &= \left.\frac{\partial h_k}{\partial X}\right|_{\hat{X}_k^-} \\ &= \big[B_{1,k} - \big(B_{2,k} - \Delta B_{stat}\big) \qquad d\big(B_{1,k} + \big(B_{2,k} - \Delta B_{stat}\big) - 2\hat{q}_{1,k-1}\big)\big], \end{aligned} \tag{2-27}$$

$$\begin{aligned} M_k &= \left.\frac{\partial h_k}{\partial n}\right|_{\hat{X}_k^-} \\ &= \big[-\hat{p}_{k-1} + d\big(B_{2,k} - \Delta B_{stat} - \hat{q}_{1,k-1}\big) \qquad \hat{p}_{k-1} + d\big(B_{1,k} - \hat{q}_{1,k-1}\big)\big]. \end{aligned} \tag{2-28}$$

#### 2.2.3.2. Experimental Results

Applying the estimator to data obtained from experiments we should be able to estimate $p$ and $q_1$, and consequently get an estimate of distance. To verify the estimator, more tests were performed in which the vehicle moved toward the sensors from a distance and sensor outputs were recorded. Then a portion of the data in which, according to the sonar sensor, the vehicle was closer than $x_{th}$ to the sensors (or the magnetic

sensors seemed visually to be responding to the approaching vehicle) was selected and the designed IEKF estimator was applied. The results are shown in Figures 2-10 to 2-13.

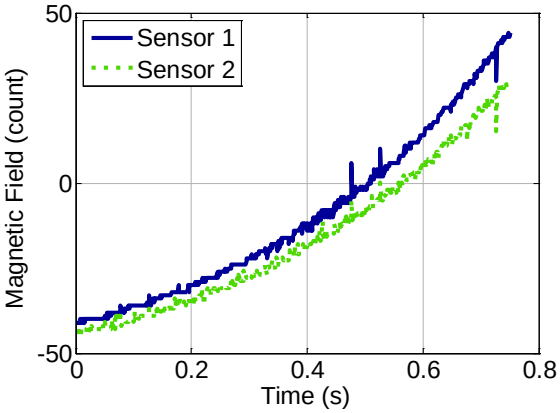


Figure 2-10. Measured magnetic fields by sensors 1 and 2 over time.

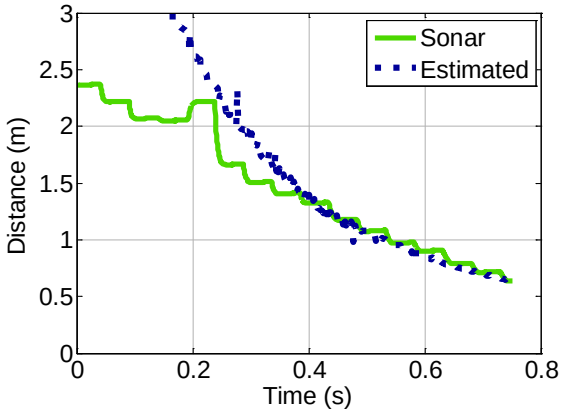


Figure 2-11. Distance estimated from magnetic sensors and measured by sonar sensor.

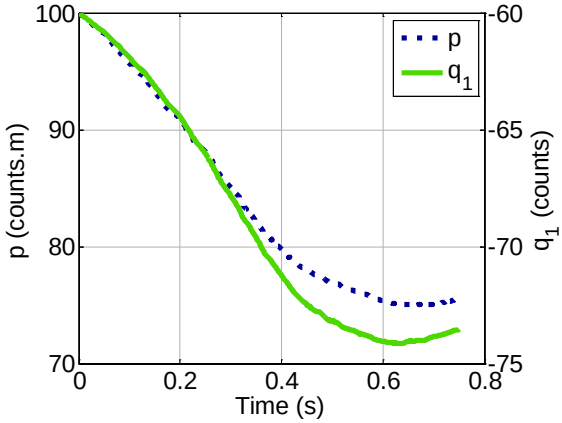


Figure 2-12. Estimated "$p$" and "$q_1$" over time.

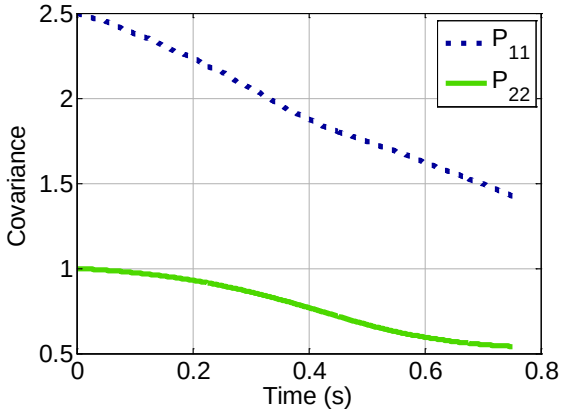


Figure 2-13. Covariance of states "$p$" and "$q_1$" over time.

Considering the results of the experiment, Figure 2-12 shows that the parameters $p$ and $q_1$ both converge in a period of about 0.6 s. The resulting position estimation, as seen in Figure 2-11, also converges very well to the position measured by the sonar sensor.

Being a nonlinear estimator, there are some issues with the designed estimator. First of all, the states appear not only in $H_k$ but also in $M_k$. This would make the nonlinear

estimator sensitive to initial conditions. Although $q_1$ would be close to $B1_{stat}$ and $q_{1,0}$ can be set close to its real value, $p$ changes a lot from one vehicle to another vehicle as shown in Table 1-1. It can be seen from Figure 2-11 that the initial value for $p$ was chosen to be $p_0 = 100$, not far from the final value. In this example, initial values higher than $\sim 100$ will cause the estimator not to converge in the time considered. This is a very critical issue for imminent crash detection. Very low initial values may also cause the estimator to diverge. One possible explanation is that very low initial values make the covariance of noise generally lower than what it is in reality. On the other hand, one may argue that an appropriate initial condition can be selected by using trial-and-error for different vehicles, however; $p$ changes a lot from one vehicle to another vehicle. In addition to selecting the initial values of the states, the initial values of the covariance of the states also play a role in convergence time and should be selected wisely.

To address these issues, a sensor fusion technique is developed that combine both magnetic and sonar sensors measurements. This technique addresses the aforementioned challenges and is discussed in the following section.

### 2.2.4. Sensor Fusion with Sonar Sensor for Improved Convergence

A sonar sensor can directly measure position with respect to itself independent of relative speed. It can measure larger distances compared with the magnetic sensors of several feet and typically will not be able to work at very short distances below 0.25 m. Furthermore, it has a narrow field of view at short distances. A sonar sensor typically has a refresh rate of only 50 ms. While this refresh rate is adequate for assistance during parking, it can be highly inadequate for an imminent crash detection and active passenger protection system. In comparison, the AMR sensors can achieve a very high Bandwidth of 5 MHz.

A sensor fusion system can be adopted to exploit the advantages of both types of sensors in order to overcome their individual drawbacks. Therefore, a new architecture is designed for the estimator using the finite state machine shown in Figure 2-14. In state 0, the estimator will use the sonar sensor to update position, since the magnetic sensors are not yet affected by the approaching vehicle. As soon as the magnetic sensors respond to the approaching vehicle, the estimator switches to state 1 and updates would be done using both sonar and magnetic sensors. When the vehicle enters a distance where the sonar sensor readings are invalid ($x(t_k) < x_{th-sonar}$) due to a small distance to the approaching object, the estimator switches to state 2 and updates would be done using only the magnetic sensors.

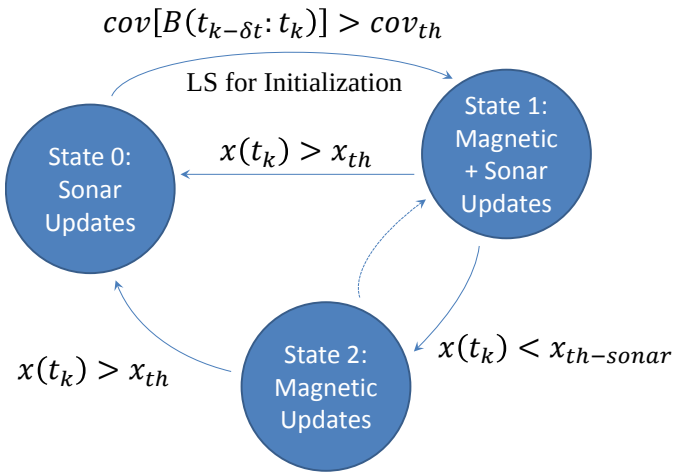


Figure 2-14. State machine diagram of the new estimator based on sensor fusion of sonar and magnetic sensors.

For transitions between the states in the finite state machine, $x_{th}$ would be the best variable to utilize for switching from state 0 to 1, but there is no prior knowledge about $x_{th}$ when a new vehicle is approaching. Therefore, the covariance of the magnetic sensors data at pre-determined time intervals can be used instead. Starting from state 0, whenever this covariance is higher than a threshold, the estimator switches to state 1 where updates are done with both sonar and magnetic sensors. To obtain more meaningful initial values for the states $p$ and $q_1$, a least squares (LS) fitting can be

performed at the switching time. The estimated values and their covariance are used as initial values of $p$ and $q_1$ and their covariance. While in state 1, $x_{th}$ can be calculated in real time and be used for determining if the vehicle is moving out of the "view" of the magnetic sensors so that the system switches back to state 0. Finally, $x_{th-sonar}$ is used to determine if the vehicle is getting very close to the sensors where the sonar sensor is not available anymore so that the system switches to state 2.

Next, we derive the IEKF equations for state 1 where the states are updated with both sonar and magnetic sensors measurements. In case of states 0 or 2, the IEKF measurement equations will be a reduced version of the measurement equations derived here. The state to be estimated is

$$X = [x \quad v \quad a \quad p \quad q_1]. \tag{2-29}$$

The system equations are

$$X_k = FX_{k-1} + Gw_{k-1} \qquad w_k \sim (0, Q_k), \tag{2-30}$$

$$F = \begin{bmatrix} 1 & dt & 0 & 0 & 0 \\ 0 & 1 & dt & 0 & 0 \\ 0 & 0 & 1 & 0 & 0 \\ 0 & 0 & 0 & 1 & 0 \\ 0 & 0 & 0 & 0 & 1 \end{bmatrix}, \tag{2-31}$$

$$G = [0 \quad 0 \quad 1 \quad 0 \quad 0]^T. \tag{2-32}$$

The measurement equations are

$$Z = h(X, n) \qquad n \sim (0, R), \tag{2-33}$$

$$Z = [x_s \quad B_1 \quad (B_2 - \Delta B_{stat})]^T, \tag{2-34}$$

$$h(X, n) = \left[x + n_x \quad \frac{p}{x} + q_1 + n_1 \quad \frac{p}{x + d} + q_1 + n_2\right]^T. \tag{2-35}$$

The time update equations would be

$$\hat{X}_k^- = F\hat{X}_{k-1}^+, \tag{2-36}$$

$$P_k^- = FP_{k-1}^+F^T + GQ_{k-1}G^T. \tag{2-37}$$

Finally, the measurement update equations would be as

$$K_k = P_k^- H_k^T (H_k P_k^- H_k^T + R_k)^{-1}, \tag{2-38}$$

$$\hat{X}_k^+ = \hat{X}_k^- + K_k\left[Z_k - h_k\left(\hat{X}_k^-, 0\right)\right], \tag{2-39}$$

$$P_k^+ = (I - K_k H_k)P_k^-, \tag{2-40}$$

$$H_k = \left.\frac{\partial h_k}{\partial X}\right|_{\hat{X}_k^-} = \begin{bmatrix} 1 & 0 & 0 & 0 & 0 \\ -\dfrac{\hat{p}_k^-}{(\hat{x}_k^-)^2} & 0 & 0 & \dfrac{1}{\hat{x}_k^-} & 1 \\ -\dfrac{\hat{p}_k^-}{(\hat{x}_k^- + d)^2} & 0 & 0 & \dfrac{1}{\hat{x}_k^- + d} & 1 \end{bmatrix}. \tag{2-41}$$

Now based on the value of the current state, the appropriate updates can be performed. The estimator is verified through different experiments which are discussed in the following section.

### 2.2.5. Experimental Results

In this section, we present the results of two different experiments verifying the performance of the developed position estimation system. The first experiment simulates a frontal/rear-end crash and involves position estimation of a Volkswagen Passat vehicle and a Chevrolet Impala vehicle. The second experiment simulates a side impact crash where a Ford vehicle door is used.

### 2.2.5.1. Frontal/Rear-end Impact Experiment

In this experiment, a Volkswagen Passat vehicle approached the sensors and moved away (between $t \cong 5$ s and $t \cong 15$ s), and then a Chevrolet Impala came close to the sensors and moved away (between $t \cong 20$ s and $t \cong 30$ s). The results are shown in Figures 2-15 to 2-18. The red circles in these figures indicate the time of transitions from state 0, where magnetic sensors measurements are not available to state 1, where magnetic sensors measurements are available and used in measurement updates.

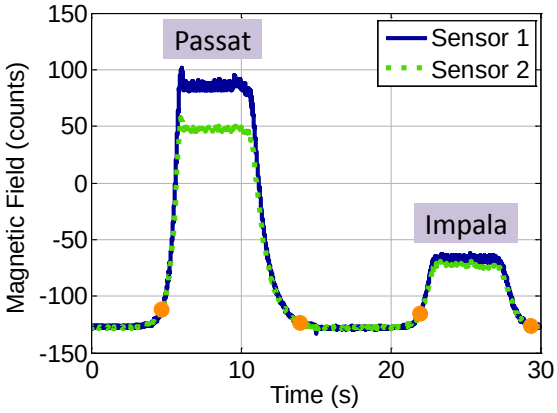


Figure 2-15. Measured magnetic fields over time.

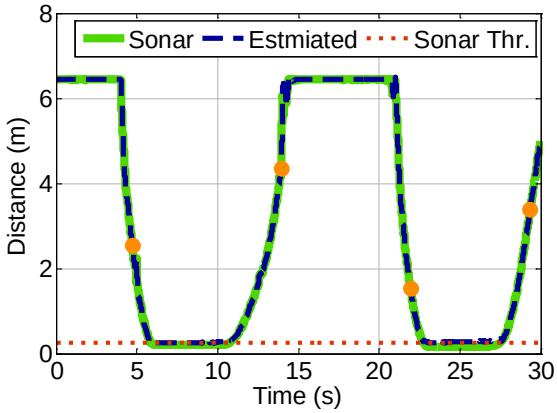


Figure 2-16. Estimated distance "$x$" over time.

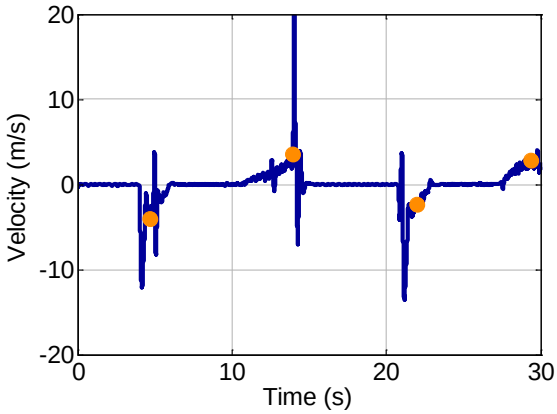


Figure 2-17. Estimated velocity "$v$" over time.

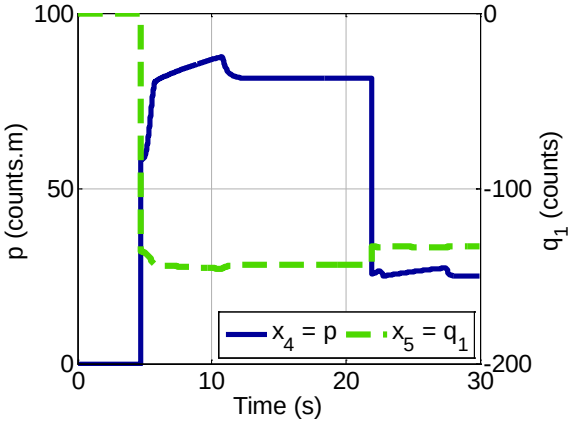


Figure 2-18. Estimated "$p$" and "$q_1$" over time.

As can be seen from the figures, the algorithm proposed to switch between states and get an initial value for $p$ and $q_1$ works very well. In spite of the change in vehicles that occurs between the Volkswagen Passat and the Chevrolet Impala during the experiment, $p$ converges quickly and changes in value between the two vehicles, as seen in Figure 2-18. Likewise the parameter $q_1$ also changes in value between the two vehicles. It can be seen that the final values of sonar distance and estimated distance in each scenario are not exactly the same. However, the sonar sensor is not rated as working at these low distances.

#### 2.2.5.2. Side Impact Experiment

The previous experiment resembles a case where a vehicle is approaching the side, front or rear of the host vehicle equipped with the imminent crash detection system. A new experiment was required to consider the case where the host vehicle, with the imminent crash detection system, is approaching the side of another vehicle for a side impact accident. Therefore, the door of a Ford passenger sedan was used as a part of the side of the vehicle and was put on a cart, so that it could be moved towards and away from the sensors. The door is shows in Figure 2-19.

Figure 2-19. The door of a Ford passenger sedan used for experiments.

On the other hand, to make sure that the sensor also works at very short distances, where the sonar measurements are invalid, narrow marking strips were fixed to the

ground apart from each other by 0.1 m. Using the strips, we can compare the steady state values of distance from the developed estimator with actual marked distance. The results are shown in Figures 2-20 to 2-23.

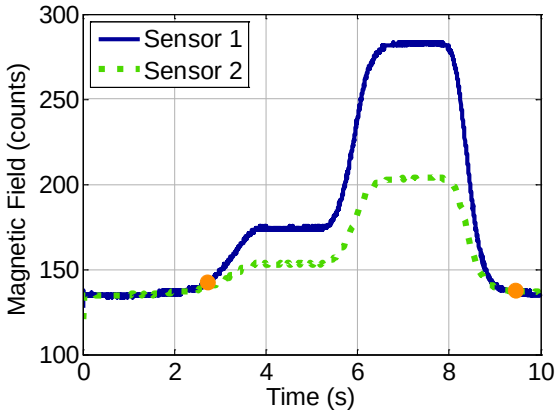


Figure 2-20. Measured magnetic fields over time.

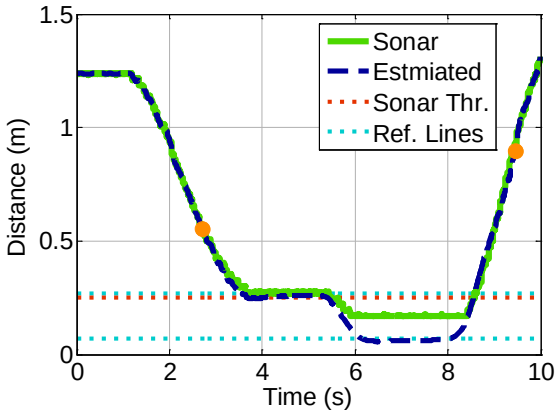


Figure 2-21. Estimated distance "$x$" over time.

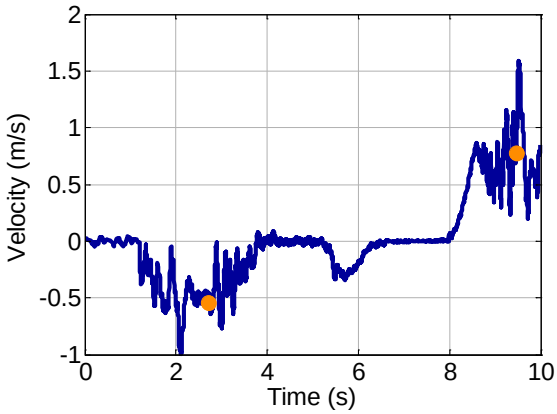


Figure 2-22. Estimated velocity "$v$" over time.

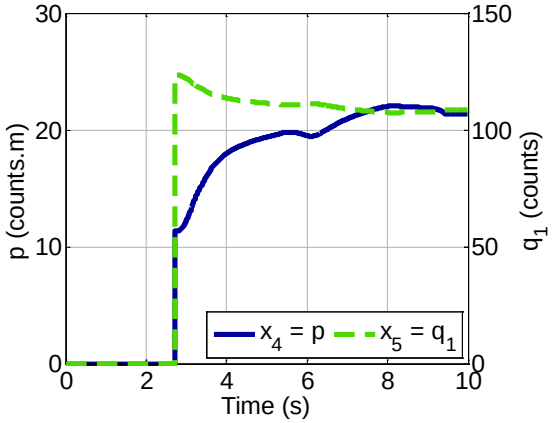


Figure 2-23. Estimated "$p$" and "$q_1$" over time.

The results show that the estimation algorithm works very well for this side impact scenario as well. The distance estimated matches the distance measured by the sonar up to 0.25 m. It also matches the distance marked by the marking strips at smaller distances below 0.25 m. As can be seen from Figure 2-21, the estimator steady state value is very close to the reference line. Indeed, the maximum absolute error is less than 0.013 m. In

the next section, we consider the problem of predicting a crash anywhere in the 2-D plane around a vehicle.

## 2.3. Two-dimensional Position Estimation

For 1-D motion, in which the vehicle is moving directly towards or away from the sensors, we found that below a threshold distance, $x_{th}$, the relation expressed by (2-12) can be assumed between magnetic field and distance. That relationship could be used together with an adaptive estimator for real-time estimation of position just prior to a frontal or rear-end collision. However, an impact due to collision can occur at any location around the car body. In fact, side impact and oblique collisions at rural intersections are a significant source of fatalities [54]. Therefore, it is necessary to be able to estimate not only the relative position, but also the orientation of the colliding vehicle anywhere in the 2-D plane.

To further investigate the 2-D motion problem, we first consider a simplified case in which the vehicle is moving toward the sensors at a constant angle $\theta$, as shown in Figure 2-24.

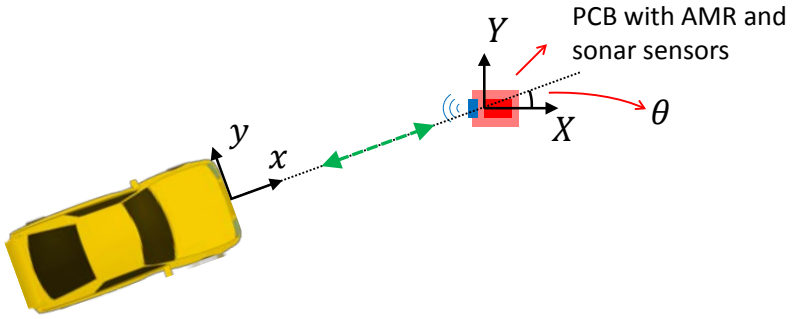


Figure 2-24. Vehicle moving toward sensors at a constant angle.

In this case, if the angle $\theta$ is known, the magnetic field along the direction of motion of the vehicle can be expressed in terms of the magnetic sensors measurements as

$$B = B_{xAMR}\cos\theta + B_{yAMR}\sin\theta = \frac{p}{r} + q, \tag{2-42}$$

where $r$ is the distance measured along the direction of motion. This equation can potentially be used with an adaptive algorithm to estimate $r$. However, if $\theta$ is not constant, or if the colliding vehicle is moving toward the sensors at an offset (meaning that its centerline does not pass through the center of the magnetic sensor), the above approach cannot be adopted.

Therefore, to fully identify and classify a crash in 2-D motion, we need to estimate $x_A$, $y_A$, $v$, $\theta$, and $\omega$ as shown in Figure 2-25, where $x_A$ and $y_A$ are the position of point $A$ with respect to the coordinate frame attached to the approaching car, $v$ is the longitudinal velocity of approaching car along its $x$-axis, $\theta$ is the orientation of the approaching car relative to the host car (in other words, it is the angle between the $x$-axis of the coordinate frame attached to the approaching car and $X$-axis of the coordinate frame at point $A$) and $\omega$ is the rotational velocity of the approaching car.

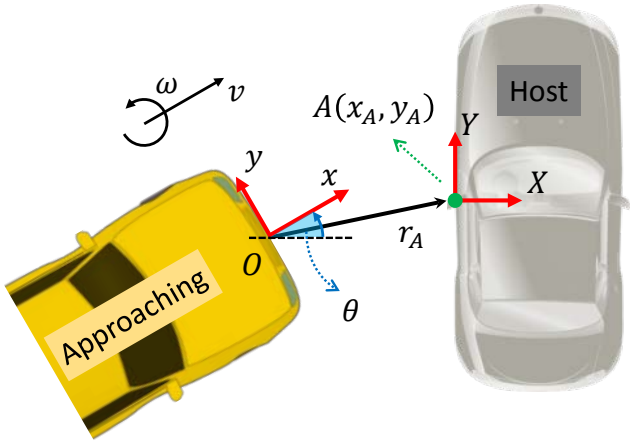


Figure 2-25. Two-dimensional position estimation and the parameters to be estimated.

It is worth mentioning that another way of expressing the position of the objects would be to express the position of point $O$ with respect to coordinate frame attached to point $A$. However, using this coordinate frame, the measurement equations which are derived later on, will be more complicated.

Use of magnetic field for estimation of vehicle position in 2-D motion is much more complicated than in the 1-D motion not only because of the additional degrees-of-freedom (DOF) for the vehicle, but also because of the complex pattern of the vehicle's magnetic field in two-dimensional space. The magnetic field lines are not parallel to each other and they curve out to the sides. This is the same with any type of magnetic objects. Figure 2-26 shows the magnetic field lines of a rectangular magnet.

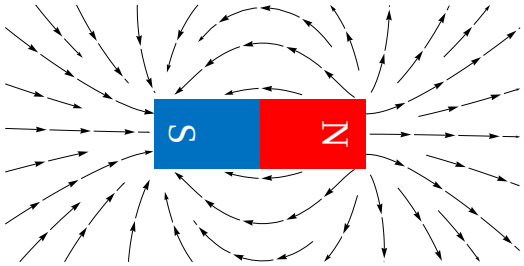


Figure 2-26. Magnetic Field lines of a magnetic bar.

This phenomenon can be also observed in the experiments with the door of a Ford passenger sedan shown in Figure 2-19. The door is mounted on a wheeled platform and can be maneuvered and moved easily towards or away from the sensors in different directions.

Figure 2-27 shows a case where the door is moving toward a set of four magnetic sensors at a 45-degree angle. The sensor readings at four different positions of the door during its motion are shown. As seen from Figure 2-27, initially, the direction of the magnetic field (shown with a green dashed line) is very different from the normal direction of the door. Thus, it is not possible to obtain the orientation of the door $\theta$, by only determining the direction of the measured magnetic fields. It can be also seen that as the door gets closer, the magnetic field magnitude increases and its direction changes to become in line with the normal direction of the door.

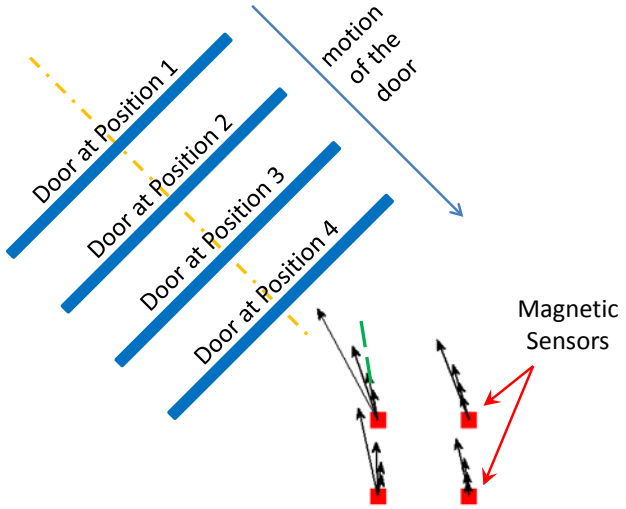


Figure 2-27. Magnetic field of the door while moving toward magnetic sensors at 45 degrees.

To further investigate a vehicle's magnetic field, a mathematical expression for magnetic field in a two-dimensional plane around a rectangular magnetic body is derived in the next section.

### 2.3.1. Derivation of a Mathematical Expression for Magnetic Field in 2-D

Modeling a vehicle as a rectangular block of magnetic dipoles, as shown in Figure 2-28, we want to obtain a mathematical expression for the magnetic field at an arbitrary point $A$. It is assumed that the height of the block $da$ is small with respect to its width and length. Note that the same assumption was used in derivation of the magnetic field model in 1-D described in Section 2.2.1. Here, the only difference is that we make this assumption from the beginning of the derivation so as to derive a closed form formula for the magnetic field in 2-D. While such a magnetic field approximation for a vehicle body might at first appear crude, the model obtained from such an assumption, together with parameter estimation, is likely to be significantly more useful than a purely

empirical function obtained without any magnetic field models. The goal is to later use the derived magnetic field equations and estimate vehicle position by measuring $B_x$ and $B_y$ using a magnetic sensor at point $A$.

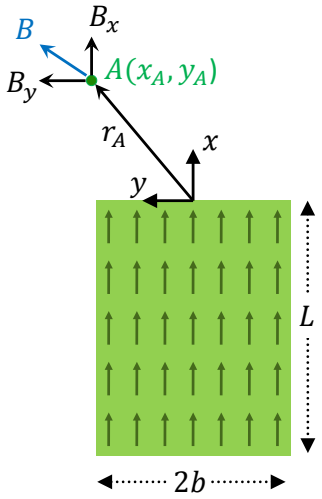


Figure 2-28. Analysis of magnetic field around a magnetic block in 2-D.

As a first step, the magnetic field of a line of magnetic dipoles (shown in Figure 2-29) is obtained.

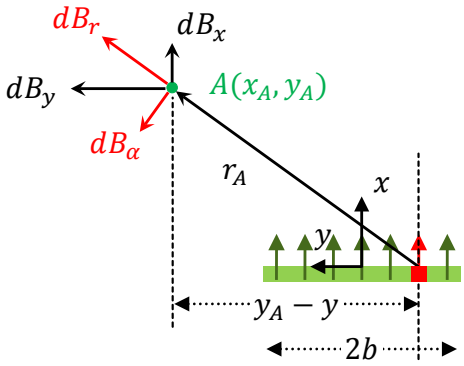


Figure 2-29. Analysis of magnetic field of line of dipoles.

According to [41], the following relations can be written down:

$$dB_r = \frac{\mu_0 dm_0}{2\pi r^3}\cos\alpha, \tag{2-43}$$

$$dB_\alpha = \frac{\mu_0 dm_0}{4\pi r^3} \sin\alpha. \tag{2-44}$$

In order to obtain $B_x$ and $B_y$ we need to integrate $dB_x$ and $dB_y$ which are given by the following equations:

$$dB_x = dB_r \cos\alpha - dB_\alpha \sin\alpha, \tag{2-45}$$

$$dB_y = dB_r \sin\alpha + dB_\alpha \cos\alpha. \tag{2-46}$$

Expressing $r$ and $\alpha$ in terms of $x$ and $y$ we have:

$$r = (x_A^2 + (y_A - y)^2)^{\frac{1}{2}}, \tag{2-47}$$

$$\alpha = \text{atan}\left(\frac{y_A - y}{x_A}\right), \tag{2-48}$$

$$\sin\alpha = \frac{y_A - y}{(x_A^2 + (y_A - y)^2)^{\frac{1}{2}}}, \tag{2-49}$$

$$\cos\alpha = \frac{x_A}{(x_A^2 + (y_A - y)^2)^{\frac{1}{2}}}. \tag{2-50}$$

Therefore, we can write $dB_x$ and $dB_y$ as:

$$dB_x = \frac{\mu_0 dm_0}{4\pi r^3}(2\cos^2\alpha - \sin^2\alpha) = \frac{\mu_0 dm_0}{4\pi}\frac{2x_A^2 - (y_A - y)^2}{(x_A^2 + (y_A - y)^2)^{\frac{5}{2}}}, \tag{2-51}$$

$$dB_y = \frac{\mu_0 dm_0}{4\pi r^3} 3\cos\alpha \sin\alpha = \frac{\mu_0 dm_0}{4\pi}\frac{3x_A(y_A - y)}{(x_A^2 + (y_A - y)^2)^{\frac{5}{2}}}. \tag{2-52}$$

The magnetic field generated by the line of magnetic dipoles is then obtained by integrating the above terms:

$$B_{x-l}(x_A, y_A) = \frac{\mu_0 m_0 da\, dx}{4\pi} \int_{-b}^{b} \frac{2x_A^2 - (y_A - y)^2}{(x_A^2 + (y_A - y)^2)^{\frac{5}{2}}} dy$$

$$= \frac{\mu_0 m_0 da\, dx}{4\pi} \left( \frac{2x_A^2(y_A + b) + (y_A + b)^3}{x_A^2(x_A^2 + (y_A + b)^2)^{\frac{3}{2}}} - \frac{2x_A^2(y_A - b) + (y_A - b)^3}{x_A^2(x_A^2 + (y_A - b)^2)^{\frac{3}{2}}} \right), \tag{2-53}$$

$$B_{y-l}(x_A, y_A) = \frac{\mu_0 m_0 da\, dx}{4\pi} \int_{-b}^{b} \frac{3x_A(y_A - y)}{(x_A^2 + (y_A - y)^2)^{\frac{5}{2}}} dy$$

$$= \frac{m_0 da\, dx}{4\pi} \left( -\frac{x_A}{x_A^2(x_A^2 + (y_A + b)^2)^{\frac{3}{2}}} + \frac{x_A}{x_A^2(x_A^2 + (y_A - b)^2)^{\frac{3}{2}}} \right). \tag{2-54}$$

In order to obtain the total magnetic field created by the whole bar, $B_{x-l}$ and $B_{y-l}$ can be integrated in the $X$ direction as

$$B_x = \int_{x_A}^{x_A+L} B_{x-l}(x, y_A) = \frac{\mu_0 m_0 da}{4\pi} \left( -\frac{y_A + b}{(x_A + L)((x_A + L)^2 + (y_A + b)^2)^{\frac{1}{2}}} \right.$$

$$+ \frac{y_A - b}{(x_A + L)((x_A + L)^2 + (y_A - b)^2)^{\frac{1}{2}}} + \frac{y_A + b}{x_A(x_A^2 + (y_A + b)^2)^{\frac{1}{2}}} \tag{2-55}$$

$$\left. - \frac{y_A - b}{x_A(x_A^2 + (y_A - b)^2)^{\frac{1}{2}}} \right),$$

$$B_y = \int_{x_A}^{x_A+L} B_{y-l}(x, y_A) = \frac{\mu_0 m_0 da}{4\pi} \left( \frac{1}{((x_A + L)^2 + (y_A + b)^2)^{\frac{1}{2}}} \right.$$

$$\left. - \frac{1}{((x_A + L)^2 + (y_A - b)^2)^{\frac{1}{2}}} - \frac{1}{(x_A^2 + (y_A + b)^2)^{\frac{1}{2}}} + \frac{1}{(x_A^2 + (y_A - b)^2)^{\frac{1}{2}}} \right). \tag{2-56}$$

The equations for magnetic field derived as (2-55) and (2-56) are complex and not suitable for real-time estimation of both equation parameters and position. However, it is possible to simply (2-55) and (2-56) for the colored region shown in Figure 2-30 for which we have $|y_A| \ll b$ and $x_A \leq x_{th}$.

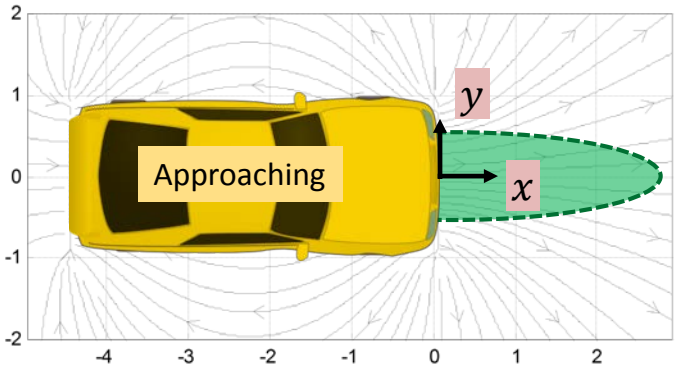


Figure 2-30. Magnetic field equations are simplified for the colored region.

Assuming $x_A + L \gg x_A$, (2-55) and (2-56) can be simplified to

$$B_x = \frac{\mu_0 m_0 da}{4\pi}\left(\frac{y_A + b}{x_A(x_A^2 + (y_A + b)^2)^{\frac{1}{2}}} - \frac{y_A - b}{x_A(x_A^2 + (y_A - b)^2)^{\frac{1}{2}}}\right), \tag{2-57}$$

$$B_y = \frac{\mu_0 m_0 da}{4\pi}\left(-\frac{1}{(x_A^2 + (y_A + b)^2)^{\frac{1}{2}}} + \frac{1}{(x_A^2 + (y_A - b)^2)^{\frac{1}{2}}}\right). \tag{2-58}$$

Next, if we assume that $y_A$ is small and close to zero, (2-57) and (2-58) can be further simplified to the following equations:

$$B_x = \frac{\mu_0 m_0 da}{2\pi}\frac{b}{x_A(x_A^2 + b^2)^{\frac{1}{2}}} + f(p, b, x_A)y^2 + \cdots \cong \frac{\mu_0 m_0 da}{2\pi}\frac{b}{x_A(x_A^2 + b^2)^{\frac{1}{2}}}, \tag{2-59}$$

$$B_y = \frac{\mu_0 m_0 da}{2\pi}\frac{b}{(x_A^2 + b^2)^{\frac{3}{2}}}y + f(p, b, x_A)y^3 + \cdots \cong \frac{\mu_0 m_0 da}{2\pi}\frac{by}{(x_A^2 + b^2)^{\frac{3}{2}}}. \tag{2-60}$$

Note that (2-59) is the same as the equation obtained earlier for one-dimensional case (2-10) replacing $da$ with $2a$. For small values of $x_A$ , (2-59) and (2-60) can be simplified further as

$$B_x = \frac{\mu_0 m_0 da}{2\pi} \frac{1}{x_A \left(1 + \left(\frac{x_A}{b}\right)^2\right)^{\frac{1}{2}}} \cong \frac{\mu_0 m_0 da}{2\pi x_A} = \frac{p}{x_A}, \tag{2-61}$$

$$B_y = \frac{\mu_0 m_0 da}{2\pi} \frac{by}{(x_A^2 + b^2)^{\frac{3}{2}}} = \frac{pby}{(x_A^2 + b^2)^{\frac{3}{2}}}. \tag{2-62}$$

If there exists any static magnetic field at point $A$, like the Earth's magnetic field, a constant needs to be added to the above equations to obtain the total magnetic field to be measured by the sensors. Thus we have:

$$B_x = \frac{p}{x_A} + q_x, \tag{2-63}$$

$$B_y = \frac{pby}{(x_A^2 + b^2)^{\frac{3}{2}}} + q_y. \tag{2-64}$$

It is also possible to subtract the static magnetic field at the location of magnetic sensors from the measurements to avoid adding a constant to readings from magnetic sensors. However, for readings of $B_x$, it was observed that even when subtracting the static magnetic field from the measurements, using (2-63) results in a better fit compared with using (2-59). Therefore, the following equations are being used for position estimation in the next sections of this chapter:

$$B_x = \frac{p}{x_A} + q, \tag{2-65}$$

$$B_y = \frac{pby}{(x_A^2 + b^2)^{\frac{3}{2}}}. \tag{2-66}$$

In order to use (2-65) and (2-66) for position estimation by measuring the magnetic field, we need to make sure that the magnetic sensors are in the colored region shown in Figure 2-30 for which we have simplified the magnetic field equations. For the points inside this region, the ratio $|B_y/B_x|$ is small. Therefore, we can install multiple magnetic sensors around the host vehicle and check the ratio $|B_{yi}/B_{xi}|$ for each magnetic sensor, and pick the sensors with the lowest ratio as the most appropriate sensor to utilize for position estimation. This concept is shown in Figure 2-31.

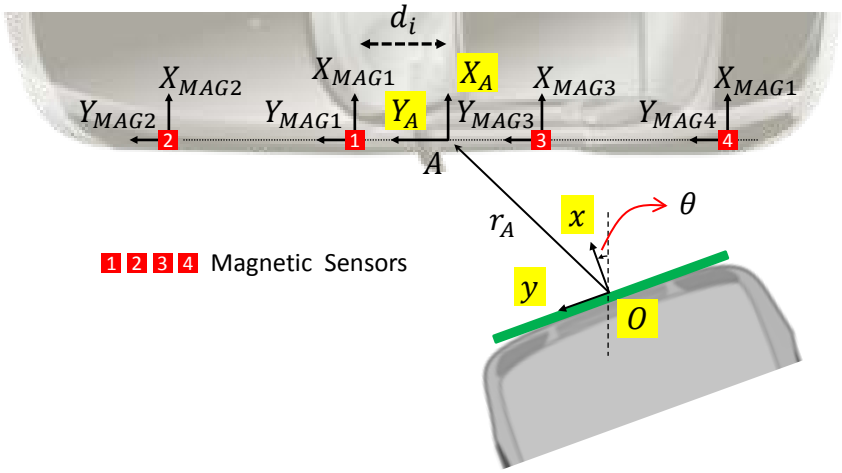


Figure 2-31. Magnetic sensors arrangements for 2-D position estimation.

Each magnetic sensor measures magnetic field along its $X$ and $Y$ axes, $B_{xMAGi}$ and $B_{yMAGi}$. Thus, the magnetic field of the approaching vehicle at the location of magnetic sensor $i$ expressed in the approaching vehicle coordinate frame can be obtained as

$$\begin{cases} B_{xi} = B_{xMAGi}\, cos(\theta) + B_{yMAGi} sin(\theta), \\ B_{yi} = -B_{xMAGi}\, sin(\theta) + B_{yMAGi} cos(\theta). \end{cases} \tag{2-67}$$

As can be seen from (2-67), to calculate the ratio $|B_{yi}/B_{xi}|$ in order to select the most appropriate magnetic sensors for measurement update, we at least need an initial

estimate of $\theta$. Therefore, a custom-designed sonar system (working at ultrasonic frequency of 40 KHz) has been developed which measures both the distance to the object as well as its orientation. The sonar system detects the objects at longer distances compared with magnetic sensors. Therefore, when the magnetic sensors respond to the presence of a car, the estimated $\theta$ from the sonar system can be used to select the most appropriate magnetic sensors for measurement updates. The measurements from the sonar system are also used to initialize the magnetic field parameters which speeds up the convergence of the magnetic field parameters. The sonar system is described in the following section.

### 2.3.2. Development of a Custom-designed Sonar Measurement System

The developed sonar measurement system includes one transmitter, $T$, at point $A$ and two receivers, $R_1$ and $R_2$, at distances $d_1$ and $d_2$ from $A$ arranged in the order shown in Figure 2-32. This configuration of the transmitter and the receivers makes it possible to measure the orientation of the target as well as its distance from the sensors.

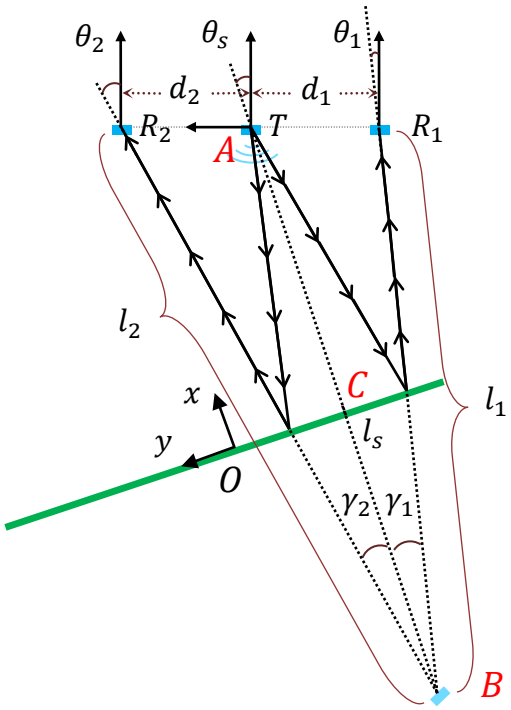


Figure 2-32. Sonar system with one transmitter and two receivers.

Measuring the travel time of sound for receivers 1 and 2, the distance that the echo pulse has traveled can be calculated. Using the fact that the incident and reflected angles of sound are the same (similar to light when it reflects from a mirror), it can be concluded that the measured distances equal $l_1$ and $l_2$ shown in Figure 2-32. In other words, $l_1$ and $l_2$ equal the distance from the image of transmitter $T$ at point $B$ to the receivers $R_1$ and $R_2$ respectively.

Knowing $l_1$ and $l_2$ and the distance between the transmitter and the receivers, $d_1$ and $d_2$ , the angle $\theta_2$ can be calculated using the cosine rule as

$$d_s = d_1 + d_2, \tag{2-68}$$

$$l_1^2 = d_s^2 + l_2^2 - 2d_s l_2 \cos(90 - \theta_2), \tag{2-69}$$

$$\theta_2 = \text{asin}\left(\frac{d_s^2 + l_2^2 - l_1^2}{2d_s l_2}\right). \tag{2-70}$$

Knowing $\theta_2$, the length $l_s$, the distance between the transmitter and its image ($\overline{AB}$), can be calculated using the cosine rule as

$$l_s^2 = d_2^2 + l_2^2 - 2d_2 l_2 \cos(90 - \theta_2). \tag{2-71}$$

Then $x_s$ ($\overline{AC}$), the sonar estimate of $x_A$, can be calculated from $l_s$ since

$$x_s = \frac{l_s}{2}. \tag{2-72}$$

Applying cosine rule one more time, $\theta_s$, sonar estimate of $\theta$, can be also calculated as

$$l_2^2 = d_2^2 + l_s^2 - 2d_2 l_s \cos(90 + \theta_s), \tag{2-73}$$

$$\theta_s = \text{asin}\left(\frac{l_2^2 - d_2^2 - l_s^2}{2d_2 l_s}\right). \tag{2-74}$$

In practice, the measured signals from the sonar system are $l_{1m}$ and $l_{2m}$, where

$$\begin{cases} l_{1m} = l_1 + n_1 & n_1 \sim N(0, \sigma_s), \\ l_{2m} = l_2 + n_2 & n_2 \sim N(0, \sigma_s). \end{cases} \tag{2-75}$$

If we want to use $x_s$ and $\theta_s$ in the estimator, we should also calculate the covariance of noise in the measurements. Since $x_s$ and $\theta_s$ have nonlinear relations with $n_1$ and $n_2$, we need to calculate the derivatives of $x_s$ and $\theta_s$ with respect to $n_1$ and $n_2$ which would be

$$\frac{\partial x_s}{\partial n_1} = -\frac{l_{1m}}{2l_s}\frac{d_2}{d_s}, \tag{2-76}$$

$$\frac{\partial x_s}{\partial n_2} = \frac{l_{2m}}{2l_s}\frac{d_1}{d_s}, \tag{2-77}$$

$$\frac{\partial \theta_s}{\partial n_1} = \frac{\cos(\gamma_2)}{\cos(\theta_s)}\frac{l_{1m}l_{2m}}{d_s l_s^2}, \tag{2-78}$$

$$\frac{\partial \theta_s}{\partial n_2} = \frac{\cos(\gamma_1)}{\cos(\theta_s)}\frac{l_{1m}l_{2m}}{d_s l_s^2}. \tag{2-79}$$

Similar to any sonar sensor used for 1-D position measurements, the developed sonar system will not also work at close proximities (typically below $0.25$ m). Also, the sonar system will not work if the orientation of the object, $\theta$, increases so that $\theta_1$ and $\theta_2$ are greater than the beam angles of the transducers. It should be mentioned that the threshold for $\theta$ is not constant and changes slightly with the distance from the object. Therefore, there cannot be a constant value for $\theta_{threshold}$. However, an easier way of detecting outliers is at the beginning of the calculation by looking at the values obtained for $\theta_1$ and $\theta_2$. If they have imaginary values then a outlier is detected. This method for detecting outliers and is described later in this section.

It is also worth mentioning that the sonar system alone is not able to determine $y_A$. In other words, the object can move arbitrary along its $y$-axis and the sonar readings will remain the same. Finally, the sonar system has a much lower refresh rate ($20$ Hz) compared with AMR sensors ($1$ KHz). Therefore, the use of the AMR sensors is critical.

***Addressing crosstalk and multipath problems of sonar system:*** Problems with crosstalk and multipath returns are addressed in three different layers of the proposed system: design level, sonar sensor level and estimator level.

1. *Design level:* The sonar transmitter is set to send out a signal every $50$ ms and each receiver hears back the signal that returns to it. After the first signal has been detected, the receivers ignore any returning signals until the next signal is transmitted. The voltage level of the signal sent to the transmitter and the time

duration of $50$ ms are design parameters. The voltage level is set such that the sonar system is not able to detect objects more than $\sim 6$ m away. Since the speed of sound is about $340$ m/s, all the possible returns are within $dt = 2 * 6/340$ ms $= 35$ ms of the transmitted signal. Therefore, transmitting signals every $50$ ms ensures that there will not be any returns from a previous transmit to interfere with the current measurement.

2. *Sonar sensor level:* The designed sonar system includes one transmitter and two receivers. Using the two receivers, it is possible to measure the distance to the object as well as its orientation. On the other hand, having two receivers provides another level of robustness. As an example assume that there is an object at a distance of $x_A = 2$ m in front of the sonar system at angle of $\theta = 20°$. The raw readings from the two receivers will be $l_1 = 3.95$ m and $l_2 = 4.05$ m from which $x_s$ and $\theta_s$ can be calculated as described by (2-68) through (2-74). Now let's assume that due to a multipath or crosstalk error, $l_1$ be measured as $l_1' = 3$ m. This will cause the argument of the "asin" function in (2-70) to be larger than 1 resulting in an imaginary value for $\theta_2$. Therefore, by looking at the values obtained for $\theta_1$ and $\theta_2$, we can determine if the readings are valid or not. This adds another level of robustness against multipath and crosstalk errors.
3. *Estimator Level:* Finally, in the estimator, the "Mahalanobis distance" is used to reject outliers of the sonar sensing system. The Mahalanobis distance is defined as

$$d_{mah-k} = \left((x_{s-k} - \hat{x}_k^-)(P_{x-k}^-)^{-1}(x_{s-k} - \hat{x}_k^-)\right)^{0.5}, \tag{2-80}$$

where $x_{s-k}$ is the measured distance from sonar system, $\hat{x}_k^-$ is the a priori estimated distance and $P_{x-k}^-$ is the a priori covariance of the estimated distance. For a given $P_{x-k}^-$, the further the measurement is from the predicted estimate, the larger is the Mahalanobis distance. For a certain distance between the

measurement and predicted estimate, the smaller the uncertainty in the predicted estimate, the larger is the Mahalanobis distance. In other words, as we are more certain about the current estimate, we reject a measurement with a shorter distance to the predicted estimate compared with the case that we are less certain about the current estimate and we allow larger distance between the measurement and estimated distance. Figure 2-40 in Section 2.3.4.1 shows how the Mahalanobis distance is used to reject sonar outliers in the experiment with the vehicle door.

### 2.3.3. Extended Kalman Filter for Two-dimensional Position and Orientation Estimation

As mentioned earlier, the current 2-D crash prediction system is based on four magnetic sensors and a sonar system consisting of three sonar transducers. The sensors configuration is shown in Figure 2-33.

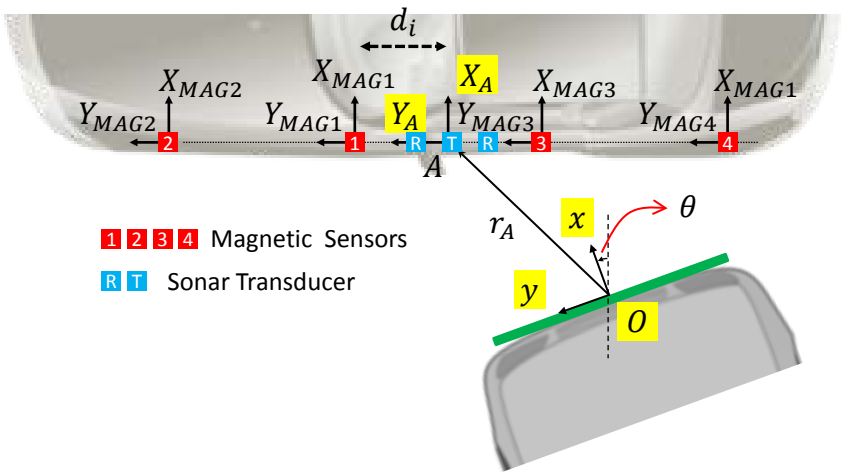


Figure 2-33. Magnetic sensors and sonar transducers arrangements for 2-D position estimation.

The sonar sensing system works at larger distances compared with magnetic sensors, however, it does not work at short distances. To account for the different working ranges

of the sensors, a state machine shown in Figure 2-34 is utilized. In state 0, the estimator will use the sonar sensor to update position, since the magnetic sensors are not yet affected by the approaching vehicle. As soon as the magnetic sensors respond to the approaching vehicle, updates would be done using both sonar and magnetic sensors (state 1). When the vehicle enters a distance where the sonar readings are not valid any more due to very small distances or an outlier is detected in the measurements from the sonar system, updates would be done using only the magnetic sensors (state 2).

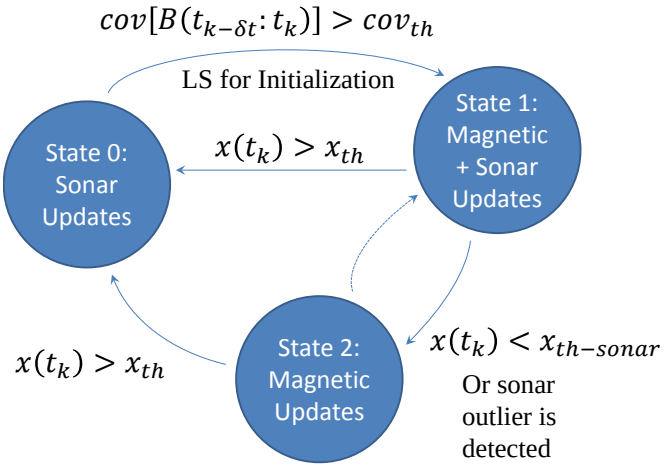


Figure 2-34. Two-dimensional sensor system state diagram.

For transitions between the states in the finite state machine, $x_{th}$ would be the best variable to utilize for switching from state 0 to 1, but there is no prior knowledge about $x_{th}$ when a new vehicle is approaching. Therefore, the covariance of the magnetic sensors data at pre-determined time intervals can be used instead. Starting from state 0, whenever the covariance is higher than a threshold, the estimator switches to state 1 where updates are done with both sonar and magnetic sensors. To obtain more meaningful initial values for the states $p$ and $q$, a least squares (LS) fitting can be performed at the switching time. The estimated values and their covariance are used as initial values for $p$, $q$ and their covariance. While in state 1, $x_{th}$ can be calculated in real time and be used for determining if the vehicle is moving out of the "view" of the

magnetic sensors so that the system switches back to state 0. Finally, $x_{th-sonar}$ is used to determine if the vehicle is getting very close to sensors where the sonar system is not available anymore so that the system switches to state 2.

The new sonar system also measures the orientation of the object, $\theta$, and if $\theta$ increases beyond a threshold, it will not be able to measure the orientation due to the limitations in the beam width of the sonar transducers which also results in a transition from state 1 to state 2.

The extended Kalman filter (EKF) [52, 53] is used for estimation of magnetic field equation parameters as well as position, orientation, and velocity of the approaching vehicle. There are some tight time constraints with the real-time 2-D positioning system. Sensors data are captured through two Microchip dsPIC microcontrollers and transferred to MATLAB running on a PC at 500 Hz via serial port. Since the system is working in real time, there would be a time period of 2 ms for transferring data from microcontrollers to MATLAB (taking about 0.5 ms), analyzing the data, and visualizing the results. Having an EKF running in MATLAB (described in later sections), it means that there is about 1.5 ms to perform time update and measurement update steps of the EKF. Therefore the measurement equations should be simplified as much as possible. For instance, it is possible to use equations obtained earlier for the magnetic field in 2-D without any simplifying assumptions. However, calculating the Jacobian required for EKF measurement update will become complicated and computationally intense. It is also worth mentioning that the ordinary unscented Kalman filter [55, 56] fails in this problem mainly because of the discontinuity at $x = 0$.

With the aforementioned explanations, we will derive the equations for time update and measurement update of the EKF. It should be noted that the equations presented here are the general equations used in state 1 where both sonar and magnetic sensors measurements are available. In case of states 0 or 2, the Kalman filter measurement

equations will be a reduced version of the measurement equations derived here. The state vector to be estimated is as

$$X = [x \quad y \quad v \quad a \quad \theta \quad \omega \quad \alpha \quad p \quad q]^T, \tag{2-81}$$

where $x$, $y$ and $\theta$ express the position and orientation of the object, $v$ and $\omega$ are the longitudinal and rotational velocity of the object, $a$ and $\alpha$ are longitudinal and rotational accelerations, and $p$ and $q$ are the magnetic field model parameters.

***Time update equations:***

In order to obtain the time update equations of the EKF, we need to derive the dynamic equations of the system. Considering Figure 2-25, it is assumed that the object moves with a longitudinal velocity $v$ along its $x$-axis and a rotational velocity $\omega$. Using the transport theorem, the dynamic equations can be written down as

$$\begin{aligned} &\dot{r}_A = (\dot{r_A})_{rel} + \omega \times r_A \\ &\Rightarrow \dot{x}_A = -v + \omega y_A \;\&\; \dot{y}_A = -\omega x_A. \end{aligned} \tag{2-82}$$

Discretizing the above equations, dropping the $A$ subscript and including longitudinal and rotational accelerations, the following equations for the dynamics of the system are obtained:

$$X_k = f(X_{k-1}, w_{k-1}) \quad w_k \sim (0, Q_k), \tag{2-83}$$

$$x_k = x_{k-1} - v_{k-1}dt + \omega_{k-1}y_{k-1}dt, \tag{2-84}$$

$$y_k = y_{k-1} - \omega_{k-1}x_{k-1}dt, \tag{2-85}$$

$$v_k = v_{k-1} + a_{k-1}dt, \tag{2-86}$$

$$a_k = a_{k-1} + w_{k-1}^1, \tag{2-87}$$

$$\theta_k = \theta_{k-1} + \omega_{k-1}dt, \tag{2-88}$$

$$\omega_k = \omega_{k-1} + \alpha_{k-1}dt, \tag{2-89}$$

$$\alpha_k = \alpha_{k-1} + w_{k-1}^2, \tag{2-90}$$

$$p_k = p_{k-1} + w_{k-1}^3, \tag{2-91}$$

$$q_k = q_{k-1} + w_{k-1}^4. \tag{2-92}$$

The time update equations will be as

$$\hat{X}_k^- = f_{k-1}\left(\hat{X}_{k-1}^+, 0\right), \tag{2-93}$$

$$P_k^- = F_{k-1}P_{k-1}^+F_{k-1}^T + G_{k-1}Q_{k-1}G_{k-1}^T, \tag{2-94}$$

$$F_{k-1} = \left.\frac{\partial f_{k-1}}{\partial X}\right|_{\hat{X}_{k-1}^+} = \begin{bmatrix} 1 & \hat{\omega}_{k-1}^+dt & -dt & 0 & 0 & \hat{y}_{k-1}^+dt & 0 & 0 & 0 \\ -\hat{\omega}_{k-1}^+dt & 1 & 0 & 0 & 0 & -\hat{x}_{k-1}^+dt & 0 & 0 & 0 \\ 0 & 0 & 1 & dt & 0 & 0 & 0 & 0 & 0 \\ 0 & 0 & 0 & 1 & 0 & 0 & 0 & 0 & 0 \\ 0 & 0 & 0 & 0 & 1 & dt & 0 & 0 & 0 \\ 0 & 0 & 0 & 0 & 0 & 1 & dt & 0 & 0 \\ 0 & 0 & 0 & 0 & 0 & 0 & 1 & 0 & 0 \\ 0 & 0 & 0 & 0 & 0 & 0 & 0 & 1 & 0 \\ 0 & 0 & 0 & 0 & 0 & 0 & 0 & 0 & 1 \end{bmatrix}, \tag{2-95}$$

$$G_{k-1} = \begin{bmatrix} 0 & 0 & 0 & 1 & 0 & 0 & 0 & 0 & 0 \\ 0 & 0 & 0 & 0 & 0 & 0 & 1 & 0 & 0 \\ 0 & 0 & 0 & 0 & 0 & 0 & 0 & 1 & 0 \\ 0 & 0 & 0 & 0 & 0 & 0 & 0 & 0 & 1 \end{bmatrix}^T. \tag{2-96}$$

Note that this simplified kinematic model is used to achieve the desired refresh rate of 500 Hz. Although $Q_k$ represents model uncertainty and thus, some levels of model uncertainty can be tolerated by the EKF, more complex dynamic models can be adopted if found necessary in the future. Next, measurement update equations of the EKF are derived.

***Measurement update equations:***

In this section, the measurements update equations for state 1 are derived. States 0 and 2 have a reduced version of the measurement update equations derived here. In state 1, the available measurements are the distance $x_s$ and the orientation $\theta_s$ from the sonar system, and eight measurements from four magnetic sensors $B_{xMAGi}, B_{yMAGi}$ $(i = 1,2,3,4)$ which are measured with respect to the coordinate frame of each magnetic sensor. At each measurement update, first the measured magnetic fields by each magnetic sensor expressed in the coordinate frame of the approaching vehicle, $B_{xi}$ and $B_{yi}$, are calculated as

$$\begin{cases} B_{xi} = B_{xAMRi}\cos\hat{\theta}_k^- + B_{yAMRi}\sin\hat{\theta}_k^- \\ B_{yi} = -B_{xAMRi}\sin\hat{\theta}_k^- + B_{yAMRi}\cos\hat{\theta}_k^- \end{cases} \qquad i = 1,2,3,4. \tag{2-97}$$

Second, the ratio between the magnetic fields in $Y$ and $X$ direction, $B_{RATi} = \left|B_{yi}/B_{xi}\right|$, is calculated for each sensor. Next, the two sensors that have lower values of $B_{RAT}$ are selected (named $m$ and $n$) and the corresponding values of $B_{xi}$ and $B_{yi}$ of those two sensors are assigned to the new variables $B_{xm}$, $B_{xn}$, $B_{ym}$ and $B_{yn}$ to be used in measurement update. This procedure is performed in order to use the simplified magnetic field equations (2-65) and (2-66). The measurement update equations are:

$$Z = h(X, n) \qquad n \sim (0, R), \tag{2-98}$$

$$Z = [x_s \quad \theta_s \quad 0 \quad 0 \quad y_{meas}]^T, \tag{2-99}$$

$$\begin{aligned} h(X, n) = [&x + n_x \quad \theta + n_\theta \quad \dots \\ &B_{xm} - \left(\frac{p}{x_m} + q\right) + \left(n_{xMAGm}\cos\theta + n_{yMAGm}\sin\theta\right) \quad \dots \\ &B_{xn} - \left(\frac{p}{x_n} + q\right) + \left(n_{xMAGn}\cos\theta + n_{yMAGn}\sin\theta\right) \quad y + n_y]^T, \end{aligned} \tag{2-100}$$

$$K_k = P_k^- H_k^T (H_k P_k^- H_k^T + R_k)^{-1}, \tag{2-101}$$

$$\hat{X}_k^+ = \hat{X}_k^- + K_k\left[Z_k - h_k\left(\hat{X}_k^-, 0\right)\right], \tag{2-102}$$

$$P_k^+ = (I - K_k H_k) P_k^-, \tag{2-103}$$

$$H_k = \left.\frac{\partial h}{\partial X}\right|_{\hat{X}_k^-}$$

$$= \left.\begin{bmatrix} 1 & 0 & 0 & 0 & 0 & 0 & 0 & 0 & 0 \\ 0 & 0 & 0 & 0 & 1 & 0 & 0 & 0 & 0 \\ \frac{\hat{p}_k}{(\hat{x}_m)^2} & 0 & 0 & 0 & B_{ym} + \frac{\hat{p}_k d_m \cos\theta}{(\hat{x}_m)^2} & 0 & 0 & -\frac{1}{\hat{x}_m} & -1 \\ \frac{\hat{p}_k}{(\hat{x}_n)^2} & 0 & 0 & 0 & B_{yn} + \frac{\hat{p}_k d_n \cos\theta}{(\hat{x}_n)^2} & 0 & 0 & -\frac{1}{\hat{x}_n} & -1 \\ 0 & 1 & 0 & 0 & 0 & 0 & 0 & 0 & 0 \end{bmatrix}\right|_{\hat{X}_k^-}, \tag{2-104}$$

$$R_k = diag([\sigma_{xs} \quad \sigma_{\theta s} \quad \sigma_B \quad \sigma_B \quad \sigma_{y-meas}], \tag{2-105}$$

where $x_i = x + d_i \cos\theta \quad \& \quad i = m, n$, $d_m$ and $d_n$ are the distances of magnetic sensors $m$ and $n$ from point $A$, and values in $R_k$ matrix represent the covariance of noise in measurements. $y_{meas}$ is an estimate of $y$ and is obtained from equations of magnetic field in two-dimension as

$$\begin{cases} B_x = \dfrac{\mu_0 m_0 da}{2\pi} \dfrac{b}{x_A (x_A^2 + b^2)^{\frac{1}{2}}} \\ B_y = \dfrac{\mu_0 m_0 da}{2\pi} \dfrac{by}{(x_A^2 + b^2)^{\frac{3}{2}}} \end{cases} \quad \Rightarrow \quad B_{RAT} = \frac{B_x}{B_y} = \frac{y x_A}{x_A^2 + b^2}. \tag{2-106}$$

For each one of the selected sensors, m and n, we have the following relations:

$$B_{RATi} = \frac{y_i (x + d_i \sin\theta)}{(x + d_i \sin\theta)^2 + b^2} \quad i = m, n, \tag{2-107}$$

where $y_i = y + d_i \cos\theta$.

Now using $\hat{x}_k^-$ and $\hat{\theta}_k^-$ after each time update and the above equations, we can get an estimate of $y_m$ and $y_n$ from the following linear equations:

$$\begin{cases} B_{RATm}T_m - y_m\left(\hat{x}_k^- + d_m \sin\hat{\theta}_k^-\right) = 0, \\ B_{RATn}T_n - y_n\left(\hat{x}_k^- + d_n \sin\hat{\theta}_k^-\right) = 0, \\ y_m - y_n = (d_m - d_n)\cos\hat{\theta}_k^-, \\ T_m - T_n = \left(\hat{x}_k^- + d_m \sin\hat{\theta}_k^-\right)^2 - \left(\hat{x}_k^- + d_n \sin\hat{\theta}_k^-\right)^2. \end{cases} \tag{2-108}$$

where

$$T_i = \left(\hat{x}_k^- + d_i \sin\hat{\theta}_k^-\right)^2 + b^2, \quad i = m, n. \tag{2-109}$$

Solving for $y_m$, $y_n$, $T_m$ and $T_n$ we can obtain an estimation of $y$ from the following equation:

$$y_{meas} = y_m - d_m \cos\hat{\theta}_k^-. \tag{2-110}$$

It should be noted that while calculating the Jacobian for EKF measurement update equations, the effect of uncertainties in $\hat{x}_k^-$ and $\hat{\theta}_k^-$ on $y_{meas}$ is ignored and $y_{meas}$ is assumed to have a zero mean Gaussian noise to make the Jacobian simpler.

### 2.3.4. Experimental Results

The developed estimator was tested with the Ford vehicle door (shown in Figure 2-19) and a Mazda Protégé 1999 sedan. Testing with the door has the advantage that more complicated scenarios can be implemented since it is easier to move it around.

#### 2.3.4.1. Results from the Tests with a Ford Door

The estimator was first verified with tests using the Ford vehicle door. The door is mounted on a wheeled platform, as shown in Figure 2-19, and can be maneuvered and moved easily towards or away from the sensors in different angles. Also, in these experiments, a few magnets were attached to the door so as to intensify its magnetic field and detect it magnetic signature from a longer distance.

Video 2-1 shows a video captured during one of the experiments. This video shows the motion of the door as recorded by a webcam and its position and orientation being estimated and displayed using MATLAB in real time. The red rectangles show the location of the magnetic sensors (sonar transducers are not shown). At the beginning of the experiment, the door is only detected by the sonar system and updates are performed using measurements from the sonar system (state 0) as indicated in the title of the plot ("Update with Sonar"). As the door gets closer, the magnetic sensors start responding and updates are performed using measurements from both the sonar system and the magnetic sensors (state 1) as indicated in the title of the plot ("Update with Sonar + AMR"). In this state, the two most appropriate magnetic sensors used for measurement update are shown by black rectangles. Next the door rotates towards $\theta \cong -35^{\circ}$ which is out of the detection range of the sonar system. Thus, updates are performed only using measurements from the magnetic sensors (state 2) as indicated in the title of the plot ("Update with AMR"). Next, the door moves closer to the sensors at the oblique angle of $\theta \cong -35^{\circ}$, moves back, and then rotates back towards $\theta \cong 0^{\circ}$ where updates are performed using measurements from both the sonar system and the magnetic sensors measurements (state 1). Finally, the door moves close to the sensors with $\theta \cong 0^{\circ}$ which makes the measurements from the sonar system unavailable due to the close range and updates are performed only using measurements from the magnetic sensors (state 2). Video 2-1 is also included in supplementary files.

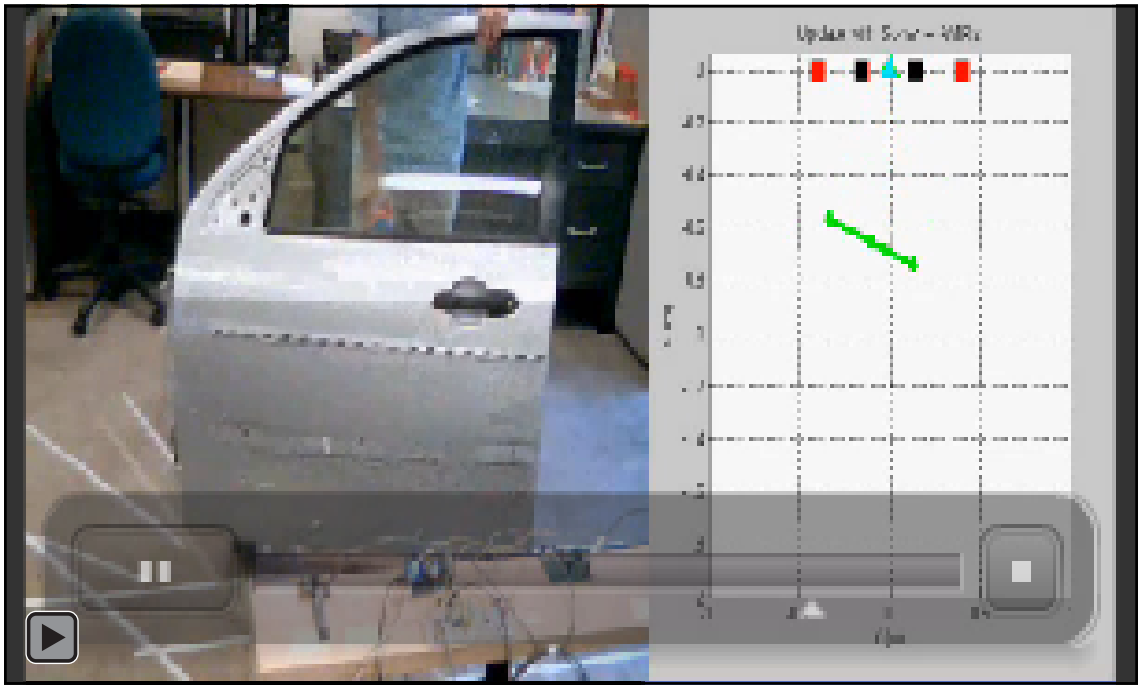

Video 2-1. A video of the experiment showing the motion of the door as recorded by a webcam and its position and orientation being estimated and displayed using MATLAB in real time. This video is also included in supplementary files.

Figure 2-35 shows snapshots of the estimated position of the door at different time intervals during the experiment. The color of the line used to represent the door position goes from black to gray from the beginning towards the end of the experiment. Points A, B, C, and D represent the initial position of the door, the point where the door starts to rotate towards $\theta \cong -35^{\circ}$ and later back to $\theta \cong 0^{\circ}$, the point where the doors gets close to the sensors at $\theta \cong -35^{\circ}$, and the point where the door gets close to the sensors at $\theta \cong 0^{\circ}$, respectively.

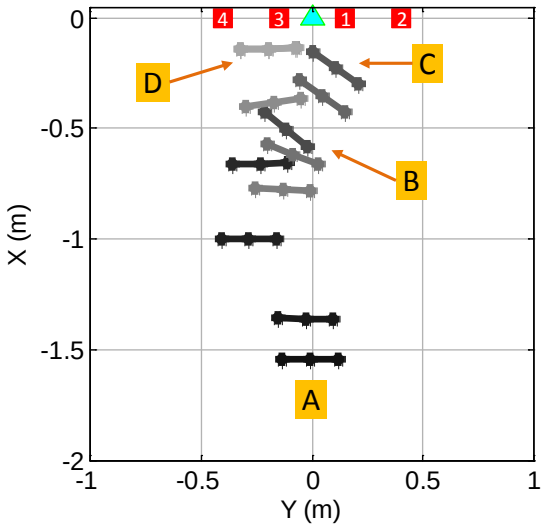


Figure 2-35. Snapshots of the estimated position of the door at different time intervals.

Figures 2-36 to 2-39 show some of the estimated states over time. It can be seen from Figures 2-36 and 2-38 that when the door rotates to more than a threshold angle at $t \cong 11$ s, the sonar measurements of distance and orientation become invalid and the estimator switches from state 1 to state 2, and updates only with magnetic sensors. When the door rotates back toward $\theta = 0$ at $t \cong 17$ s, the sonar measurements become valid again and the estimator switches to state 1. Also, when later in the experiment, at $t \cong 22$ s, the door gets very close to the sensors, the sonar measurements become invalid again and the estimator switches to state 2. In addition, we can see from Figure 2-37 that at the beginning of the experiment, since magnetic sensors are not available yet, updates are performed only with measurements from the sonar system (State 0) and thus, an estimate of $y$ is not available. However, as soon as magnetic sensors become available ($t \cong 5.5$ s), estimation of $y$ becomes possible as well.

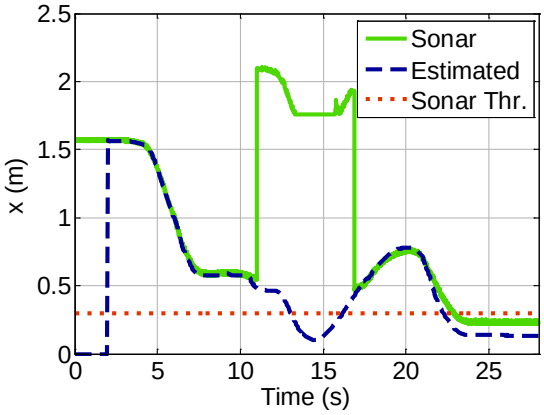


Figure 2-36. Estimated "$x$" over time.

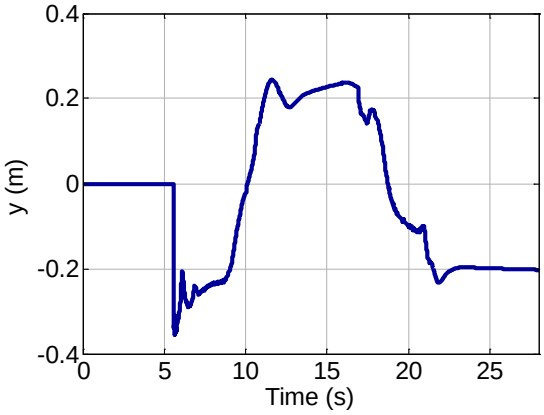


Figure 2-37. Estimated "$y$" over time.

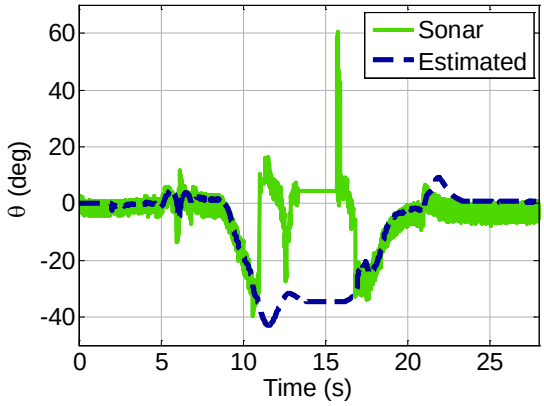


Figure 2-38. Estimated "$\theta$" over time.

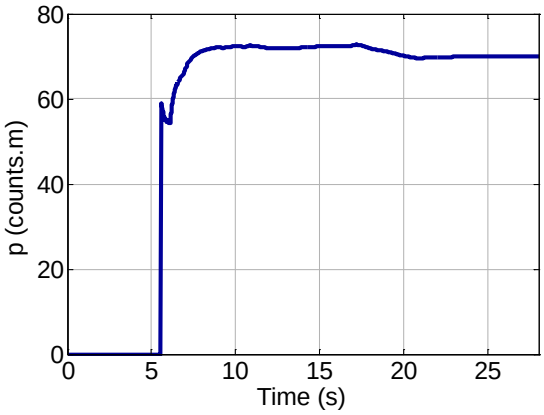


Figure 2-39. Estimated "$p$" over time.

Figure 2-40 shows how the Mahalanobis distance is used to reject sonar outliers. As $d_{mah-k}$ goes over the predefined threshold, the sonar measurement is ignored. The measurements from the 4 magnetic sensors are shown in Figures 2-41 and 2-42.

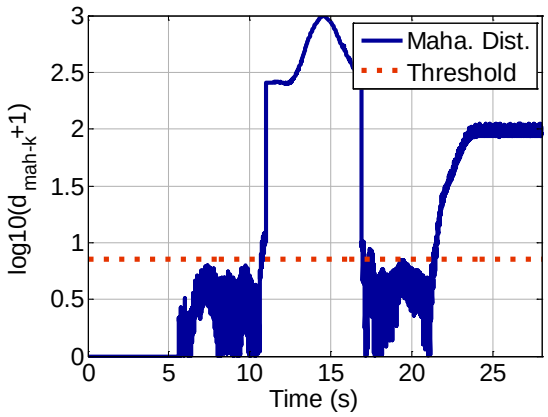


Figure 2-40. Mahalanobis distance used to reject sonar outliers.

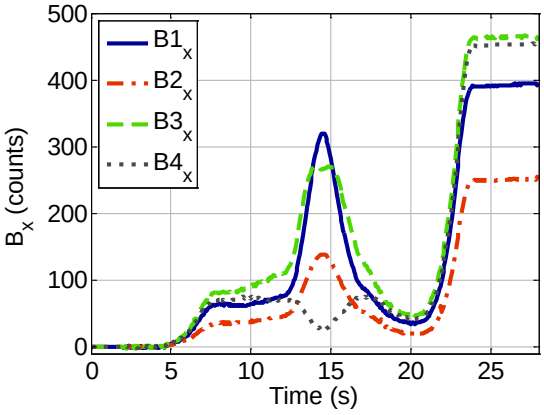


Figure 2-41. Magnetic field along the $X$-axis of the sensors.

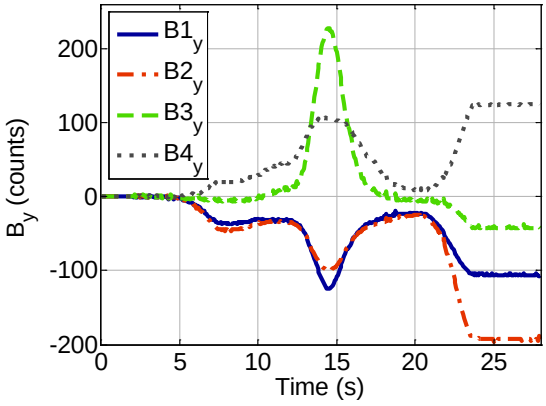


Figure 2-42. Magnetic field along the $Y$-axis of the sensors.

### 2.3.4.2. Results from the Tests with a Mazda Protégé

Tests were conducted with a full scale passenger sedan (Mazda Protégé) so as to evaluate the performance of the developed system at various orientation angles. In these tests, the Mazda car was driven toward the sensors at a fixed angle. Data was obtained at various fixed angles to verify performance for different orientations. Figures 2-43 to 2-47 show the result from one of the tests where the car moved at an orientation of about $\theta = -20^{\circ}$ towards the sensors and then back away from the sensors. In these figures the magenta triangles indicate the time interval that a vehicle is detected and active

positioning is performed. The orange circles indicate the time interval that the magnetic sensors are responding and the estimator is in state 1 or 2 depending on the availability of sonar measurements. Also in this test, $x_{th}$ for the sonar system has been set to 1 meter and thus, the estimator switches from state 1 to 2 when $x < x_{sonar-th} = 1$ m, However, the sonar measurements are valid up to about 0.25 m from the transducers. With this higher threshold we can evaluate the estimator performance by comparing sonar system and estimator values. The error between magnetic sensors estimation (state 2) and sonar measurement is shown in Figure 2-48.

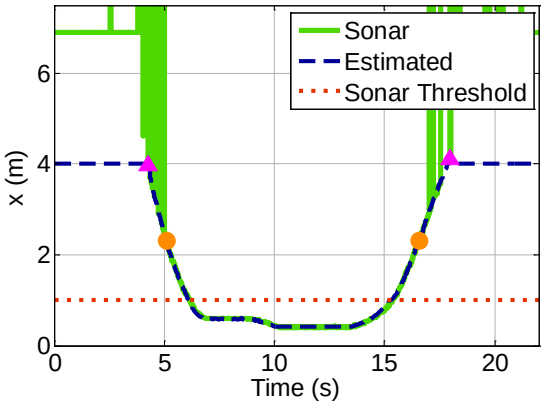


Figure 2-43. Estimated "$x$" over time.

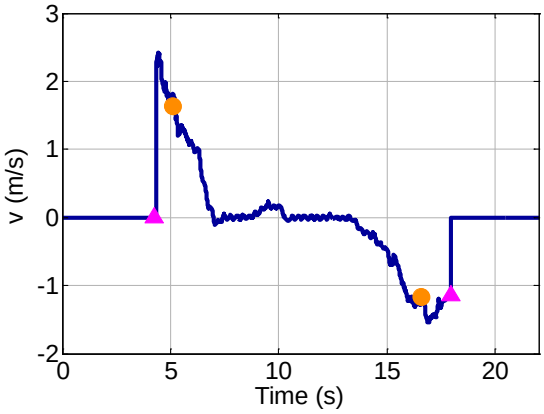


Figure 2-44. Estimated "$v$" over time.

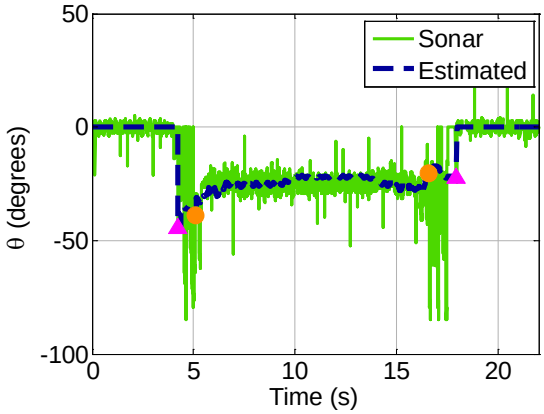


Figure 2-45. Estimated "$\theta$" over time.

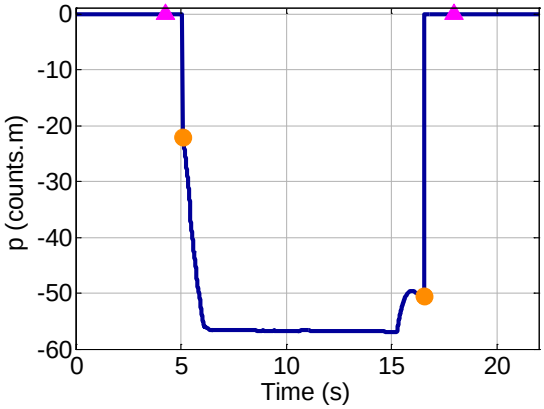


Figure 2-46. Estimated "$p$" over time.

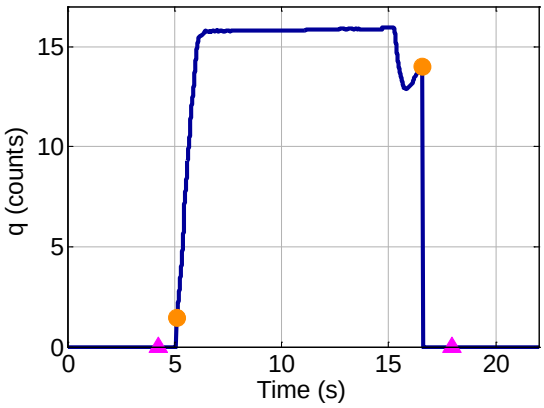


Figure 2-47. Estimated "$q$" over time.

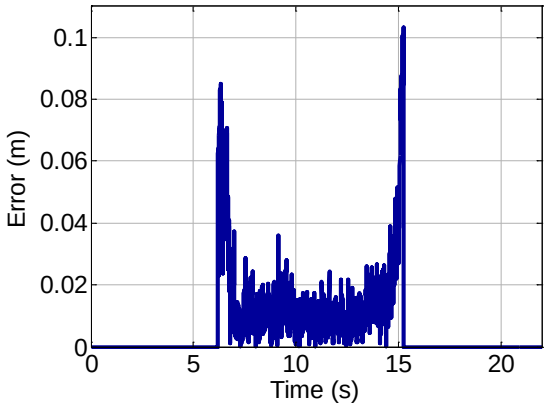


Figure 2-48. Error in "$x$" estimation over time.

It should be noted that the tests in this section were carried out using a single vehicle. Additional vehicles could be parked close to the test vehicle if multipath and robustness issues need to be evaluated.

## 2.4. Technical Challenges and Future Work

In this section, we will discuss possible future research to improve the performance and verify the reliability of the proposed crash detection system. In summary, the major topics include expansion of the magnetic field model to include $Z$-axis magnetic field measurements, performing experiments with a larger number of vehicles to verify the magnetic field model, analysis of the estimator convergence rate at high relative velocities, improvement of the implementation of the EKF to achieve a higher update rate, and development of a test rig to perform tests at high relative velocities. These topics are briefly discussed in the following sections.

### 2.4.1. Effect of External Magnetic Field Sources on the Sensors

External changing (dynamic) sources of magnetic field can influence the measurements of the magnetic sensors and as a result, affect the accuracy of the estimates. An example is the magnetic fields induced by the electrical systems in a car equipped with the proposed sensing system. A quick calculation using the formula $B = \frac{\mu_0 I}{2\pi d}$ for the magnetic field from a long wire at a distance $d$ shows that a changing current of $0.1$ A can cause a change of magnetic field by $2$ mG at a distance of $10$ cm from the wire. Since the magnetic field from an approaching car is over $50$ mG even at a distance of $2$ m, the error due to electrical systems on a car is likely to be small. However, the electric currents can be much larger in electric vehicles and thus it will be important to place the sensors far enough from major sources of alternating electric currents in such cases. Note that as long as the currents are constant, like when an electric vehicle is cruising at a constant velocity, they will not have an impact on the performance of the sensing system. On the other hand, when an electric vehicle is accelerating or decelerating, alternating currents will be generated.

To better understand possible issues, several tests were performed with a Chevrolet Volt vehicle. In all of the tests, the vehicle was operated only on the battery. The scenario for the tests was as follows: The car was driven from zero velocity to a maximum velocity and then stopped over a course of $40$ m. With this scenario, it is possible to study the effects of alternating currents due to the acceleration and deceleration of the vehicle. The results from three different cases are shown in Figure 2-49. In the first case, a magnetic sensor was placed over the mat of the front passenger side as close as possible to the engine. The maximum velocity reached was $\sim 1.3$ m/s ($\sim 3$ mph) which was read from the speed gauge. In the second case, the magnetic sensor was at the same location as the first case but the maximum velocity reached was $\sim 8$ m/s ($\sim 18$ mph). The larger

maximum velocity in this case would result in larger acceleration and deceleration compared with the first case. Finally, in the third case, the sensor was placed closer to the front passenger door which is a typical and candidate location for the magnetic sensors. Similar to the second case, the maximum velocity reached was ~7.6 m/s (~17 mph).

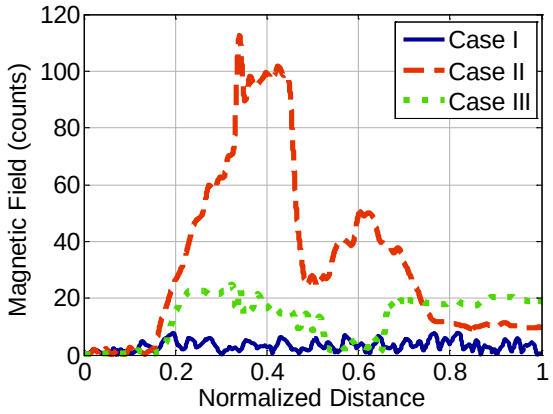


Figure 2-49. Results from the experiment with Chevrolet Volt.

Figure 2-49 shows that if the sensors are placed in a proper location, the influence of the alternating currents can be minimized. This issue can be tackled through another approach as well. Magnetic field has typically a linear relationship with current passing through a wire. Thus, it would be possible to use current sensors measurements on the high current wires and magnetic sensors measurements to pre-calculate the influence of the currents at the location of each magnetic sensor. During the normal operation of the sensing system, the influences can be subtracted from the magnetic sensors readings based on the measured currents.

Later in Chapter 3, we use the same principle of position estimation developed in this chapter to estimate piston position in cylinders in a number of different applications. In Section 3.5, a method is developed to reject the magnetic disturbances on the position estimation system created by external sources which is based on sensor fusion of multiple closely spaced magnetic sensors. That method can be further improved and be adopted in the crash detection system developed in this chapter as well.

So far, we have considered the challenges associated with an electric vehicle equipped with our sensing system. The next question is that if there are challenges in estimating the relative position of an electric vehicle approaching another vehicle equipped with the sensing system. In other words, the question is that if the alternating currents generated by acceleration and deceleration of an electric vehicle or its motors cause deviations from the derived analytical model of magnetic field vs. position. To answer this question, the following experiment was conducted with the Chevrolet Volt electric vehicle. A three-axis magnetic sensor and a sonar sensor were placed in front of the vehicle similar to the scenario shown in Figure 2-3. The vehicle was placed stationary at a very close distance to the sensors. In the first case, it was driven backward and slowly away from the sensor. In the second case, it was driven backward and faster away from the sensor. Thus, if the currents or the motors of the electric vehicle are to affect the magnetic field model, we should see a larger deviation in the second case.

The first observation of this experiment was that the Chevrolet Volt vehicle did not create a large signal along the $X$-axis of the magnetic sensor. Therefore, the $Z$-axis (perpendicular to the ground) signal was used to compare the two cases. The average acceleration was $\sim 0.05\ \mathrm{m/s^2}$ and $\sim 3.42\ \mathrm{m/s^2}$ for the first and second cases, respectively. The average acceleration was measured from the sonar sensor. Figure 2-50 shows the results of the experiment and it can be seen that both cases create an almost identical magnetic field although the second case has a much higher acceleration. Therefore, the changing magnetic field created in an electrical vehicle during acceleration/deceleration seem not to influence the sensors on another vehicle.

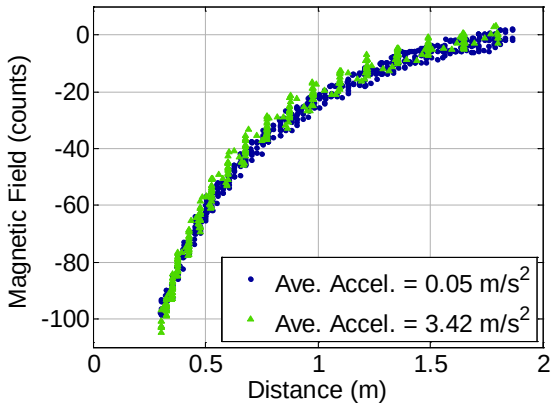


Figure 2-50. Results from experiments with Chevrolet Volt at two different accelerations.

## 2.4.2. Expanding Magnetic Field Models

Remember from Section 2.3 that the developed position sensor system takes advantage of the measurements in the $XY$ plane around a vehicle (parallel to the ground) as shown in Figure 2-51. An analytical expression for the magnetic field in the $XY$ plane was derived by modeling a vehicle as a block of magnetic dipoles orientated along the $X$-axis (longitudinal axis of a vehicle) as shown in Figure 2-28. An adaptive estimator was developed later in Section 2.3 to estimate an approaching vehicle's position and orientation in real time.

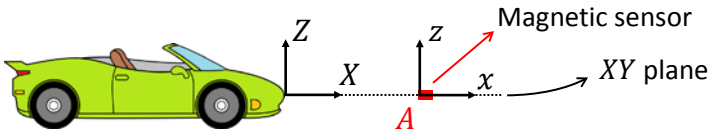


Figure 2-51. Earlier in this chapter, mathematical expressions were developed to model the magnetic field due to a vehicle in the $XY$ plane.

As mentioned in Section 2.4.1, it was observed that the Chevrolet Volt vehicle did not create a large enough signal along the $X$-axis of the magnetic sensor. However, it created a large enough signal along the $Z$-axis of the sensor. On the other hand, some of the vehicles in the earlier tests also created noticeable signals along the $Z$-axis. Thus, it is

reasonable that as a future work, the developed models be expanded to include measurements along the $Z$-axis, and the new models and associated measurements be incorporated into the estimator.

As an example, considering the 1-D motion, a model for the magnetic field in $Z$ direction along the longitudinal axis of motion of a vehicle, $X$-axis, is derived and verified in this section. Similar to (2-11), it is desired to find an analytical relation between $B_z$ and $x_A$ shown in Figure 2-51. Assuming that the sensors are roughly at the same level as the chassis, a vehicle should have magnetic dipoles with nonzero components along the $Z$-axis for $B_z$ to be nonzero. In other words, the contribution of magnetic dipoles in $XY$ plane (green dipoles in Figure 2-52) to $B_z$ is zero. Similarly, the contribution of magnetic dipoles along the $Z$-axis (blue dipoles in Figure 2-52) to $B_x$ is zero.

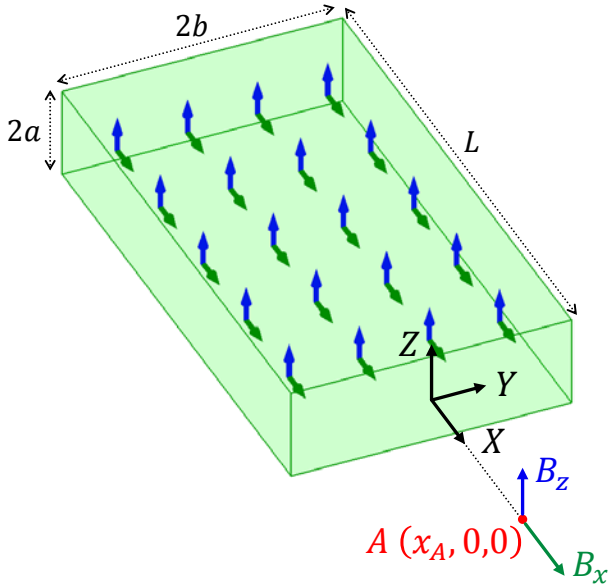


Figure 2-52. Modeling the magnetic field of a rectangular block of magnetic dipoles along both $X$-axis and $Z$-axis.

Note that the vehicle is still modeled as a uniform block of magnets, but the magnetic dipoles are allowed to have components along both $X$-axis and $Z$-axis. Thus, for

a vehicle that creates a low magnetic field along its $X$-axis but a large magnetic field along $Z$-axis, such as the Chevrolet Volt, the magnetic dipoles have a larger component along $Z$-axis compared with the $X$-axis.

With the assumptions made in Section 2.3.1 that i) $a$ is small relative to $b$, ii) $x_A + L \gg x_A$, and iii) $x_A$ is small relative to $b$, we can derive a mathematical relation between $B_z$ and $x_A$ as

$$B_z = \frac{\mu_0 m_{z0} a}{2\pi} \int_{-L}^{0} \int_{-b}^{b} -\frac{1}{((x_A - x)^2 + y^2)^{\frac{3}{2}}} dy dx$$

$$= -\frac{\mu_0 m_{z0} a}{\pi} \left( \frac{(x_A^2 + b^2)^{\frac{1}{2}}}{b x_A} - \frac{((x_A + L)^2 + b^2)^{\frac{1}{2}}}{b(x_A + L)} \right) \tag{2-111}$$

$$\cong -\frac{\mu_0 m_{z0} a}{\pi b} \left( \left( 1 + \left( \frac{b}{x_A} \right)^2 \right)^{\frac{1}{2}} - 1 \right) \cong -\frac{\mu_0 m_{z0} a}{\pi x_A} = \frac{p_z}{x_A},$$

where the definition of $p_z$ is apparent. If there is any existing magnetic field at point $A$, like the Earth's magnetic field, a constant needs to be added to equation (2-111) to obtain the total magnetic field, resulting in:

$$B_z = \frac{p_z}{x_A} + q_z \tag{2-112}$$

Interestingly, the derived relation for $B_z$ is similar to the relation obtained earlier for $B_x$. Figures 2-53 and 2-54 show the result of applying this relation to the data obtained from tests with Chevrolet Volt and Hyundai Elantra vehicles. Similar results were obtained from tests with Chevrolet Impala and Honda Accord vehicles. However, the Volkswagen Passat vehicle did not create a noticeable signal along the $Z$-axis of the magnetic sensor although it had the largest signal along the $X$-axis among the test vehicles.

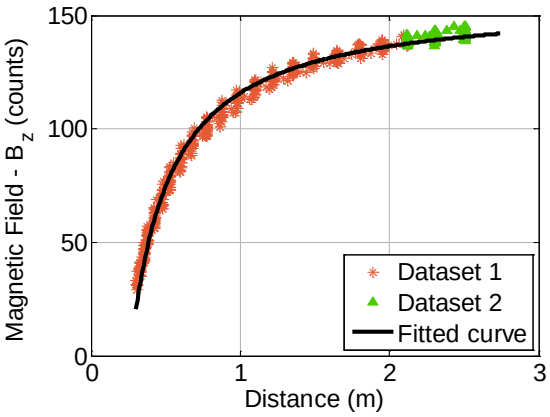


Figure 2-53. Results of the experiment with Chevrolet Volt and fitted curve.

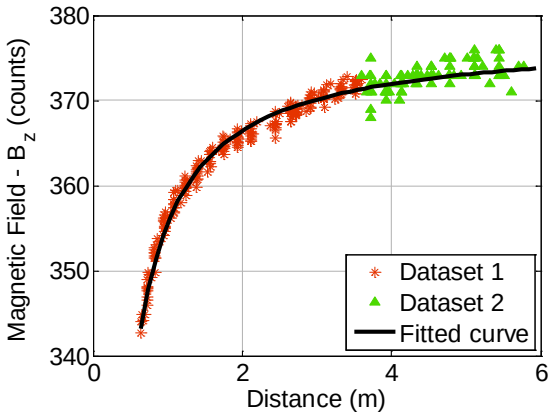


Figure 2-54. Results of the experiment with Hyundai Elantra and fitted curve.

In conclusion, a future research work is to expand the magnetic field models, perform tests with a larger number of vehicles to verify the models, and finally incorporate the new developed models into the developed sensor system. Note that due to the adaptive nature of the estimation system, some level of possible inconsistencies in the derived models can be tolerated by the system.

### 2.4.3. Improving the Platform of the Sensor System

As discussed in Section 2.3.3, the EKF developed in this chapter has been implemented using MATLAB. The magnetic sensors and the sonar system measurements are collected by dsPIC Microchip microcontrollers and transmitted to the PC to be used by the EKF in measurement update. This system achieves an update rate of 500 Hz and was selected for proof of concept due to the simplicity of implementation and debugging, and to provide a visual feedback in real time. There are possible ways to considerably increase the update rate of the developed system. As an example, data collection and estimation can be performed on a single processor to eliminate the time required to transmit the data from microcontrollers to PC. Also, the EKF equations can be optimized

for faster calculations and/or reduced-order filters be used ([53, 57]) if the estimation accuracy is not sacrificed.

### 2.4.4. Convergence Analysis Using Monte Carlo Simulations

The estimator developed in this chapter was able to achieve a reasonable convergence rate by the brief use of sonar sensor measurements. Due to physical limitations, the tests conducted to verify the performance of the estimator were at low relative velocities. A future work is to adopt the Monte Carlo method to simulate cases with larger relative velocities in order to investigate the convergence rate and possibly improve the performance of the estimator. Note that convergence is not only a function of time, but also depends on how "informative" the measurements are at each EKF measurement update. As a vehicle moves faster towards the sensors, measurements with larger signal-to-noise ratio will be provided to the estimator due to the $1/x$ relation between the magnetic field and distance.

A brief example of such simulations is presented in the following paragraphs considering the 1-D estimator developed in Section 2.2.4. The assumption made for this example are: i) the update rate of the estimator is $2$ KHz (refer to Section 2.4.3 for possible approaches to increase update rate of the existing system) and ii) the sample rate of the sonar sensor is $25$ ms which means that the sonar sensor can detect objects up to about $4$ m. Next, for a range of impact velocities of $2.5\ \mathrm{m/s} - 25\ \mathrm{m/s}$, system model and measurements are simulated as

$$X_k = FX_{k-1} + Gw_{k-1} \qquad w_k \sim (0, Q_k), \tag{2-113}$$

$$Z_k = h(X_k, n_k) \qquad n_k \sim (0, R_k), \tag{2-114}$$

where $F$, $G$, and $h$ are defined by (2-31), (2-32), and (2-35), respectively. The estimated state, $\hat{X}_k$, can be obtained by applying the estimator designed in Section 2.2.4 to simulated measurements, $Z_k$. The error between $X_k$ and $\hat{X}_k$ indicates the estimator error for each run. As an example, the error in position and velocity estimates at $x_k = 0.4$ m over 1000 runs are calculated and then averaged for each candidate impact velocity. The results are shown in Figures 2-55 and 2-56.

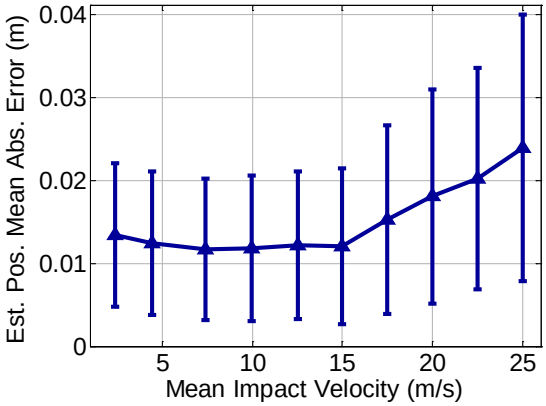


Figure 2-55. Mean absolute error of position estimate at $x_k = 0.4$ m.

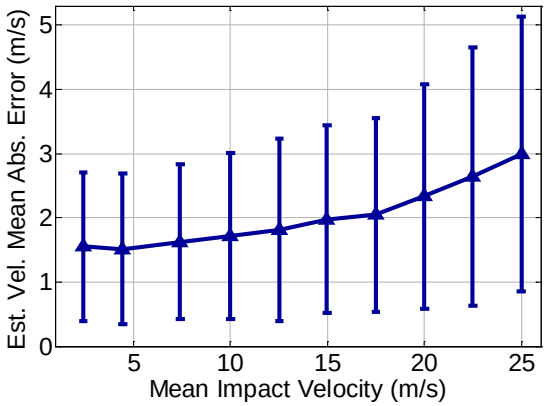


Figure 2-56. Mean absolute error of velocity estimate at $x_k = 0.4$ m.

The results indicate that the error in position and velocity estimates slightly increase by the increase of the impact velocity, nevertheless, the mean absolute position error stays around a couple of centimeters.

Note that in this example, the values of $p$ and $q$ were fixed for each run and were adopted from Table 2-1. Similar experiments can be performed to include variable model parameters. Overall, the goal of such experiments is to understand the design limitations and tune filter parameters so as to guarantee a reasonable performance across different conditions.

### 2.4.5. Development of a Platform for High Relative Velocity Tests

Finally, in order to verify the performance of the estimator in a real crash scenario, a test rig should be developed to enable high relative velocity tests. Another possibility is to use crash test facilities where high speed tests are performed and equip the colliding objects with the developed sensing system. In either case, these tests would require considerable effort and financial support since it is almost impossible to recover and reuse the sensors after each real crash test. These types of tests were beyond the scope of this thesis which is to show the feasibility of the concept of using the inherent magnetic field of objects for position estimation.

## 2.5. Conclusion

In this chapter, a novel and unique automotive sensing system was developed for the estimation of relative position and orientation of another vehicle in close proximity. The developed system can be used to predict and classify an imminent crash. The sensing system is based on the use of anisotropic magnetoresistive (AMR) sensors which measure magnetic field. While AMR sensors have previously been used to measure traffic flow rate and to detect vehicles in parking spots, they are used here for the first time to measure the relative two-dimensional position of the vehicle.

Analytical formulations were developed to predict the relationships between position and magnetic field for 1-D and 2-D relative motion. The use of these relationships to estimate vehicle position is complicated by the fact that the parameters in the relationships vary with the type of vehicle under consideration. Since the type of vehicle encountered is not known a priori, the parameters for the magnetic field vs. position relationship have to be adaptively estimated in real time.

A system based on the use of multiple magnetic sensors and a custom-designed sonar system together with an extended Kalman filter was developed to estimate vehicle parameters, position, and orientation in a 2-D plane. The use of the combined sensors results in a reliable system that performs well without the knowledge of vehicle specific magnetic field parameters. Test results with a wheeled laboratory test rig consisting of a door and tests with a full scale passenger sedan were presented. The experimental results confirm that the developed sensing system is viable and that it is feasible to adaptively estimate vehicle position and orientation even without prior knowledge of vehicle-dependent parameters.

# 3. Non-intrusive Piston Position Estimation Using Magnetic Field Measurements

## 3.1. Introduction

In Chapter 2, it was shown that the inherent magnetic field of a vehicle can be used to estimate its position and velocity relative to another vehicle to predict an imminent unavoidable crash so as to use the information to mitigate the effect of the crash on the occupants. The main concept behind the developed system is that any ferromagnetic object has an inherent magnetic field which varies as a function of position around the object. By modeling the magnetic field as a function of position and using sensors to measure magnetic field, the position of the object can be estimated. This same concept can be applied to position estimation of ferromagnetic objects in many other applications as well. In this chapter, it is shown that the proposed concept can be used for non-intrusive real-time estimation of piston position in engines, pneumatic cylinders, hydraulic cylinders, and many other machines. The major superiority of the proposed technology over the existing technologies is its lower cost and noncontact operation.

Any ferromagnetic object has an inherent magnetic field which varies as a function of the position around the object. If the magnetic field is analytically modeled as a function of position and the field intensity is measured using magnetic sensors, then the

position of the object can be estimated using the model and the measurements. A significant challenge for this proposed sensing mechanism arises from the fact that the parameters in the magnetic field vs. position function are unique to the particular object under consideration. While the functional form will remain the same for objects of the same shape and size, the parameters in the function can vary from one object to another due to varying level of magnetization. Therefore, calibration for each individual object is needed to obtain model parameters which could be extremely time consuming both for instrumentation of the system with reference calibration sensors and for the actual data gathering and calibration process. In Chapter 2, this challenge was overcome by developing adaptive estimation algorithms to estimate both model parameters and vehicle position in real time as a vehicle approaches the sensors. In the developed sensor system, sensor fusion with a custom-designed sonar system was used to improve the convergence rate which is required for immediate crash detection. In this chapter, adaptive estimation algorithms are developed using only magnetic field measurements and specific to piston position estimation applications.

Piston position measurement is required for many applications in a number of industrial domains. For example, in modern internal combustion engines with variable compression ratio, measuring the position of a piston inside the engine cylinder is important for real-time combustion control technologies [58, 59]. Another application is measurement of piston position in hydraulic cylinders of an excavator for automatic excavation [27, 60, 61] (Figure 3-1.a). In precision agriculture, seeding depth is an important factor for maximum seed germination and reduced energy consumption [62-65]. For example, planting seeds too shallow increases the risk of drying up before germination. Planting seeds too deep may delay germination and exhaust seedlings. Also, more fuel is consumed with the increase of seeding depth since friction forces are higher. Hydraulic cylinders are one of the tools to adjust the seeding depth in planters (Figure 3-1.b) and thus, piston position measurement is required to achieve optimal seeding depth and reduce energy consumption. Piston position estimation is also required

for many applications involving pneumatic actuators. An example is web handling where pneumatic actuators are used to control the position of guide rollers required for active control of tension in a web [66-69] (Figure 3-1.c).


Figure 3-1. Potential applications of piston position estimation in (a) hydraulic cylinders of an excavator for automatic excavation, (b) hydraulic cylinders of a planter for maintaining optimal seeding depth, and (c) a pneumatic actuator for web guide. Photos are courtesy CNH® and Bimba®.

This chapter is organized as follows: In Section 3.2, a method is developed for estimation of piston position in a free piston engine based on the proposed sensing concept. In Section 3.3, it is shown through a case study that if the piston lacks inherent magnetic field, a small magnet can be attached to it and exactly the same developed method be applied for piston position estimation. A pneumatic cylinder is used for the experiments in that section. A summary of the proposed sensing method is presented in Section 3.4 so that it can be followed for other piston position estimation applications. A challenge in the use of magnetic sensors for piston position estimation is the magnetic disturbance caused by other magnetic objects coming close to the sensors which can create significant position estimation errors. This problem is discussed in Section 3.5 and a method is developed to make the sensing system robust to the external disturbances. In Section 3.6, a comparison between the developed sensing technology and other existing sensors is provided. This chapter is concluded in Section 3.7.

## 3.2. Piston Position Measurement in a Free Piston Engine

In modern internal combustion engines with variable compression ratio, measuring the position of a piston inside the engine cylinder is becoming important for a variety of real-time combustion control technologies. In this section, we show how the proposed measurement system can be used for accurate estimation of piston position inside a free piston engine (FPE).

A free piston engine is one that does not have a crankshaft attached as in conventional engines. This “frees” the piston motion from being restricted by the position of the rotating crankshaft. The position of the piston instead is determined by the interaction between the combustion gas forces and the load forces acting on it. Advantages of a free piston engine include reductions in friction losses and possibilities to optimize engine operation efficiency using variable compression ratios. A FPE can have variable stroke length and the piston position needs to be controlled actively [58]. This requires a precise position sensor for real-time feedback.

Figure 3-2 shows a schematic of a dual piston FPE used in this section. The FPE includes an inner and an outer piston that can move towards and away from each other. Accurate estimation of the positions of the pistons is needed for synchronizing and controlling their motion. Currently, linear variable differential transformer (LVDT) is used for piston position measurement. The LVDT is expensive and furthermore requires significant effort for assembly into the engine. Also, it requires mechanical connection to the piston which makes its life cycle limited due to the harsh environment inside the engine cylinder. In this work, the LVDT is used only to verify the accuracy of the piston position estimates obtained from the magnetic sensors.

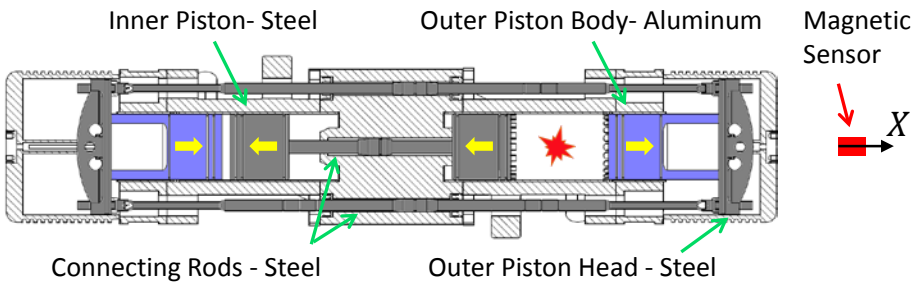


Figure 3-2. Free piston engine diagram.

The goal is to estimate the position of the outer piston by placing a magnetic sensor on one side of the FPE as shown in Figure 3-2. The same printed circuit board (PCB) shown in Figure 2-4 with the HMC2003 three-axis magnetic sensor boards from Honeywell are used for data collection. However, very small changes in the magnetic field were observed as the piston was moved during preliminary tests. The change was of the order of 0.2 G during full motion of the outer piston, from 20 mm to 60 mm away the AMR sensor. To get a better signal-to-noise-ratio, the signal from AMR sensors were amplified. The HMC2003 sensors have a nominal sensitivity of $1\,\mathrm{V/G}$ and since the sensor signals are being captured with a 12-bit analog-to-digital converter with a voltage range of $0-5\,\mathrm{V}$, one count is equivalent to $(5/4095)\,\mathrm{V} = 1.22\,\mathrm{mV} \cong 1.22\,\mathrm{mG}$. On the other hand, the specified resolution of the AMR sensor according to the manufacturer is 40 μG. Therefore, it is appropriate to amplify the output of the sensor by about 5 times to get higher signal levels without a significant deterioration in the signal-to-noise ratio. The Analog Devices AMP04 amplifier chip was utilized for amplification.

The main source of the generated magnetic field is considered to be the outer piston connecting mechanism, made of steel, since the body and the rest of the outer piston is made of aluminum. Also the inner piston is far away from the outer piston connecting rod ($\sim$170 mm at the closest distance) and its effect on the magnet field at the location of the magnetic sensor is considered to be negligible.

In the next section, an analytical relation between the magnetic field created by the piston connecting mechanism and the distance from it will be derived.

### 3.2.1. Analytical Derivation of Magnetic Field Equations

The outer piston connecting mechanism has a complex shape, shown in Figure 3-3 and it is difficult to obtain an exact analytical formula for its magnetic field. However, if the shape is approximated with a rectangular cube as shown in Figure 3-4, an approximate analytical equation for the magnetic field as a function of position along the longitudinal $X$-axis can be obtained.

Figure 3-3. Outer piston connecting mechanism.

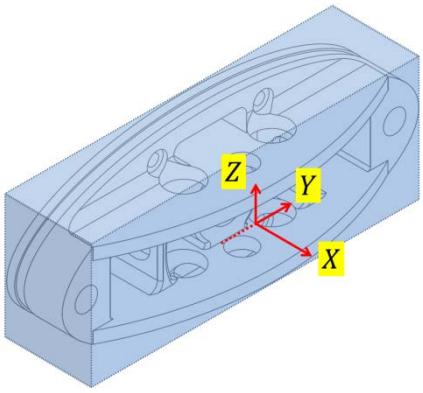


Figure 3-4. Outer piston connecting mechanism enclosed in a rectangular block.

Considering Figure 3-4, our objective is to derive a relation expressing the magnetic field along the $X$-axis of the piston head (connecting mechanism) as a function of distance from it.

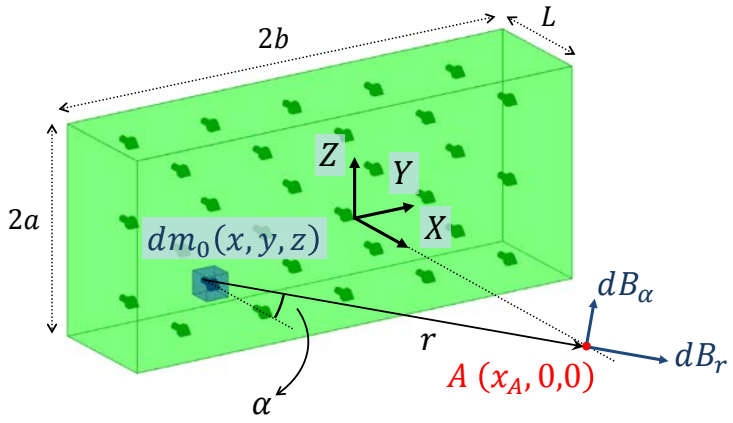


Figure 3-5. Block of magnetic dipoles.

Recall from Section 2.2.1 that the magnetic field along the $X$-axis of a rectangular cube is expressed by the integral in (2-8) which has the following solution:

$$B_x = \frac{\mu_0 m_0}{\pi}\left(\operatorname{atan}\left(\frac{ab}{x_A(a^2+b^2+x_A^2)^{1/2}}\right) - \operatorname{atan}\left(\frac{ab}{(x_A+L)(a^2+b^2+(x_A+L)^2)^{1/2}}\right)\right). \tag{3-1}$$

The above equation needs to be simplified in order to use it efficiently for position estimation. The dimensions of the head are

$$a \cong 35 \text{ mm}, \quad b \cong 80 \text{ mm}, \quad L \cong 40 \text{ mm}$$

The values of $x_A$ change from about 20 mm to 60 mm from the magnetic sensor. First of all, we can ignore the second term in comparison with the first term since we have $(x_A + L)$ in the denominator. We also have the connecting rods which add to the effective length $L$ and decrease the effect of the second term. Therefore, we get:

$$B_x \cong \frac{\mu_0 m_0}{\pi}\operatorname{atan}\left(\frac{ab}{x_A(a^2+b^2+x_A^2)^{1/2}}\right). \tag{3-2}$$

Also, we use the following approximation since $b$ is considerably larger than $a$ and $x_A$.

$$\frac{ab}{x_A(a^2+b^2+x_A^2)^{1/2}} = \frac{a}{x_A\left((\frac{a}{b})^2+1+(\frac{x_A}{b})^2\right)^{1/2}} \cong \frac{a}{x_A}. \tag{3-3}$$

Thus, we have:

$$B_x \cong \frac{\mu_0 m_0}{\pi}\text{atan}\left(\frac{a}{x_A}\right). \tag{3-4}$$

Finally, we can use the following approximation for the "atan" function [70]:

$$\theta = \text{atan}(z) \implies \theta = \frac{\pi}{4} - \frac{\pi}{4}\frac{1-z}{1+z}, \tag{3-5}$$

$$B_x \cong \frac{\mu_0 m_0}{\pi}\left(\frac{\pi}{4} - \frac{\pi}{4}\frac{1-\frac{a}{x_A}}{1+\frac{a}{x_A}}\right) = \frac{\mu_0 m_0}{4}\left(1-\frac{x_A-a}{x_A+a}\right) = \frac{\mu_0 m_0 a}{2}\,\frac{1}{x_A+a}. \tag{3-6}$$

To apply (3-6) to the piston head, we replace $a$ with $e$ since the effective height of the head is less than $a$ defined as the height of the rectangle enclosing the head. Defining $p = \frac{\mu_0 m_0 a}{2}$, we get the following model:

$$B_x \cong \frac{p}{x_A+e}. \tag{3-7}$$

We have obtained a simple relation for magnetic field at a distance $x_A$ from the piston head. By placing magnetic sensors at a distance from the piston head and using this relation, we can estimate the outer piston position $x_p$ from the magnetic field measurements. However, since we are subtracting the static magnetic field at the beginning of each test, which also includes the field created by the outer piston at its initial position, we need to rewrite (3-7) as

$$B_x = \frac{p}{x_p + e} - \frac{p}{x_{p0} + e}. \tag{3-8}$$

Subtracting the initial magnetic field is needed in order to remove the influence of the Earth's magnetic field and other static or slowly varying magnetic fields. In order to use (3-8) for position estimation, we need to know the three parameters $p$, $e$, and $x_{p0}$. However it is not possible to estimate these three parameters from this equation, even if we use two magnetic sensors instead of one magnetic sensor since the system becomes unobservable for the three unknown parameters. Therefore, we will assume that $x_{p0}$ is known. In the experiment presented here, we obtain $x_{p0}$ from the LVDT. In case that there are no LVDTs installed, we can start the piston from a known initial position (at the lower or upper bounds of motion of the piston) for the first time and obtain $x_{p0}$ from the geometry of the piston and the location of the magnetic sensor with respect to the engine. After the first run we record the final position to use it as the initial position for the next run.

In the following sections, five different methods are presented for estimation of model parameters. The first two methods take advantage from the installed LVDT to identify model parameters and are presented in Section 3.2.2. The parameters are identified by fitting curves to magnetic vs. LVDT measurements obtained from moving the piston a full stroke (from one end to the other end) and minimizing 2-norm (Method 1) and infinity-norm (Method 2) of the error. Methods 3 to 5 do not use the measurements from the LVDT; the parameters are estimated entirely using the signals from two longitudinally spaced magnetic sensors. Method 3 uses iterated nonlinear least squares to identify the model parameters from magnetic sensors measurements obtained from moving the piston a full stroke. Method 3 is described in Section 3.2.3. Method 4 is based on the extended Kalman filter (EKF) and estimates the parameters as well as position adaptively over time with the regular motion of the piston and thus, not requiring end-to-end motion. Method 5 is similar to method 4; however, the knowledge of the

stroke length is used to achieve faster convergence of parameters. Methods 4 and 5 are described in Section 3.2.4.

### 3.2.2. Parameter Identification for Position Estimation System Using the Additional LVDT (Methods 1 and 2)

Since the FPE in this case is already equipped with an LVDT, we can use the distance obtained from the LVDT and the magnetic field measurements from a magnetic sensor to obtain estimates of the model parameters. Therefore, the outer piston is moved a full stroke (from one end to the other end) and the magnetic sensor and LVDT signals are captured. Figure 3-6 shows the magnetic field obtained from the magnetic sensor vs. distance obtained from the LVDT as the piston is moved from $x_{p0} \cong 63$ mm to $x_{pf} \cong 23$ mm. Magnetic field is plotted in arbitrary voltage units, the same as what was read from the ADC of the microcontroller.

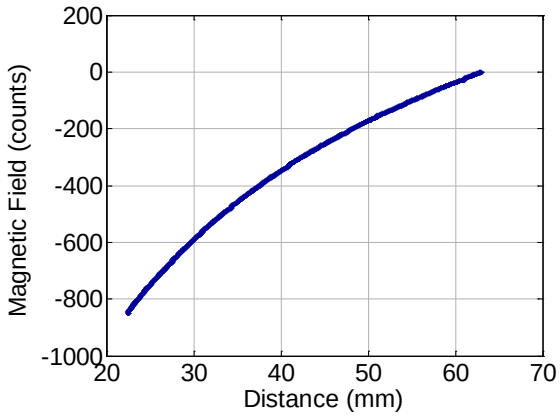


Figure 3-6. Magnetic field vs. distance from the magnetic sensor.

Two methods are developed to identify model parameters which are described in the following sections.

### 3.2.2.1. Method 1 – Least Squares

Defining $q = \frac{p}{x_{p0}+e}$, we can rewrite (3-8) as

$$B_{xi} = \frac{q(x_{p0}+e)}{x_{pi}+e} - q \quad \Longrightarrow \quad (B_{xi}+q)(x_{pi}+e) = q(x_{p0}+e) \quad \Longrightarrow$$
$$B_{xi}x_{pi} = -B_{xi}e - (x_{pi}-x_{p0})q, \tag{3-9}$$

where $i = 1, 2, \dots, N$, and $N$ is the number of samples. Now we can combine all the measurements from the magnetic sensor, $B_{xi}$'s, and the LVDT, $x_{pi-LVDT}$'s, and use the least squares (LS) method to fit a curve to the data points. The parameter to be estimated is

$$X = [p \quad q]. \tag{3-10}$$

The measurement equation is

$$Z = HX + n \qquad n \sim (0, R), \tag{3-11}$$

$$Z = [B_{x1}x_{p1-LVDT} \quad B_{x2}x_{p2-LVDT} \quad \dots \quad B_{xn}x_{pn-LVDT}]^T, \tag{3-12}$$

$$H = \begin{bmatrix} -B_{x1} & -(x_{p1-LVDT} - x_{p0-LVDT}) \\ -B_{x2} & -(x_{p2-LVDT} - x_{p0-LVDT}) \\ \vdots & \vdots \\ -B_{xn} & -(x_{pn-LVDT} - x_{p0-LVDT}) \end{bmatrix}. \tag{3-13}$$

The LS solution is

$$\hat{X} = (H^T H)^{-1} H^T Z. \tag{3-14}$$

The estimated values of $p$ and $e$ are shown in Table 3-1 (Method 1). The fitted curve and the error are shown in Figures 3-9 and 3-10, respectively.

#### 3.2.2.2. Method 2 – Minimax Fitting

The LS algorithm is based on minimizing the square of the errors or the following expression:

$$J = \|\varepsilon\|_2^2 = \varepsilon^T \varepsilon = (Z - HX)^T (Z - HX), \tag{3-15}$$

and the error in the previous case is

$$\varepsilon = \left( B_x x_{p-LVDT} - \begin{bmatrix} -B_x & -\left(x_{p-LVDT} - x_{p0-LVDT}\right) \end{bmatrix} \begin{bmatrix} \hat{e} \\ \hat{q} \end{bmatrix} \right). \tag{3-16}$$

However, we are interested in finding $p$ and $e$ that minimize the error between the distance obtained from magnetic sensor and the distance from LVDT uniformly across the piston motion range. In other words, it is desired to minimize the maximum error or minimize the infinity norm of the error. This problem can be written as

$$\text{minimize} \max_i \left| x_{pi-LVDT} - x_{pi-AMR} \right|, \tag{3-17}$$

where

$$x_{pi-AMR} = \frac{q x_{p0-LVDT} - B_{xi} e}{B_{xi} + q}. \tag{3-18}$$

We can rewrite problem (3-18) by defining a new variable and transforming it into a problem with linear objective as

$$\begin{aligned} &\text{minimize} && \gamma \\ &\text{subject to} && \left( x_{pi-LVDT} - \frac{q x_{p0-LVDT} - B_{xi} e}{B_{xi} + q} \right) \le \gamma \qquad i = 1,2,\dots,N \\ &\& && -\left( x_{pi-LVDT} - \frac{q x_{p0-LVDT} - B_{xi} e}{B_{xi} + q} \right) \le \gamma \qquad i = 1,2,\dots,N. \end{aligned} \tag{3-19}$$

Considering Figure 3-6, we can see that the magnetic field decreases as the piston moves from its initial position, $x_{p0}$, and gets closer to the magnetic sensor. Thus, we should have

$$\frac{p}{x_{p0-LVDT}+e} = q \leq -B_{xi} \quad \& \quad i = 1,2,\dots,N. \tag{3-20}$$

Now we can write the problem defined by (3-19) as

$$\begin{aligned} &minimize && \gamma \\ &subject\ to && \left(\gamma - x_{pi-LVDT} + x_{p0-LVDT}\right)q - B_{xi}e \leq \left(x_{pi-LVDT} - \gamma\right)B_{xi} \\ &\& && \left(\gamma + x_{pi-LVDT} - x_{p0-LVDT}\right)q + B_{xi}e \leq \left(-x_{pi-LVDT} - \gamma\right)B_{xi} \\ &\& && q + B_{xi} \leq 0 \\ & && i = 1,2,\dots,N. \end{aligned} \tag{3-21}$$

The problem defined by (3-21) can be solved iteratively using the bisection algorithm [71] as follows:

--Assume that the optimal $\gamma$ is in the interval $[l, u]$.

--Repeat solving feasibility problem for $\gamma = (u + l)/2$

$$\left(\gamma - x_{pi-LVDT} + x_{p0-LVDT}\right)q - B_{xi}e \leq \left(x_{pi-LVDT} - \gamma\right)B_{xi}$$

$$\left(\gamma + x_{pi-LVDT} - x_{p0-LVDT}\right)q + B_{xi}e \leq \left(-x_{pi-LVDT} - \gamma\right)B_{xi}$$

$$q + B_{xi} \leq 0$$

$$i = 1,2,\dots,N.$$

--if feasible $u \coloneqq \gamma$, if infeasible $l \coloneqq \gamma$.

--until $u - l \leq \epsilon$.

With this method, we will get the optimal $p$ and $e$ which are presented in Table 3-1 (Method 2). The fitted curve and the error are shown in Figures 3-9 and 3-10, respectively. As it can be seen from Table 3-1, the maximum error is reduced by about 20% compared with using the LS method.

### 3.2.3. Parameter Identification for Position Measurement System Using Only Magnetic Sensors (Method 3)

In the previous section, we obtained the equation parameters, $p$ and $e$, by fitting a curve to the magnetic field vs. actual distance data points. The actual distance was obtained from the installed LVDT on the FPE. However, if there is not an LVDT or other type of displacement measurement sensors available, these methods cannot be applied. In a real-world engine on a car, no additional displacement sensor is likely to be available. In this section, we will describe how to use only two magnetic sensors to obtain the equation parameters. With this method, one can estimate the position of the piston using magnetic sensors without the need of any additional distance sensors for calibration. The two magnetic sensors are placed along the longitudinal axis of motion of the cylinder. The distance between the two sensors is $d = 38$ mm.

We will have the following measurement equations for the two sensors:

$$\begin{cases} B1_x = \dfrac{p}{x_p + e} - \dfrac{p}{x_{p0} + e}, \\ B2_x = \dfrac{p}{x_p + e + d} - \dfrac{p}{x_{p0} + e + d}. \end{cases} \tag{3-22}$$

Solving for $x_p$ from the first equation in (3-22) and replacing into the second equation in (3-22), we get:

$$x_p = \frac{p}{B1_x + \frac{p}{e + x_{p0}}} - e, \tag{3-23}$$

$$B2_x = \frac{p}{d + \frac{p}{B1_x + \frac{p}{e + x_{p0}}}} - \frac{p}{d + e + x_{p0}}. \tag{3-24}$$

We can use (3-24) and the data points from the two magnetic sensors to obtain $p$ and $e$ by applying the iterated nonlinear least squares method. However, it was observed that the parameter estimates did not converge consistently in this case. In order to make the algorithm converge reliably, the measurements from the final position of the piston can be included in the measurements which are

$$\begin{cases} B1_{xf} = \dfrac{p}{x_{pf} + e} - \dfrac{p}{x_{p0} + e}, \\ B2_{xf} = \dfrac{p}{x_{pf} + e + d} - \dfrac{p}{x_{p0} + e + d}. \end{cases} \tag{3-25}$$

In general, this final point would be available by only knowing the stroke length of the piston. In other words, to use this proposed method, one only needs to move the piston a full stroke, record the magnetic sensors measurements and know the stroke length of the piston. Thus, we will have the following measurements:

$$\begin{cases} B2_{xi} = h_1(B1_x, p, e) + v_{1i} & i = 1,2, \dots, N, \\ B1_{xf} = h_2\left(x_{pf}, p, e\right) + v_2, \\ B2_{xf} = h_3\left(x_{pf}, p, e\right) + v_3, \end{cases} \tag{3-26}$$

$$h_1(B1_x, p, e) = \frac{p}{d + \frac{p}{B1_x + \frac{p}{e + x_{p0}}}} - \frac{p}{d + e + x_{p0}}, \tag{3-27}$$

$$h_2\left(x_{pf}, p, e\right) = \frac{p}{x_{fp} + e} - \frac{p}{x_{p0} + e}, \tag{3-28}$$

$$h_3(x_{pf}, p, e) = \frac{p}{x_{fp} + e + d} - \frac{p}{x_{p0} + e + d}. \tag{3-29}$$

Here the noise was assumed to be additive for simplicity. Next, the iterated nonlinear least squares method [52] is utilized to identify model parameters $p$ and $e$. Recall from Section 3.2.1 that $e$ is the effective height of the piston which is expected to be less than $a$, the actual height of the piston. Therefore, it is reasonable to use $a$ as the initial value for $e$. An initial value of $p$ can be obtained by plugging the initial value of $e$ in either of the equations of (3-22).

Following the proposed method, the piston was moved a full stroke. Figure 3-7 shows the measurements from the two magnetic sensors. Note that sensor 2 signals are of less amplitude compared with sensor 1 since sensor 2 is placed farther away from the piston by a distance $d$. The values of parameters $p$ and $e$ were obtained by applying the iterated nonlinear least squares method and are shown in Figure 3-8 over iteration. The final values are presented in Table 3-1 (Method 3). The fitted curve and the error are shown in Figures 3-9 and 3-10, respectively. It can be seen that using only two magnetic sensors without any other calibrating devices, we can achieve a maximum absolute error of ~0.4 mm.

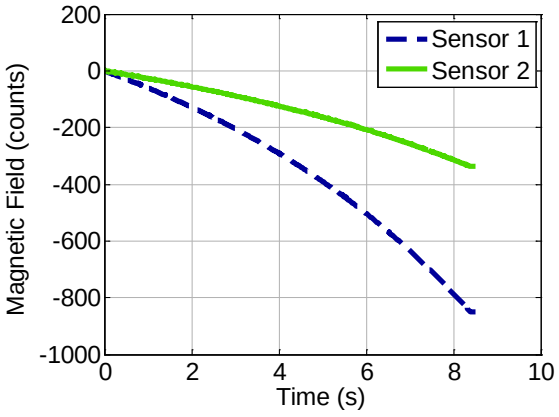


Figure 3-7. Magnetic field measurements from sensors 1 and 2.

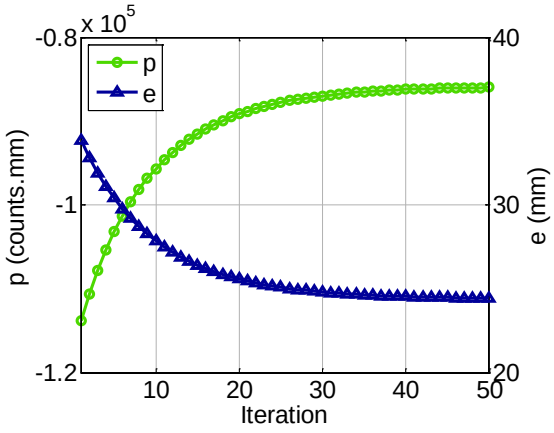


Figure 3-8. Values of parameters $p$ and $e$ over iterations.

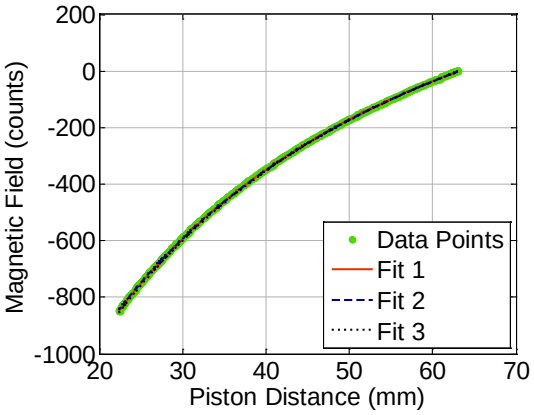


Figure 3-9. Fitted Curves.

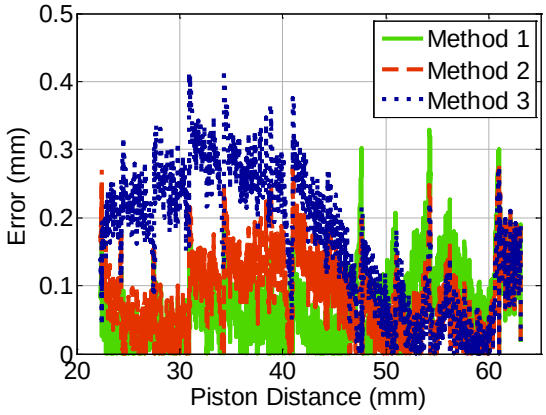


Figure 3-10. Position Error in fits using Methods 1, 2 and 3.

Table 3-1. Summary of Parameter Values and Maximum Errors.

| Method | $p$ | $e$ | Max Error (mm) |
|---|---|---|---|
| Method 1 – Least Squares | $-84043$ | 24.05 | 0.3294 |
| Method 2 – Minimax | $-88233$ | 25.66 | 0.2731 |
| Method 3 – Mag. sensors only | $-85844$ | 24.39 | 0.4141 |

Once we know the model parameters $p$ and $e$, we can calculate distance from the magnetic sensors using either one of the equations in (3-22) by solving for $x_p$. Figures 3-11 and 3-12 show the results of two additional experiments with the FPE. In the first experiment, the FPE started running at 2 Hz and the amplitude was increased over time. In the second experiment, the FPE started running at 2 Hz and the frequency increased to 5 Hz during the test. It can be seen that in both cases, the magnetic sensors provide an excellent estimate of the piston position as verified by the LVDT.

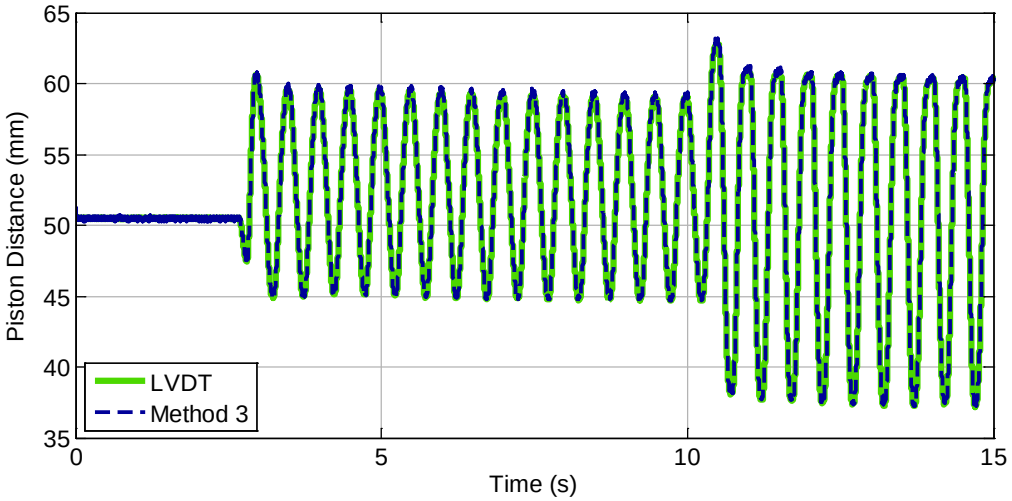


Figure 3-11. Experimental results 1: FPE operating at 2 Hz with an increase in amplitude during the experiment.

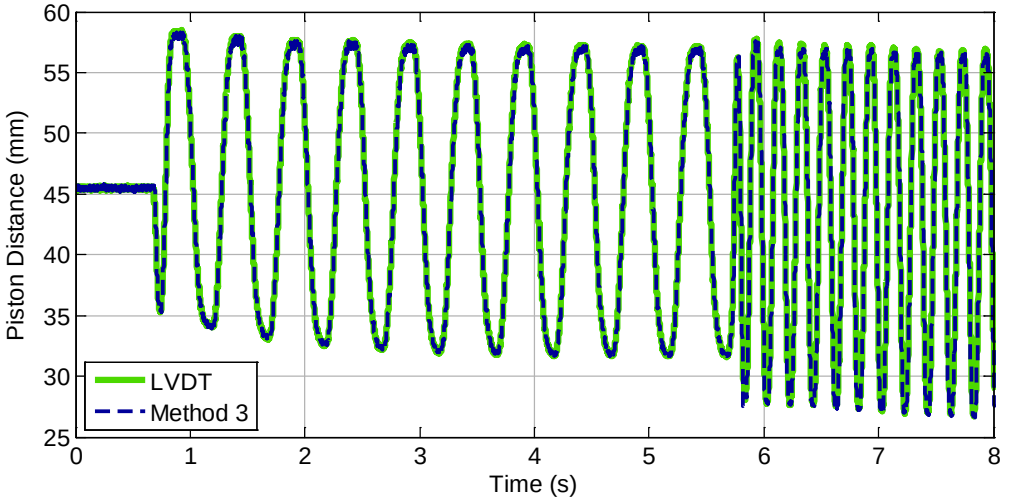


Figure 3-12. Experimental results 2: FPE operating at 2 Hz with an increase in frequency to 5 Hz during the experiment.

### 3.2.4. Adaptive Real-time Estimation of Model Parameters and Piston Position (Methods 4 and 5)

In Section 3.2.3, a method was proposed for estimation of the model parameters in (3-8) by using two magnetic sensors (Method 3). In the proposed method, the piston was moved a full stroke and the magnetic sensors measurements were recorded. Next, the iterated nonlinear least squares method was applied to estimate the model parameters, $p$ and $e$. Finally, the estimated parameters were used along with (3-22) to estimate piston position. In this section, two other methods (methods 4 and 5) are proposed for real-time estimation of both piston position, $x_p$, and model parameters, $p$ and $e$. The main advantage of these methods is that it will not be necessary to interrupt the regular operation of the engine and artificially move the piston a full stroke. The sensors and the required electronics can be placed along the axis of the piston and as the piston is continuing its normal operation, model parameters as well as piston position be estimated. Also, any changes in the values of model parameters over time can be automatically captured. The two proposed methods are described in the following sections.

#### 3.2.4.1. Method 4 – Extended Kalman Filter (EKF) for Adaptive Parameter and Position Estimation

As it was mentioned earlier, the objective of adaptive position estimation is to estimate both piston position and model parameters in real time so that it will not be necessary to interrupt the normal operation of the piston. Therefore, the variables to be estimated are $x_p, p$ and $e$. Also the two magnetic sensors, placed along the longitudinal axis of motion of the cylinder, provide measurements described by (3-22).

Using the extended Kalman filter (EKF) [52, 53], we can measure magnetic field from two magnetic sensors and estimate the variables. The state to be estimated is (dropping index $p$ from $x$):

$$X = [x \quad v \quad a \quad p \quad e]^T, \tag{3-30}$$

where $x$, $v$ and $a$ are the piston position, velocity, and acceleration, respectively, and $p$ and $e$ are the model parameters. The system equations are

$$X_k = FX_{k-1} + w_{k-1} \qquad w_k \sim (0, Q), \tag{3-31}$$

$$F = \begin{bmatrix} 1 & dt & 0 & 0 & 0 \\ 0 & 1 & dt & 0 & 0 \\ 0 & 0 & 1 & 0 & 0 \\ 0 & 0 & 0 & 1 & 0 \\ 0 & 0 & 0 & 0 & 1 \end{bmatrix}, \tag{3-32}$$

where $dt$ is the sampling time. The measurement equations are

$$z_k = h(X_k, n_k) \qquad n_k \sim (0, R), \tag{3-33}$$

$$z_k = [B_{1k} \quad B_{2k}]^T, \tag{3-34}$$

$$h(X_k, n_k) = \begin{bmatrix} \dfrac{p_k}{x_k + e_k} - \dfrac{p_k}{x_0 + e_k} + n_k^1 \\ \dfrac{p_k}{x_k + e_k + d} - \dfrac{p_k}{x_0 + e_k + d} + n_k^2 \end{bmatrix}, \tag{3-35}$$

where $d$ is the distance between the two magnetic sensors. Also, the acceleration of the piston is assumed to be zero-mean which is a reasonable assumption considering the alternating motion of the piston. The EKF time update is performed as

$$\hat{X}_k^- = FX_{k-1}^+, \tag{3-36}$$

$$P_k^- = FP_{k-1}^+F^T + Q. \tag{3-37}$$

The EKF measurement update is performed as

$$K_k = P_k^- H_k^T (H_k P_k^- H_k^T + R_k)^{-1}, \tag{3-38}$$

$$\hat{X}_k^+ = \hat{X}_k^- + K_k\left[Z_k - h_k\left(\hat{X}_k^-, 0\right)\right], \tag{3-39}$$

$$P_k^+ = (I - K_k H_k) P_k^-, \tag{3-40}$$

$$H_k = \left.\frac{\partial h}{\partial X}\right|_{\hat{X}_k^-} = \left[\begin{array}{cccc} -\frac{p}{(x+e)^2} & 0 & 0 & \frac{1}{x+e} - \frac{1}{x_0+e} \quad \ldots \\ -\frac{p}{(x+e+d)^2} & 0 & 0 & \frac{p}{x+e+d} - \frac{1}{x_0+e+d} \quad \ldots \end{array}\right.$$
$$\left.\begin{array}{c} \ldots \quad -\frac{p}{(x+e)^2} + -\frac{p}{(x_0+e)^2} \\ \ldots \quad -\frac{p}{(x+e+d)^2} + -\frac{p}{(x_0+e+d)^2} \end{array}\right]\Bigg|_{\hat{X}_k^-}. \tag{3-41}$$

The initial value for $e$ is set as the piston height $a$, similar to Method 3. The initial value for $p$ is set close to zero. The method was then applied to a portion of data obtained from a test with FPE where the piston motion has reached its steady-state behavior. The results are shown in Figures 3-13 to 3-15.

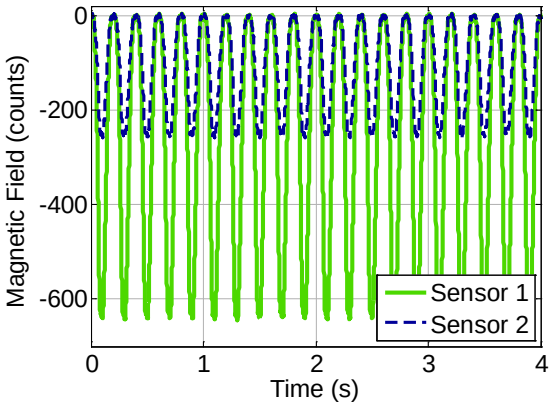


Figure 3-13. Magnetic field measurements from sensors 1 and 2.

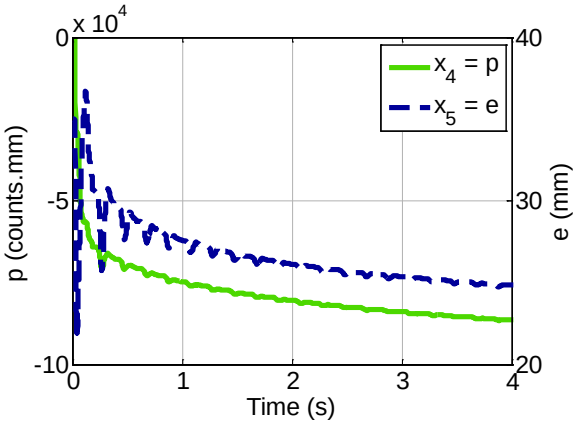


Figure 3-14. Parameters estimates over time.

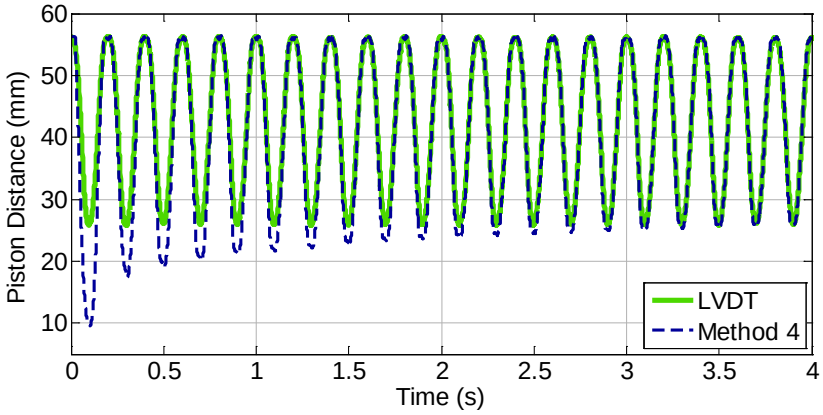

Figure 3-15. Position estimates and comparison with the LVDT.

As can be seen from Figure 3-15, it takes several cycles until the estimated piston position converges to the actual piston position. However, it is possible to further improve the performance of the estimator by using the fact that the stroke length of a piston is usually known. The resulting improved estimator is described in the following section.

#### 3.2.4.2. Method 5 – EKF for Adaptive Parameter and Position Estimation Using the Stroke Length Information

From the geometry of the piston inside the engine and the location of the magnetic sensors with respect to the engine, it is possible to know the minimum and maximum distances of the piston from the magnetic sensors. In other words, the min and max of the piston position, $x$, are known which are synchronized with min and max of the measured magnetic fields. For example, considering Figures 3-13 and 3-15, it can be seen that the magnetic field reading is about zero when the piston is furthest from the sensors (this is because initially at $t = 0$, the piston was at the furthest location from magnetic sensors and the initial magnetic field at $t = 0$ is subtracted from the measurements). When the piston comes to the closest distance to AMR sensors, $x = x_f$, the absolute value of the

magnetic field reaches its maximum. Thus, similar to (3-25) we will have the following extra measurements at this particular instant in time:

$$\begin{cases} B1_{xf} = \dfrac{p}{x_f + e} - \dfrac{p}{x_{p0} + e}, \\ B2_{xf} = \dfrac{p}{x_f + e + d} - \dfrac{p}{x_{p0} + e + d}. \end{cases} \tag{3-42}$$

These extra measurements can be integrated into the EKF designed in the previous section to update $p$ and $e$ whenever a peak in magnetic field is detected. The results from the new estimator are shown in Figures 3-16 and 3-17. As can be seen from Figure 3-17, estimated piston position converges to the actual piston position within a couple of cycles. The parameter estimates over time are shown in Figure 3-16.

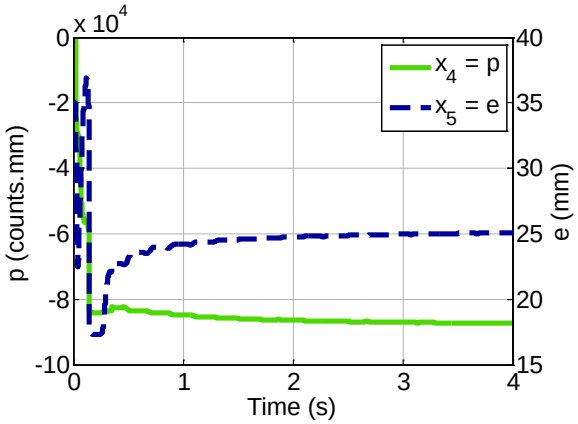


Figure 3-16. Parameters estimates over time using Method 5.

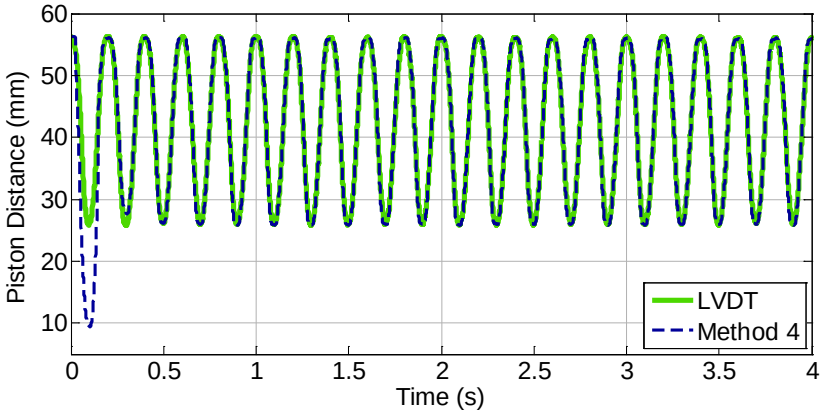


Figure 3-17. Position estimates obtained using Method 5 and comparison with the LVDT.

## 3.3. Piston Position Estimation in a Pneumatic Actuator

In Section 3.2, we developed techniques for piston position estimation in a free piston engine by exploiting the inherent magnetic field of the piston. In this section, it is shown that if the piston lacks inherent magnetic field, a small magnet can be attached to it and the same developed techniques be applied to estimate piston position from magnetic field measurements. A pneumatic actuator is used for the experiments.

The experimental setup is described in Section 3.3.1. A model for the magnetic field due to the small magnet added to the piston head is derived in Section 3.3.2. Parameter identification of the proposed model and the experimental results are presented in Section 3.3.3.

### 3.3.1. Experimental Setup

Figure 3-18 shows the experimental setup used to evaluate the performance of the proposed sensing principle. The setup consists of a pneumatic actuator, two external magnetic sensors with a separation of 28 mm between them, a linear variable differential transformer (LVDT) which is used as a reference position sensor for comparison, and electronics to read sensors outputs. The LVDT has a linearity of $\pm 0.25$ mm and a Bandwidth of 200 Hz.

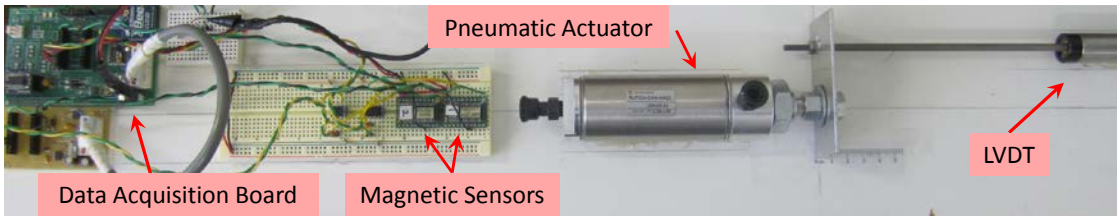


Figure 3-18. Test setup for performance analysis of the proposed sensing principle.

The piston of the pneumatic actuator used is made of paramagnetic materials (the piston and the piston rod are made of aluminum and type 303 stainless steel, respectively) and lacks inherent magnetic field. Thus, it does not create a change in the magnetic field when it is moved from one end to the other end. Thus, a small magnet (5 mm diameter and 1 mm thickness) is attached to the piston head as shown in Figure 3-19.

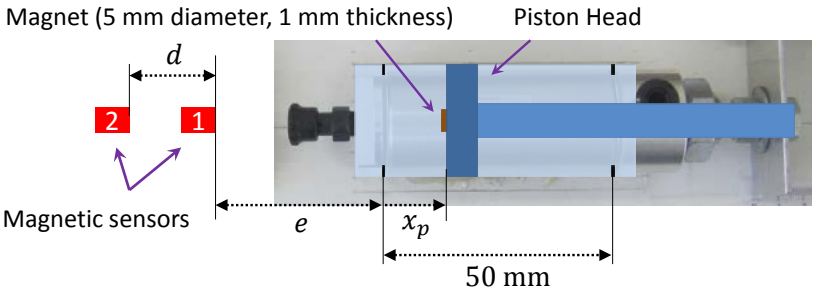


Figure 3-19. A small magnet is attached to the piston head.

After adding the magnet to the piston head, changes in the magnetic field are observed with the motion of the piston. Figure 3-20 shows the measured magnetic field

from the two magnetic sensors as the piston moves a full stroke. In the next section, we develop a model relating the magnetic field measurements to the piston position.

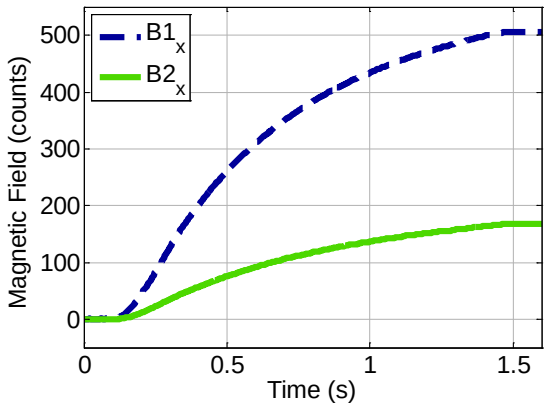


Figure 3-20. Sensors readings when the piston is moved a full stroke.

### 3.3.2. Magnetic Field Model

Considering Figure 3-19, we want to obtain a mathematical relation between the magnetic field measured by magnetic sensor 1, $B_x$, and the piston position $x_p$.

The sensors are about 70 mm from the piston head at the closest distance ($x_p = 0$). On the other hand, the size of the magnet attached to the piston head (1 mm in thickness and 5 mm in diameter) is very small compared with this distance. Therefore, it is reasonable to assume that the magnetic field at the location of the magnetic sensors due to the attached magnet can be modeled as a dipole. The magnetic field of a dipole at a distance $x$ along its axis is given by [41]:

$$B_x = \frac{\mu_0 m_0}{2\pi x^3}, \tag{3-43}$$

where $B_x$ is the magnetic field, $m_0$ is the dipole magnetic moment and $\mu_0$ is the permeability of free space. Defining $e$ as the initial distance between the piston head and

sensor 1, $x_p$ as the piston position (changing from $x_p = 0$ mm to $x_p = 50$ mm), and $p = \frac{\mu_0 m_0}{2\pi}$, we can rewrite (3-43) as

$$B_x = \frac{p}{\left(x_p + e\right)^3}. \tag{3-44}$$

Since we subtract the static magnetic field at the beginning of each test, which also includes any field created by the outer piston at its initial position $x_{p0}$, the magnetic field measured by sensor 1 can be written as

$$B_x = \frac{p}{\left(x_p + e\right)^3} - \frac{p}{\left(x_{p0} + e\right)^3}. \tag{3-45}$$

Subtracting the initial magnetic field is needed in order to remove the influence of the Earth's magnetic field and other static or slowly varying magnetic fields. In order to use (3-45) for position estimation, we need to know the three parameters $p$, $e$ and $x_{p0}$. However, it is not possible to estimate all three of these parameters from this equation, even if we use two sensors instead of one sensor, since the system becomes unobservable for the three unknown parameters. Therefore, we will assume that $x_{p0}$ is known. Basically, we can start the piston from a known initial position (at the lower or upper bounds of motion of the piston, $x_p = 0$ mm or $x_p = \text{Stroke Length}$) for the first time and subsequently record the final position in a memory to use it as the initial position for the next run. In the following section, we use Method 3 developed in Section 3.2.3 to estimate the model parameters. Once we know the model parameters, we can use (3-45) to estimate piston position $x_p$ by measuring magnetic field $B_x$.

### 3.3.3. Magnetic Field Model Parameter Identification

The parameter identification methods developed in Section 3.2 were developed for parameter identification of a magnetic field model due to a rectangular piston with inherent magnetic field. Magnetic field $B_x$ had a linear relationship with $1/x_p$ in the derived mathematical model. With the nonmagnetic piston and the tiny magnet in this section, the relationship between $B_x$ and $1/x_p$ is cubic as expressed by (3-45). However, we can use the same developed methods for identification of model parameters as long as we have a model relating $B_x$ and $x_p$. The parameter identification Methods 3 to 5 are based on using two magnetic sensors and does not require any additional sensors for calibration. Here, we utilize Method 3 for identification of the pneumatic actuator model parameters. Consider the two magnetic sensors placed on the longitudinal axis of the cylinder as shown in Figure 3-18. We will have the following equation for the two sensors:

$$\begin{cases} B1_x = \dfrac{p}{\left(x_p + e\right)^3} - \dfrac{p}{\left(x_{p0} + e\right)^3}, \\ B2_x = \dfrac{p}{\left(x_p + e + d\right)^3} - \dfrac{p}{\left(x_{p0} + e + d\right)^3}, \end{cases} \tag{3-46}$$

where $d$ is the distance between the two sensors which is known. Defining $q = \frac{p}{\left(x_{p0}+e\right)^3}$ and solving for $x_p$ from the first equation in (3-46) we have:

$$x_p = \left(\frac{p}{B1_x + q}\right)^{1/3} - e. \tag{3-47}$$

Replacing $x_p$ in the second equation of (3-46) using (3-47), we have:

$$B2_x = \frac{p}{\left(\left(\frac{p}{B1_x + q}\right)^{1/3} + d\right)^3} - \frac{p}{\left(x_{p0} + e + d\right)^3}. \tag{3-48}$$

We can use (3-48) and the data points from the two magnetic sensors to obtain $p$ and $e$ by applying the iterated nonlinear least squares method [52]. Besides these data points, moving the piston a full stroke, $x_p = x_{p0} = 0$ to $x_p = x_{pf} = Stroke\ Length$, the following two measurements can be also adopted:

$$\begin{cases} B1_{xf} = \dfrac{p}{\left(x_{pf} + e\right)^3} - \dfrac{p}{\left(x_{p0} + e\right)^3}, \\ B2_{xf} = \dfrac{p}{\left(x_{pf} + e + d\right)^3} - \dfrac{p}{\left(x_{p0} + e + d\right)^3}. \end{cases} \tag{3-49}$$

Therefore, moving the piston a full stroke, we will have $N + 2$ measurements:

$$\begin{cases} B2_{xi} = h_1(B1_x, p, e) + v_{1i} & i = 1,2, \dots, N, \\ B1_{xf} = h_2\left(x_{pf}, p, e\right) + v_2, \\ B2_{xf} = h_3\left(x_{pf}, p, e\right) + v_3, \end{cases} \tag{3-50}$$

where function $h_1$ is defined by (3-48), and functions $h_2$ and $h_3$ are defined by (3-49). Here, the noise is assumed to be additive for simplicity and $N$ is the number of samples taken during the motion of the piston. Next, we can use the iterated nonlinear least squares method and the measurements from the two sensors (shown in Figure 3-20) to identify model parameters $p$ and $e$. Recall from the previous section that $e$ is the initial distance between the piston head and magnetic sensors. Therefore, we can get a rough initial estimate of $e$ by guessing or using a ruler. An initial value of $p$ can be obtained by plugging the initial value of $e$ in either of the equations of (3-46). The values of the estimated parameters over iterations are shown in Figure 3-21. Thus, the actual values of the parameters are obtained automatically from this algorithm.

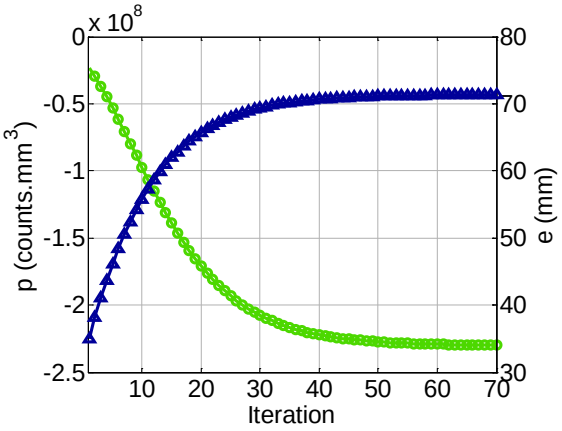


Figure 3-21. Values of parameters $p$ and $e$ over iterations.

Knowing the model parameters, we can use either one of the equations in (3-47) and get an estimate of $x_p$ at each time instant as shown in Figure 3-22. Comparing estimated position from magnetic sensors and the LVDT, we can calculate the error in the proposed sensing system which is shown in Figure 3-23.

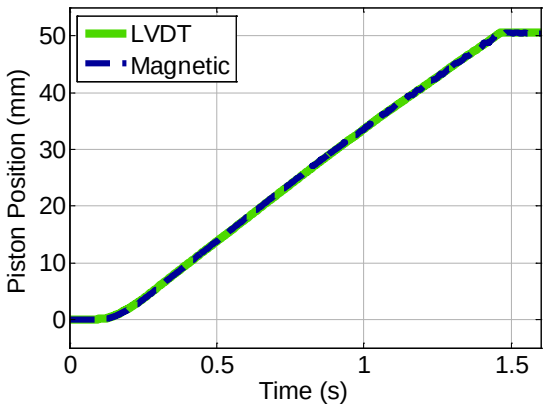


Figure 3-22. Piston position obtained from LVDT and magnetic sensors.

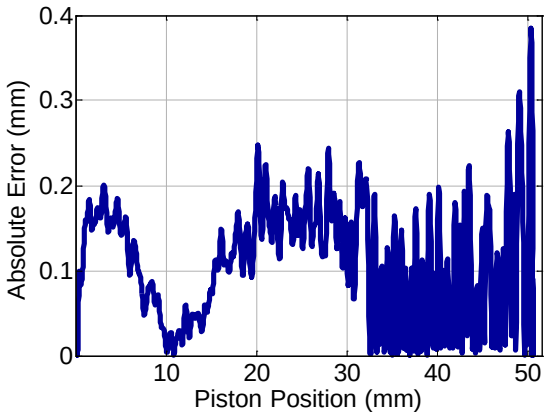


Figure 3-23. Error in position estimation.

Figure 3-23 shows that the maximum error is less than 0.4 mm. Therefore, using the developed magnetic field model, two inexpensive magnetic sensors and the proposed calibration algorithm, we can develop a position sensing system with an accuracy of 0.4 mm without the need of any other type of sensors. It is worth mentioning that the exact value of the initial distance between the sensors and piston head, $e$, is obtained as

one of the parameters of the sensing system. Therefore, it is not required to measure this distance accurately; rather a rough estimate is adequate. As seen from Figure 3-21, the initial value of $e$ is set to half of the actual value and yet the proposed method is able to identify the true values of the parameters.

Video 3-1 shows a demo of the real-time estimation system developed in MATLAB using a PC and an embedded microcontroller. In this demo, Method 3 has been used to identify model parameters. The value of "Est Piston Position (mm)" is obtained by using the measurements of magnetic sensor 1 and the first equation of (3-47). The difference between this value and the value obtained by using the measurements of magnetic sensor 2 and the second equation of (3-47) is shows as "Error (mm)". Video 3-1 is also included in supplementary files.

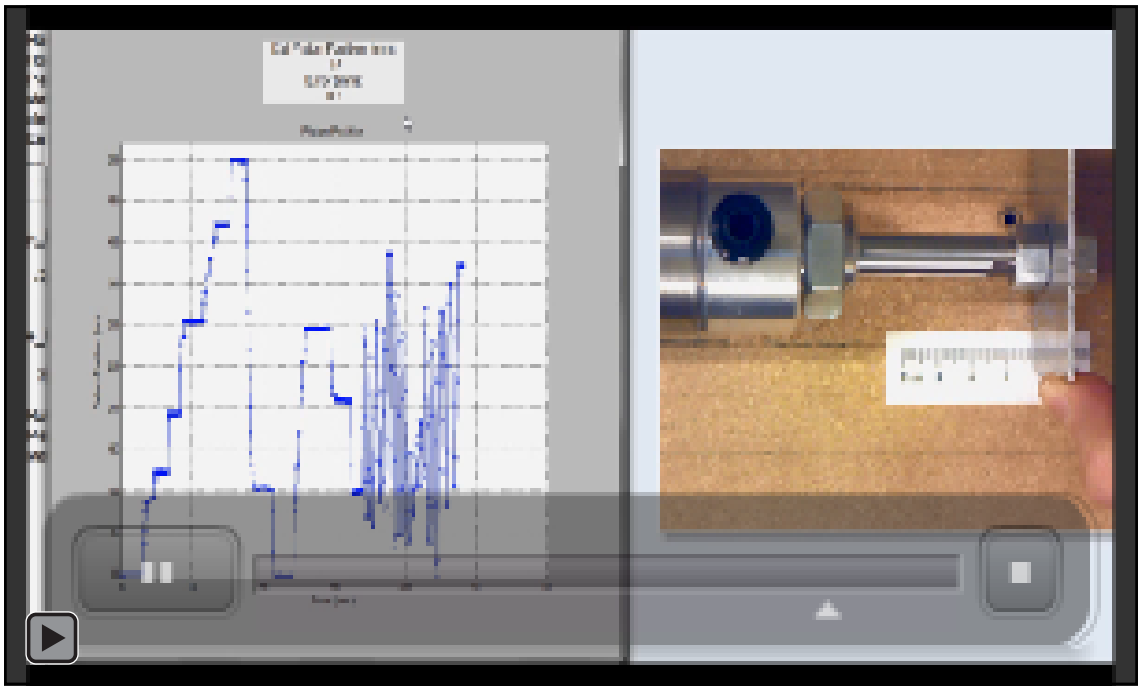

Video 3-1. A demo of the real-time estimation system developed in MATLAB. This video is also included in supplementary files.

## 3.4. Summary of the Position Estimation Method

The position measurement approach described above for piston position measurement can be generalized and applied to position measurement for a number of other objects. The general steps that should be followed are described below:

1. Derive an analytical function modeling the magnetic field around the ferrous object as a function of distance from the object. Therefore, we have:

$$B_x = f(x_p, \lambda), \tag{3-51}$$

where $x_p$ is the piston position, $\lambda$ is a vector of model parameters, and $B_x$ is the measured magnetic field. The function $f(x_p, \lambda)$ should be injective and invertible for $x_p$ so that we can calculate the function $g$ where:

$$x_p = g(B_x, \lambda) = f^{-1}(B_x, \lambda). \tag{3-52}$$

Equation (3-47) shows an example of the function $g$. Note that if the function $f$ is not injective and/or invertible, the methods described in Section 3.2.4 can be used to adaptively estimate both model parameters as well as position in real time.

2. Place two magnetic sensors along the axis of motion of the piston with a spacing of $d$. The magnetic field measured by the sensors will have the following relation with $x_p$:

$$\begin{cases} B1_x = f(x_p, \lambda), \\ B2_x = f(x_p + d, \lambda). \end{cases} \tag{3-53}$$

Using (3-52) we get:

$$B2_x = f(g(B_x, \lambda) + d, \lambda). \tag{3-54}$$

The significance of (3-54) is that it is not dependent on piston position $x_p$. Model parameters can be estimated from this equation using the measurements from the two sensors. Therefore, no other reference sensors are required for calibration.

3. Move the piston a full stroke and record sensor measurements. Using these magnetic measurements and the fact that the stroke length of the cylinder is known, the following measurements are available:

$$\begin{cases} B2_{xi} = f(g(B_{xi}, \lambda) + d, \lambda) + n_{1i} \quad i = 1,2, \dots, N, \\ B1_{xf} = f(x_{pf}, \lambda) + n_2, \\ B2_{xf} = f(x_{pf} + d, \lambda) + n_3, \end{cases} \tag{3-55}$$

where $N$ is the number of samples taken during the piston motion and $n$ is the measurement noise.

4. Apply iterated nonlinear least squares or other parameter identification algorithms to identify model parameters $\lambda$.
5. Knowing model parameters $\lambda$, use (3-52) to estimate piston position $x_p$ in real time, by measuring the magnetic field $B_x$.

## 3.5. Robust Piston Position Estimation with Additional Magnetic Sensors

In this section, we consider the problem of external disturbance on the magnetic sensors due to unexpected presence of other ferromagnetic objects. The disturbance can cause inaccuracies in piston position estimation. As an example, consider Figure 3-24 which shows the actual piston position as measured by the LVDT in an experiment with the pneumatic actuator setup (shown in Figure 3-18). Figure 3-25 shows the signal from the magnetic sensor for the same test which gets affected by an external disturbance at $t \cong 16$ s. The disturbance is created by bringing a ferromagnetic object (pliers shown in

Figure 3-26) from a far distance (with no impact on the sensor) close to the sensor. Consequently, the sensor signal starts deviating from its actual value (at $t \cong 16$ s) and reaches a final value as the object is placed next to the sensor. If we do not correct for this disturbance, the position estimate that we obtain from the magnetic sensors will be quite inaccurate as shown in Figure 3-25. In this test, the error caused by the disturbance is as much as 10 mm.

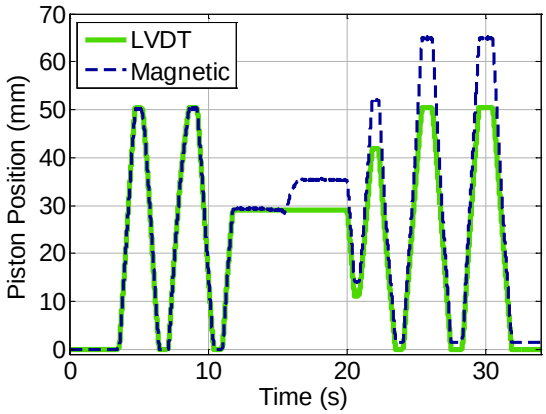


Figure 3-24. Piston position measured by LVDT and estimated from magnetic sensor when disturbance exists.

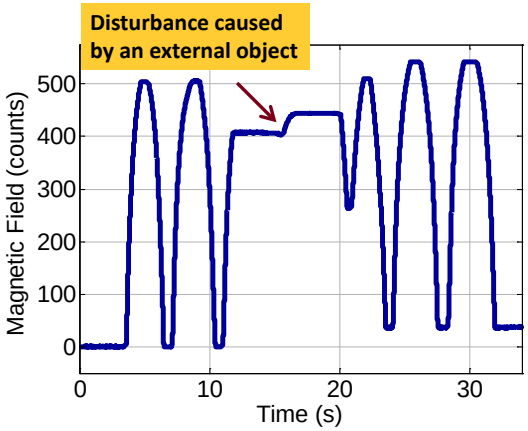


Figure 3-25. Magnetic sensor measurement which gets affected by the external disturbance.

Figure 3-26. The pliers used to create external magnetic disturbance.

In order to make the sensor system robust to external disturbance, a method is proposed which is based on using a quad arrangement of four magnetic sensors as shown in Figure 3-27.

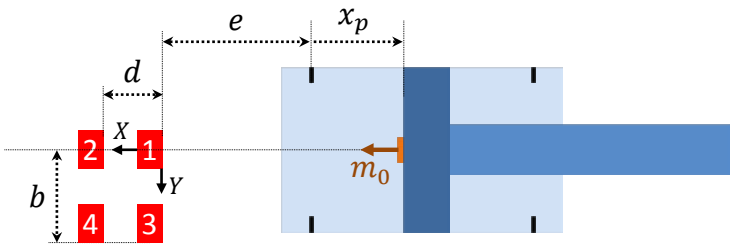


Figure 3-27. Sensor configuration for disturbance rejection algorithm.

In Section 3.3.2, we developed a mathematical model relating the magnetic field measured by the sensors 1 and 2 to piston position. For the proposed disturbance rejection algorithm, we first derive a model relating the magnetic field measured by sensors 3 and 4, which are offset from the axis of motion of the piston, to the piston position.

### 3.5.1. Magnetic Field Model for Sensors Off the Axis of Motion of the Piston

Considering Figure 3-28, we have [41]:

$$B_r = \frac{\mu_0 m_0}{2\pi r^3}\cos(\alpha), \tag{3-56}$$

$$B_\alpha = \frac{\mu_0 m_0}{4\pi r^3}\sin(\alpha). \tag{3-57}$$

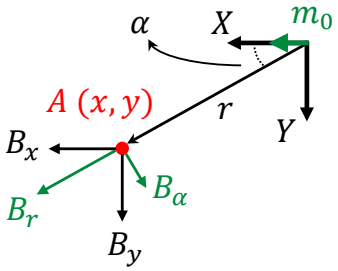


Figure 3-28. Magnetic field of a dipole when sensor are placed on the side of the piston.

Assuming that a magnetic sensor is placed at point $A$ which measures $B_x$, we have:

$$B_x = \frac{\mu_0 m_0}{4\pi r^3}(2\cos^2\alpha - \sin^2\alpha). \tag{3-58}$$

If we express $r$ and $\alpha$ in terms of $x$ and $y$, and define $p = \frac{\mu_0 m_0}{2\pi r^3}$, we get:

$$B_x = \frac{p(2x^2 - y^2)}{2(x^2 + y^2)^{5/2}}. \tag{3-59}$$

From Figure 3-27, we have $x = x_p + e$ and $y = b$ resulting in

$$B_x = \frac{p\left(2(x_p + e)^2 - b^2\right)}{2\left((x_p + e)^2 + b^2\right)^{5/2}}. \tag{3-60}$$

Finally, subtracting the initial magnetic field from the sensors, we get:

$$B_x = \frac{p\left(2(x_p + e)^2 - b^2\right)}{2\left((x_p + e)^2 + b^2\right)^{5/2}} - \frac{p\left(2(x_{p0} + e)^2 - b^2\right)}{2\left((x_{p0} + e)^2 + b^2\right)^{5/2}}. \tag{3-61}$$

The model parameters in (3-61) are $p$ and $e$ which we can estimate using sensors 1 and 2 and the method proposed in the previous sections, and $b$ which is known (similar to $d$). Note that (3-45) is a special case of (3-61) where $b = 0$. In the next section, the algorithm used for disturbance rejection is described.

### 3.5.2. Disturbance Rejection Algorithm

Considering Figure 3-27, we have the following measurements from the four sensors:

$$\begin{cases} B1_x = f_1(x_p), \\ B2_x = f_2(x_p) = f_1(x_p + d), \\ B3_x = f_3(x_p), \\ B4_x = f_4(x_p) = f_3(x_p + d), \end{cases} \tag{3-62}$$

where functions $f_1$ and $f_3$ are defined by (3-45) and (3-61), respectively. Now consider that a magnetic object gets close to the sensors and affects the sensors signals. As a result, the field measured by the sensors can be expressed as

$$\begin{cases} B1_x = f_1(x_p) + D_1, \\ B2_x = f_2(x_p) + D_2, \\ B3_x = f_3(x_p) + D_3, \\ B4_x = f_4(x_p) + D_4, \end{cases} \tag{3-63}$$

where $D_i$'s represent the influence of the external magnetic object on each sensor.

In general, the disturbance is unknown, and we do not have any information about $D_i$'s. Therefore, we have four equations and five unknowns, $D_i$'s and $x_p$. However, it is possible to impose a constraint on $D_i$'s. Since the four sensors are close to each other, we assume that we can fit a plane to the four disturbances added to the sensors.

A plane in 3-D space can be expressed as

$$z = \rho_1 x + \rho_2 y + \rho_3, \tag{3-64}$$

where $\rho_i$'s are the plane parameters. Now, consider three points in space: $(d, 0, D_2)$, $(0, b, D_3)$, and $(d, b, D_4)$. The plane which goes through these points in space can be obtained as

$$\begin{cases} D_2 = \rho_1 d + \rho_3 \\ D_3 = \rho_2 b + \rho_3 \\ D_4 = \rho_1 d + \rho_2 b + \rho_3 \end{cases} \Longrightarrow \begin{bmatrix} D_2 \\ D_3 \\ D_4 \end{bmatrix} = \begin{bmatrix} d & 0 & 1 \\ 0 & b & 1 \\ d & b & 1 \end{bmatrix} \begin{bmatrix} \rho_1 \\ \rho_2 \\ \rho_3 \end{bmatrix} \tag{3-65}$$

$$\Longrightarrow \begin{bmatrix}\rho_1\\ \rho_2\\ \rho_3\end{bmatrix} = \begin{bmatrix}d & 0 & 1\\ 0 & b & 1\\ d & b & 1\end{bmatrix}^{-1}\begin{bmatrix}D_2\\ D_3\\ D_4\end{bmatrix} = \begin{bmatrix}-D_3/d + D_4/d\\ -D_2/b + D_4/b\\ D_2 + D_3 - D_4\end{bmatrix}.$$

Assuming that the point $(0,0,D_1)$ is on the same plane, we have:

$$D_1 = c_1 = D_2 + D_3 - D_4 \implies D_1 - D_2 - D_3 + D_4 = 0. \tag{3-66}$$

Now, we can develop a real-time estimator to estimate piston position and the disturbances. The extended Kalman filter (EKF) is used for this purpose [52, 53]. The state to be estimated is

$$X = [x \quad v \quad a \quad D_1 \quad D_2 \quad D_3 \quad D_4], \tag{3-67}$$

where $x$, $v$, and $a$ are piston position, velocity, and acceleration, respectively. The time update equations are

$$X_k = FX_{k-1} + w_{k-1} \qquad w_k \sim (0, Q_k), \tag{3-68}$$

$$\hat{X}_k^- = F\hat{X}_{k-1}^+, \tag{3-69}$$

$$P_k^- = FP_{k-1}^+F^T + Q_{k-1}, \tag{3-70}$$

$$F = \begin{bmatrix}1 & dt & 0 & 0 & 0 & 0 & 0\\ 0 & 1 & dt & 0 & 0 & 0 & 0\\ 0 & 0 & 1 & 0 & 0 & 0 & 0\\ 0 & 0 & 0 & 1 & 0 & 0 & 0\\ 0 & 0 & 0 & 0 & 1 & 0 & 0\\ 0 & 0 & 0 & 0 & 0 & 1 & 0\\ 0 & 0 & 0 & 0 & 0 & 0 & 1\end{bmatrix}. \tag{3-71}$$

The measurement update equations are

$$Z = h(X, n) \qquad n \sim (0, R), \tag{3-72}$$

$$Z = [B1_x \quad B2_x \quad B3_x \quad B4_x \quad 0]^T, \tag{3-73}$$

$$h(X,n) = [f_1(x) + D_1 + n_1 \quad f_2(x) + D_2 + n_2 \quad f_3(x) + D_3 + n_3 \quad \ldots \quad \ldots \quad f_4(x) + D_4 + n_4 \quad D_1 - D_2 - D_3 + D_4 + n_5]^T, \tag{3-74}$$

$$R = diag([\sigma_B \quad \sigma_B \quad \sigma_B \quad \sigma_B \quad \sigma_{const}], \tag{3-75}$$

$$H_k = \left.\frac{\partial h}{\partial X}\right|_{\hat{X}_k^-}, \tag{3-76}$$

$$K_k = P_k^- H_k^T (H_k P_k^- H_k^T + R)^{-1}, \tag{3-77}$$

$$r_k = Z_k - h_k\left(\hat{X}_k^-, 0\right), \tag{3-78}$$

$$\hat{X}_k^+ = \hat{X}_k^- + K_k r_k, \tag{3-79}$$

$$P_k^+ = (I - K_k H_k) P_k^-. \tag{3-80}$$

Note that the imposed constraint on the disturbances $D_i$'s is included as a perfect measurement [72]. Since at the beginning of each test, the initial magnetic field is subtracted from the sensors readings, the estimator starts with zero disturbance. Therefore, the model uncertainty associated with disturbances, $Q_{i,i}$ $(i = 4,5,6,7)$, is set to zero. The measurement residual $r_k$ is small in this case. However, as soon as an external magnetic object creates a disturbance on the sensors readings, $r_k$ will increase and when it goes over a preset threshold, $Q_{i,i}$ $(i = 4,5,6,7)$ will be set to a nonzero value to allow for the estimation of the disturbances $D_i$'s. To have a smoother signal for threshold detection and avoid triggers by measurement noise, $r_k$ is filtered before checking if it has crossed the preset threshold.

### 3.5.3. Disturbance Rejection Algorithm Experimental Results

The proposed disturbance rejection algorithm was verified against several tests including the one shown in Figure 3-24. The measurements from the four sensors are shown in Figure 3-29 which shows how the external disturbance affects the sensors readings at $t \cong 16$ s. Figure 3-30 shows piston position measured by LVDT and estimated from the magnetic sensors over time. It can be seen that the estimated position momentarily deviates from the actual position after the disturbance affects the sensors but converges to the actual value after a short period of time. Figure 3-31 shows the disturbance estimation over time. Figure 3-32 shows the filtered measurement residual.

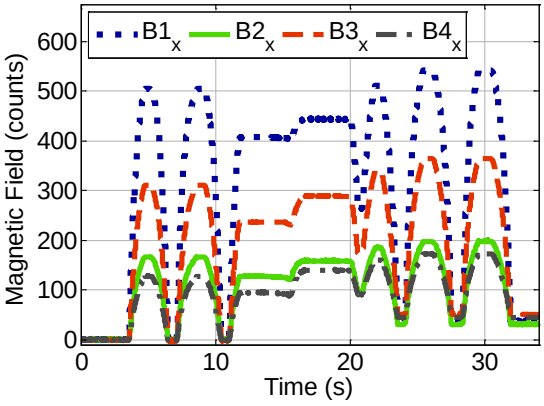


Figure 3-29. Magnetic field readings of the magnetic sensors which get affected by the external disturbance at $t \cong 16$ s.

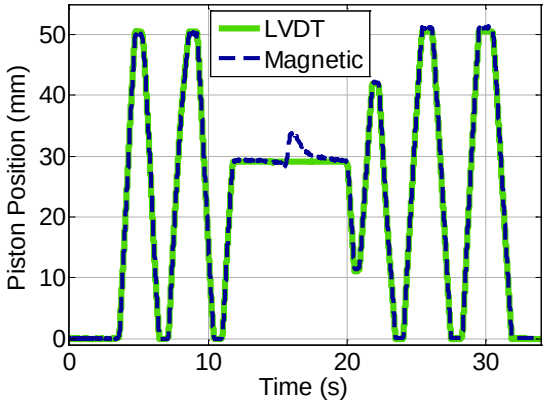


Figure 3-30. Piston position measured by the LVDT and estimated from the magnetic sensors measurements.

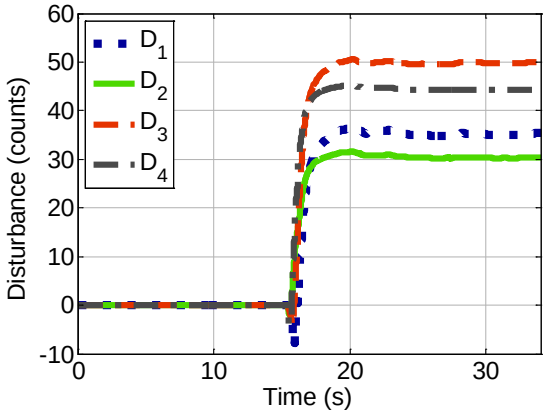


Figure 3-31. Estimated disturbance on each sensor.

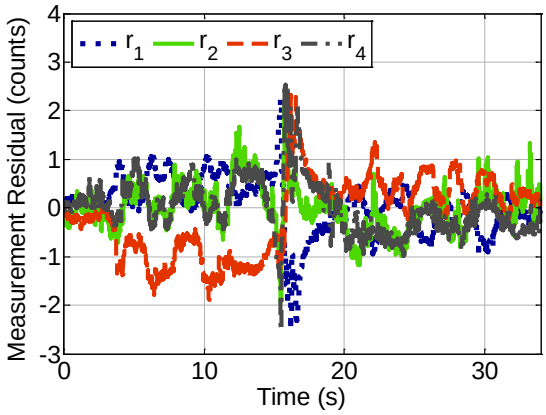


Figure 3-32. Filtered measurement Residuals over time.

In order to investigate how fast the sensing system recovers from an external disturbance, another experiment was conducted. A coil was placed next to the sensors and a step current was sent through the wirings of the coil to create a step magnetic field disturbance on the sensors. The step disturbances have a $10\% - 90\%$ rise time of 25 ms. Figure 3-33 shows the measured magnetic field from the four sensors. A step current is sent through the coil at $t \cong 15$ s and removed at $t \cong 46$ s. Figure 3-34 shows piston position measured by the LVDT and estimated from the magnetic sensors. The error of the position estimation system is shown in Figure 3-35. It can be seen that due to the generation and removal of the external disturbance, the error increases at $t \cong 15$ s and $t \cong 40$ s but drops very quickly (within 47 ms) below 1 mm. Figure 3-36 shows the estimated disturbance on each sensor.

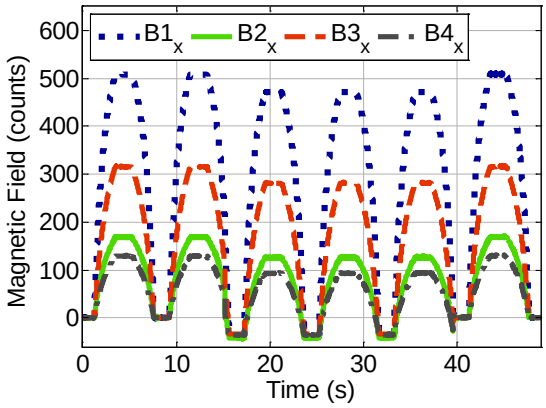


Figure 3-33. Experiment II – Magnetic field readings of the magnetic sensors which get affected by the external disturbance.

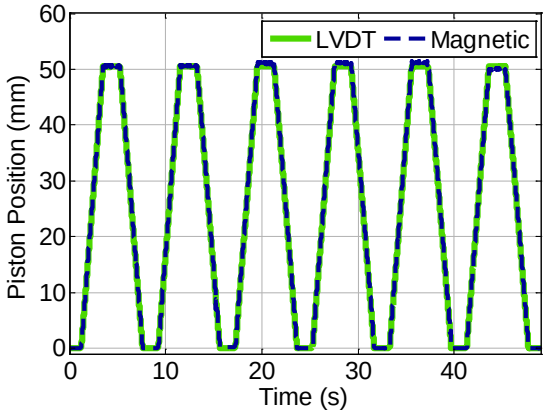


Figure 3-34. Experiment II – Piston position measured by the LVDT and estimated from the magnetic sensors measurements.

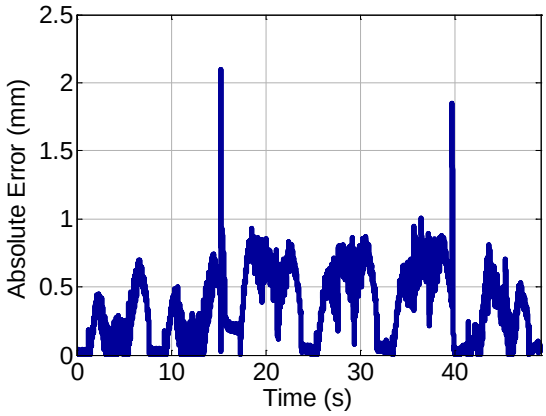


Figure 3-35. Experiment II – Error in position estimation.

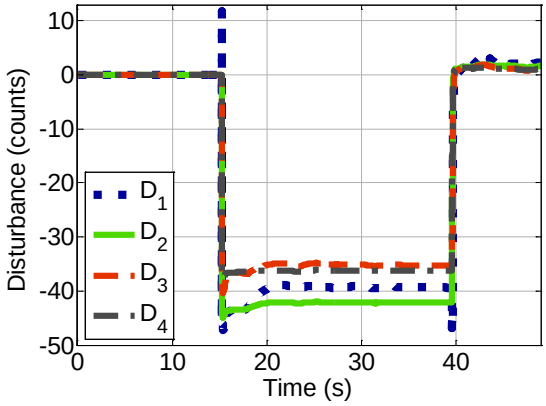


Figure 3-36. Experiment II – Estimated disturbance on each sensor.

In general, the time it takes for the estimated disturbances to converge to the actual disturbances determines how fast the sensing system can recover from an external disturbance. This time depends on several factors including the motion of the piston. The key factors in estimation of the disturbances on each sensor are the usage of the magnetic field model of the piston and the assumed constraint between the disturbances expressed by (3-66). Therefore, when an external object disturbs the sensors readings, if the piston is moving, more data points would be obtained and convergence time would be faster compared with the case when the piston is stationary.

### 3.5.4. Summary of the Disturbance Rejection Algorithm

The disturbance rejection algorithm described in Section 3.5.2 can be generalized and be used with different numbers and configurations of sensors. In this section, we provide a summary of the disturbance rejection method as a guideline:

1. Place a desired number of sensors $N \geq 2$ close to the object which its position is to be estimated. In the ideal case with no disturbance on the sensors, we have

$$Bi = f_i(x_p, \lambda) \qquad i = 1, 2, \dots, N, \tag{3-81}$$

   where $x_p$ is the piston position, $\lambda$ is a vector of magnetic field model parameters, and $B$ is the measured magnetic field.
2. Identify the model parameters, $\lambda_i$'s, using the method described in Section 3.4.
3. In general, the sensors measurement equations can be written as

$$Bi = f_i(x_p, \lambda) + D_i \qquad i = 1, 2, \dots, N, \tag{3-82}$$

   where $D_i$'s model the disturbance on each sensor caused by an external object. Use the geometry and the location of the sensors to impose $M \geq 1$ constraint on the disturbances as

$$c_j(D) = 0 \qquad j = 1, 2, \dots, M. \tag{3-83}$$

   Equation (3-66) is an example of such constraints. Two other examples are provided later in this section and in Section 3.5.5.
4. Develop an estimator (such as EKF) using the measurement equations and the constraints to estimate both the piston position and disturbances.

The number of sensors $N$ and the arrangement of the sensors depend on the specific application and the type of disturbances expected to occur. As an example, consider piston position measurement in a mobile vehicle using the proposed method where

disturbances occur due to the motion and rotation of the mobile vehicle in the Earth's magnetic field. In this case, if the sensors are close to each other, we can assume that they are affected equally by the Earth magnetic field. Therefore, we can write the constraint on the disturbances simply as

$$c(D) = D_1 - D_2 = 0. \tag{3-84}$$

As a result, two magnetic sensors are adequate for robust piston position estimation. As another example, consider the sensor configuration used in Section 3.5.2. If we also measure the magnetic field along the $Y$-axis of the sensors, we can have two sets of constraints:

$$\begin{cases} c_1(D_x) = D_{x1} - D_{x2} - D_{x3} + D_{x4} = 0, \\ c_2(D_y) = D_{y1} - D_{y2} - D_{y3} + D_{y4} = 0. \end{cases} \tag{3-85}$$

where $D_{xi}$'s and $D_{yi}$'s are the disturbances on each sensors $X$-axis and $Y$-axis readings. Similarly, we can apply a constraint on the magnitude of the disturbances as

$$\begin{aligned} c(D) = \left(D_{x1}^2 + D_{y1}^2\right)^{0.5} - \left(D_{x2}^2 + D_{y2}^2\right)^{0.5} - \left(D_{x3}^2 + D_{y3}^2\right)^{0.5} \\ + \left(D_{x4}^2 + D_{y4}^2\right)^{0.5} = 0. \end{aligned} \tag{3-86}$$

In the next section, we briefly present another example for the disturbance rejection method.

### 3.5.5. Robust Piston Position Estimation with Three Longitudinally Spaced Sensors

In this section, we present another example of the disturbance rejection algorithm where three magnetic sensors are placed longitudinally along the axis of the motion of the pneumatic cylinder as shown in Figure 3-37.

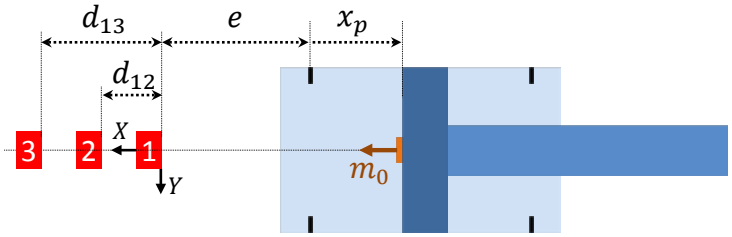


Figure 3-37. Sensor configuration for disturbance rejection algorithm using three longitudinally spaced sensors.

Following the steps described in Section 3.5.4, we write the measurement equations as

$$\begin{cases} B1_{xf} = \dfrac{p}{\left(x_{pf}+e\right)^3} - \dfrac{p}{\left(x_{p0}+e\right)^3}, \\ B2_{xf} = \dfrac{p}{\left(x_{pf}+e+d_{12}\right)^3} - \dfrac{p}{\left(x_{p0}+e+d_{12}\right)^3}, \\ B3_{xf} = \dfrac{p}{\left(x_{pf}+e+d_{13}\right)^3} - \dfrac{p}{\left(x_{p0}+e+d_{13}\right)^3}, \end{cases} \tag{3-87}$$

where $d_{12}$ is the distance between sensors 1 and 2, and $d_{13}$ is the distance between sensors 1 and 3. Next, we apply the method described in Section 3.4 to identify model parameters. As a constraint on the disturbances, we assume that we can fit a line to the disturbances on the sensors. A line in 2-D plane can be expressed as

$$y = \rho_1 x + \rho_2, \tag{3-88}$$

where $\rho_i$'s are the line parameters. Considering a line in 2-D plane passing through the two points $(d_{12}, D_2)$ and $(d_{13}, D_3)$ we have

$$\begin{cases} D_2 = \rho_1 d_{12} + \rho_2 \\ D_3 = \rho_1 d_{13} + \rho_2 \end{cases} \Rightarrow \begin{cases} \rho_1 = (D_3 - D_2)/(d_{13} - d_{12}), \\ \rho_2 = (D_2 d_{13} - D_3 d_{12})/(d_{13} - d_{12}). \end{cases} \tag{3-89}$$

Assuming that the point $(0, D_1)$ is on the same line and $d_{13} = 2d_{12}$, we get the following constraint on the disturbances:

$$c(D) = D_1 - 2D_2 + D_3 = 0. \tag{3-90}$$

Finally, we use the EKF to estimate both the piston position as well as the disturbances on the sensors. Figures 3-38 to 3-41 show the experimental results from this sensor system where an external disturbance was created by placing a wrench close to the sensors. As seen from Figures 3-39 and 3-41, the disturbance is partially estimated and corrected for as it is caused by the wrench. However, as the piston starts its motion, the estimated disturbances converge to the true disturbances and the estimation error reduces. Also, Figure 3-40 shows that disturbance rejection algorithm provides a great advantage compared with a sensing system without disturbance rejection where errors of up to 20 mm are observed.

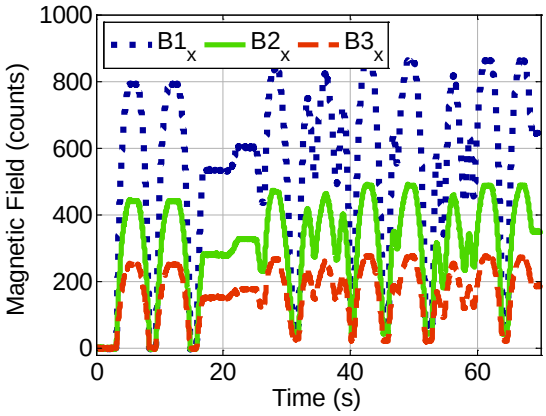


Figure 3-38. Magnetic field readings of the magnetic sensors which get affected by the external disturbance.

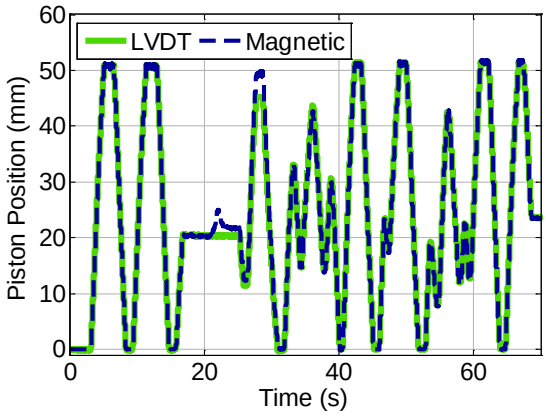


Figure 3-39. Piston position measured by the LVDT and estimated from the magnetic sensors measurements.

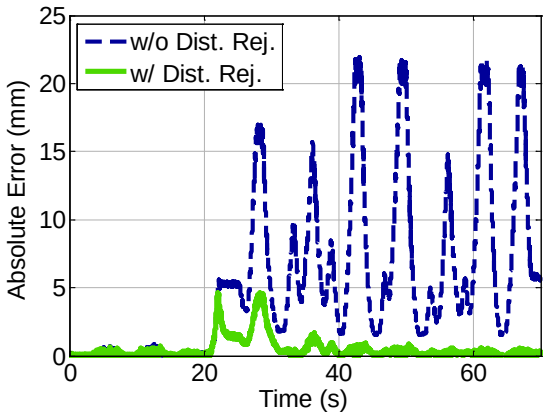


Figure 3-40. Error in position estimation with and without applying the disturbance rejection method.

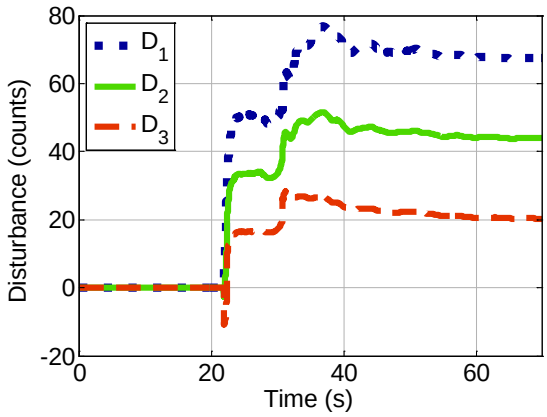


Figure 3-41. Estimated disturbance on each sensor.

## 3.6. Comparison of the Developed Sensing Technology with Existing Technologies

In the previous sections of this chapter, the developed sensor system for piston position estimation and its features were discussed. The developed technology has a great potential for commercialization because of the broad range of applications that it can be applied to and due to its advantages over existing technologies. In this section, a brief comparison between the developed sensor technology and existing technologies is provided. Note that the existing technologies considered are only the ones that are able to provide continuous linear position measurement. Table 3-2 shows comparison of the key features between the developed sensor and existing sensors. Price is included as a number between 1 and 5, with 1 indicating a price around or below $100 and 5 indicating a price around or above $1000, for a single unit of each sensor.

Table 3-2. Comparison of existing continuous linear position measurement sensors with the developed sensor discussed in this chapter.

| **Technology** / **Model** | **Linearity (% FS)** | **Contact Required** | **Line of Sight Required** | **Size Proportional to Measuring Range** | **Price** |
|---|---|---|---|---|---|
| Potentiometer LCP12Y-50 | 0.7 | Y | N | Y | 2 |
| LVDT LD620-25 | 0.2 | Y | N | Y | 4 |
| LVDT DC-SE 4000 | 0.25 | Y | N | Y | 3 |
| Laser FT80RLA-500-L8 | 0.375 | N | Y | N | 5 |
| Laser OD2-P300W200I0 | 0.3125 | N | Y | N | 5 |
| Ultrasonic T30UXUA | 0.25 | N | Y | N | 2 |
| Ultrasonic PK 104101-10 | 0.3 | N | Y | N | 3 |
| Magnetic SPS-L075-HALS | 0.4 | N | N | Y | 2 |
| Magnetic Univ. of Minn. | 0.8 | N | N | N | 1 |

In summary, potentiometers and LVDTs require mechanical connection between the moving object and the sensor. Therefore, it is not possible to use these sensors in a case where the moving object is isolated in a harsh environment, for example a piston moving inside an engine cylinder or a piston in a hydraulic cylinder operating by high-pressure fluid. On the other hand, making the mechanical connection requires modifications to the designed system which adds to the total cost of the measurement system. Another limitation of these types of sensors is that the size of the sensor increases as the range of

measurement increases. In other words, if the length of a sensor with measuring range of $d_1$ is $L$, the length of the same type of sensor with a measuring range of $d_1 + d_2$ should be at least $L + d_2$. This is a practical limitation; for example if it is desired to measure the position of a hydraulic piston whose range of motion is 500 mm, the length of the sensor should be at least 500 mm.

Laser and ultrasonic sensors do not require mechanical connection; however, they require a clear line of sight to the moving object. Therefore, their application becomes limited in cases where the moving object is isolated. Another requirement of the laser sensor is that the surface of the moving object should reflect a certain percentage of the laser beam. Laser sensors also have the highest price among the discussed position sensors.

The other magnetic based sensor in Table 3-2 (SPS-L075-HALS and similar models) requires installation of an extra magnet on the moving object. The sensor consists of an array of AMR devices which is placed adjacent to the moving object. The required short gap, 0.5 mm to 5.5 mm, between the sensor and the moving object limits the applicability of the sensor in cases that a thicker isolation of the moving object is required. Another major drawback is that the size of the sensor increases with the increase in the range of measurement of the sensor, similar to the potentiometer and the LVDT. Beside these limitations, magnetic disturbances caused by external ferromagnetic objects coming close to this sensor can affect the accuracy of the position measurement as noted in the sensor datasheet. However, the sensor technology developed in this chapter includes a disturbance rejection method which can guarantee robust and reliable position measurement in spite of magnetic disturbances.

Overall, the sensor technology developed in this chapter results in a non-contact, compact, inexpensive, robust, and accurate piston position estimation system which can be used for many position measurement applications. Figure 3-42 shows a developed USB-powered printed circuit board implementing this sensor technology.

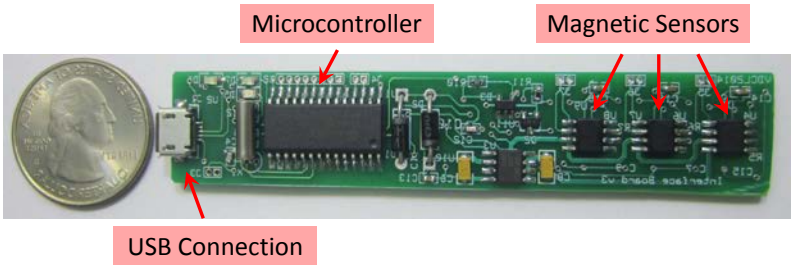


Figure 3-42. The prototype printed circuit board which includes a microcontroller and 3 magnetic sensors.

## 3.7. Conclusion and Future Work

In this chapter, a novel sensor technology was described for non-intrusive real-time estimation of piston position inside a cylinder. The developed sensor utilized external magnetic field measurements and did not require sensor placement inside the cylinder. By modeling the magnetic characteristics of a piston, a model of the magnetic field as a function of longitudinal position can be obtained. Using magnetic field sensors, the piston position can be obtained from the magnetic field measurements.

While the functional form will remain the same for objects of the same shape and size, the parameters in the function can vary from one object to another due to the varying levels of magnetization. Therefore, calibration for each individual object is needed which could be extremely time consuming both for instrumentation of the system with reference calibration sensors and for the actual data gathering and calibration process. This challenge was addressed by utilizing two magnetic sensors with known longitudinal separation between them. By using a redundant magnetic sensor, the need to use an additional position sensor (such as an LVDT) for calibration was eliminated. Experimental results from a free piston engine test rig and a pneumatic actuator test rig showed that the proposed sensor can provide 0.4 mm accuracy. The proposed sensing principle can be utilized for piston position measurement in multi-cylinder spark-ignition

and diesel engines, hydraulic cylinders, pneumatic cylinders, and in many other position measurement applications.

Another challenge with the use of magnetic sensors is the effect of other ferromagnetic objects moving close to the sensors. If this effect is not corrected for, piston position estimates can become inaccurate. A method was developed in this chapter to estimate the disturbance on each sensor caused by external objects. It was shown through experimental results that the developed method can significantly reduce the effect of external magnetic fields.

Due to the advantages of the developed technology over existing technologies as mentioned in Section 3.6, there is a potential for commercialization of the developed technology. Therefore, future work of this project includes taking steps to move towards a final product, such as packaging, failure mode and effects analysis (FMEA), and conducting extensive field trials.

It should be noted that the University of Minnesota has filed Provisional and PCT applications on this developed technology in March 2013 and March 2014, respectively.

# 4. Portable Roadside Sensors for Vehicle Counting, Classification, and Speed Measurement

## 4.1. Introduction

In this chapter, a portable sensing system is described that can be placed adjacent to a road and be used for vehicle counting, classification, speed measurement. The proposed system can make these traffic measurements reliably for traffic in the lane adjacent to the sensors. The developed signal processing algorithms enable the sensing system to be robust to the presence of traffic in the other lanes of the road.

The sensor consists of anisotropic magnetoresistive (AMR) devices that measure magnetic field. Signal processing algorithms based on an analysis of the magnetic field around a car are used to enable the sensor estimates. The developed sensor system is compact, portable, wireless, and inexpensive (with an expected cost on the order of $50).

Inductive loop detectors (ILD's) are a widespread technology used by many transportation agencies for vehicle detection and measurement of traffic flow rates. Single inductive loops by themselves do not measure individual vehicle speed.

Vehicle classification into pre-defined classes, such as cars, trucks, tractor trailers, etc., typically requires measuring the size/length of the vehicle and/or counting the number of axles of the vehicle. A vehicle classification model based on feature extraction

from piecewise slope rate values in single-loop inductive signature data was pursued in [73] and was able to classify vehicles into 15 classes. However, the accuracy rate is not 100% and can vary from $40\% - 100\%$ depending on the amount of "problematic" data present in the sensor readings and the class of vehicle under consideration.

Vehicle detection and classification based on feature extraction from camera systems have been developed by many researchers [74, 75]. The research in [75] presented model-based and fuzzy logic approaches to improve the reliability of such systems. An evaluation of three commercial camera based vehicle detection systems is presented in [76] under adverse weather conditions of snow, fog and rain. The results therein show that the performance of such systems deteriorates under adverse weather, especially under snow conditions in both daytime and nighttime. Increases in false calls by up to 90% and in missed calls by up to 50% were shown to occur in adverse weather.

Magnetic sensors and anisotropic magneto-resistive (AMR) sensors have also been evaluated for vehicle classification by some research groups [29, 51, 77-81]. The main limitation of these works is their inability to distinguish between sedans vs. sport utility vehicles (SUVs), pickups and vans. Mostly these two classes are combined, or poor classification rates are obtained when they are considered as individual classes. Further, the magnetic sensors that have been evaluated are based on devices embedded directly in the roadway lanes.

Unlike inductive loops and magnetic sensors that have been previously evaluated, the sensing system proposed in this paper does not require devices to be embedded in the roadway. Instead, it utilizes sensors that are placed on the side of the road and thus it is not needed to stop the traffic for their installation. Also, the sensor system used is very compact, wireless, and can provide very high accuracies in vehicle detection, classification, and speed measurement.

This chapter is organized as follows: In Section 4.2, the signal strength and sensor system configuration is discussed. In Section 4.3, the detection performance of the sensor

system is presented. The method developed to make the system robust to traffic in the nonadjacent lane is described in Section 4.4. In Section 4.5, the speed estimation method is described. Vehicle classification is discussed in Section 04.6. A method for counting the number of vehicles making a right turn at an intersection is discussed in Section 4.7. Conclusion and future work are presented in Section 4.8.

## 4.2. Signal Strength and Sensing System Configuration

An AMR sensor has a silicon chip with a thick coating of piezoresistive nickel-iron. The presence of an automobile in close range causes a change in magnetic field which changes the resistance of the nickel-iron layer. The HMC2003 3-axis magnetic sensor boards from Honeywell are utilized for the sensing system. Each sensor board contains core HMC100x AMR sensing chips which cost about $10.

First, magnetic field readings obtained from a magnetic sensor embedded on top of the road surface in the center of a lane were compared with the magnetic field readings when the sensor was placed adjacent to the road. Figure 4-1a shows the magnetic field readings of $X$-, $Y$-, and $Z$-axes with the sensor placed in the center of the road lane. Here, the $X$-axis is along the longitudinal direction of travel of the vehicles, $Y$-axis is perpendicular to the direction of travel of the vehicles and $Z$-axis is perpendicular to the road surface and upward. Figure 4-1b shows magnetic field readings when the magnetic sensor was placed adjacent to the road at a height of about 0.6 m. It can be clearly seen that the magnetic field readings due to the vehicle are 10 times stronger when the sensor was placed on the road. The vehicle used for these two tests was a Ford Ranger pickup truck.

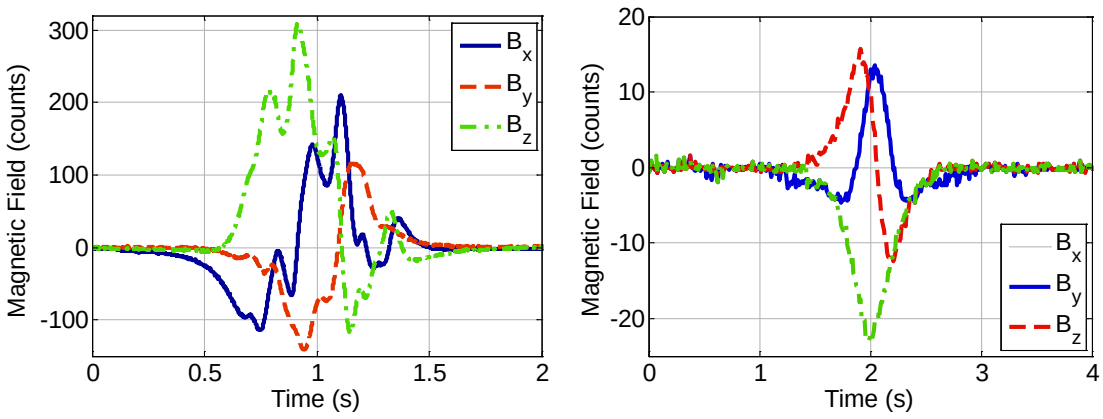


Figure 4-1. Magnetic field readings of a Ford Ranger vehicle. (a) Magnetic sensor embedded in the road. (b) Magnetic sensor adjacent to the road.

It can be also seen from Figure 4-1b that when the sensor is placed on the side of the road, the signals are more uniform compared with the case where the sensor is on the road. The main reason is that with the sensor on the road, many different ferromagnetic parts underneath the vehicle pass over the sensor at close proximity and create extra fluctuations in the signals. Since the original signal levels are low when the sensors are placed on the side of the road, it is necessary to use higher amplification in order to get better signal-to-noise ratio. Therefore, the sensors signals were amplified using instrumentation amplifiers with cut-off frequencies set to 100 Hz to reduce the noise level.

Figure 4-2 shows the configuration of the sensor system which includes four 3-axis magnetic sensors placed on the side of the road. The objective of the system is to count, measure the speed, and classify the vehicles that pass in the adjacent lane. Sensors 1 and 2 are laterally spaced from each other by 0.1 m. Sensor 3 is placed 0.9 m longitudinally downstream from sensor 1. Sensor 4 is placed 0.3 m vertically above sensor 1. Sensors 1 and 2 are together used to obtain a rough estimate of lateral location of the vehicle and make the sensing system robust to the traffic in the nonadjacent lane. This method is described in Section 4.4. Sensors 1 and 3 are together used to calculate the longitudinal

speed of passing vehicles. The speed estimation algorithm is described in Section 4.5. Sensor 4 is used along with sensor 1 to get a rough estimate of the average vertical magnetic height of passing vehicles which is used for vehicle classification described in Section 4.6.

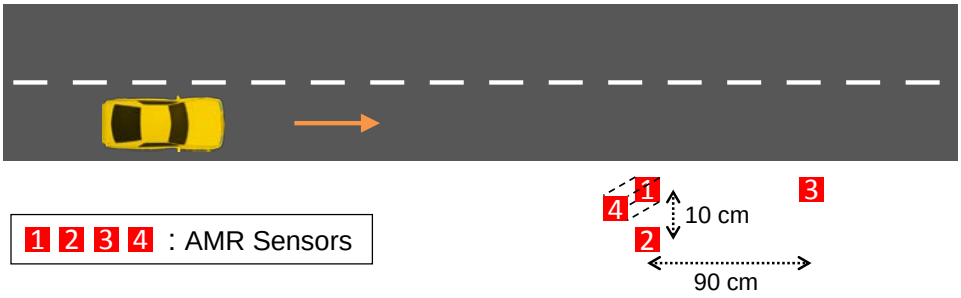


Figure 4-2. Sensor configuration for data collection.

A single printed circuit board (PCB) contains sensors 1 and 2. Two other PCB's contain Sensors 3 and 4. The PCB's include Microchip dsPIC microcontrollers which sample the sensors output at 1 KHz with 12-bit Analogue-Digital-Converters (ADC). Magnetic field is read in as arbitrary voltage unit (counts) as provided by the ADCs. The data is transferred from the PCB's to a laptop either wirelessly or through a serial port. The XBee wireless module from Digi® is used for wireless communication. This module has an outdoor line-of-sight range of 100 m, required power of 150 mW and radio frequency (RF) data rate of 250 kbps. Figure 2-4 shows the developed PCB.

## 4.3. Vehicle Detection and Counting

As it was mentioned in the previous section, the recorded signals from the sensors placed adjacent to the road are more uniform compared with the case where the sensors are on the road. This behavior makes the detection more reliable since many oscillations in the signals can cause errors due to double detection of a single vehicle. Specifically, it was observed that the signals measured along the $Z$-axis have very similar patterns for a

large variety of vehicles. Therefore, magnetic readings of the $Z$-axis of sensor 1 are used for detecting and counting the passing vehicles in the adjacent lane. A threshold of 30 counts was used as the vehicle detection threshold. This threshold was selected experimentally. If it is set too high, smaller vehicles will not be detected and if it is set too low, a higher percentage of vehicles passing in the nonadjacent lane will be detected. Although a robust algorithm is developed for reducing the false detections due to vehicles passing in the nonadjacent lane (described in Section 4.4), it is good to avoid false detections at an early stage to have a minimized final false detection rate. Signals from 188 vehicles driving in the adjacent lane were recorded in two days during afternoon hours under clear sky condition. Out of the 188 vehicles, 186 vehicles created a large enough signal to be detected resulting in a detection rate of 99%. Figure 4-3 shows a sample signal recorded from a Jeep SUV passing in the adjacent lane, two unknown vehicles passing in the nonadjacent lane, and a Mazda sedan passing in the adjacent lane at lateral distances of 2 m, 5.3 m, 4.6 m, and 1.6 m from the sensors, respectively. The lateral distance was measured purely for reference purposes by a sonar sensor facing the road.

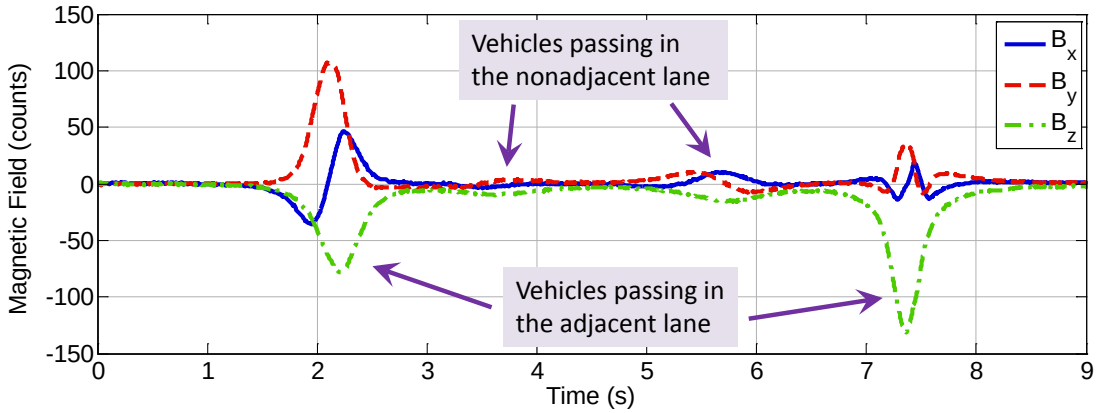


Figure 4-3. Recorded magnetic field from a Jeep SUV and a Mazda Sedan passing in the adjacent lane and two other vehicles passing in the nonadjacent lane.

## 4.4. Robustness to Traffic on the Nonadjacent Lane

While measuring traffic parameters on the lane adjacent to the sensors, the signals from over 216 vehicles passing in the nonadjacent lane (the lane next to the closest lane to the sensors) were also recorded. Analyzing the data, it was observed that passenger sedans, SUVs, and pickups traveling in the nonadjacent lane typically do not create errors in the sensor system signals. However, larger vehicles (trucks, buses, etc.) passing in the nonadjacent lane may create large enough signals to cause false detections and affect the accuracy of the system. The false detections can significantly increase the detection error. In our experiments, 15 vehicles out of 216 vehicles created a large enough signal to be miscounted as a vehicle passing in the adjacent lane. If uncorrected, this will cause an overdetection error of 8%. The results presented in [82] show a similar error rate from false detection of vehicles in the adjacent lanes ranging from 5.6% to 15.4% in different weather conditions, even when the AMR sensors are embedded in the middle of the lane in the road. It should be noted that increasing the detection threshold is not an effective solution to address this problem. Although it may reduce the number of false calls, it will increase the number of missed calls due to smaller vehicles not being detected because of the higher threshold as experienced in [83]. In order to correct for vehicle detection errors due to larger vehicles passing in the nonadjacent lane, a method is developed which is described in the following paragraphs.

Through analytical modeling and experimental measurements, it was shown in Chapter 2 that the magnetic field intensity around a vehicle has a relation that approximately varies as $1/x$ with distance, where $x$ is the distance from the vehicle. An estimate of the lateral distance of a vehicle can be obtained by simply evaluating the ratio of the maximum of the measured magnetic fields between Sensors 2 and 1, $B_2/B_1$. As the distance $x$ increases, the two sensors read roughly the same magnetic field intensity. The closer the ratio of magnetic fields is to 1, the larger is the lateral distance. Also, the

vehicles passing in the nonadjacent lane have a much lower peak value, $B_{max}$, on average compared with vehicles passing in the adjacent lane. These two metrics can be used to reject the traffic passing in the nonadjacent lane affecting the sensors. Figure 4-4 shows the result of applying the proposed method to the dataset. A support vector machine is used to come up with a classification boundary [84]. Using the developed method, the error reduces from 8% to 1%. From the data of 216 vehicles shown in Figure 4-4, it can be seen that the proposed classification boundary accurately classifies 99% of the vehicles as correctly being in the adjacent or nonadjacent lane. All of the nonadjacent vehicles are correctly rejected. Only two of the 201 adjacent lane vehicles are incorrectly classified as nonadjacent.

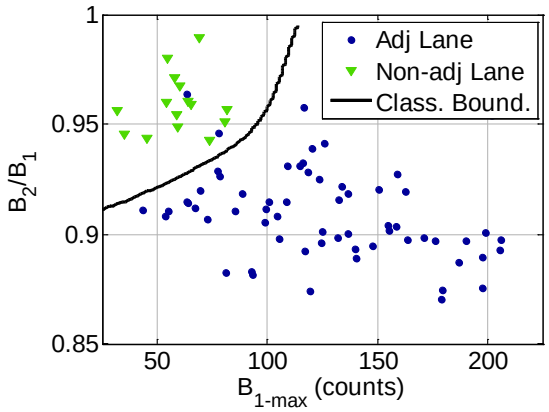


Figure 4-4. Use of the ratio $B_2/B_1$ and $B_{1-max}$ to reject the traffic in the nonadjacent lane.

## 4.5. Speed Estimation

Estimating the speed of a passing vehicle is required in order to measure vehicle length which is used for vehicle classification. Speed estimation also has other applications, for example, it has been used by researchers to estimate the queue length for ramp metering algorithms [85]. Transportation agencies use estimated speed information for setting speed limits and timing traffic signals [86]. There are some proposed methods

in the literature for speed measurement using a single magnetic sensor [29]; however, those methods provide only an average estimate of the speed over a number of passing vehicles. In order to measure individual vehicle speed, two longitudinally spaced sensors are required. The conventional method for estimating speed with two magnetic sensors is based on the detection times of the two sensors. If the detection times for sensors "a" and "b" are $t_{a,ON}$, $t_{a,OFF}$, $t_{b,ON}$, and $t_{b,OFF}$, an estimate of the speed can be calculated as

$$v = \frac{d_{a-b}}{\left(\left(t_{b,ON} - t_{a,ON}\right) + \left(t_{b,OFF} - t_{a,OFF}\right)\right)/2}, \tag{4-1}$$

where $d_{a-b}$ is the distance between sensors "a" and "b". $t_{a,ON}$ and $t_{b,ON}$ are the time stamps that the sensor signal goes over the detection threshold, for sensors "a" and "b", respectively. $t_{a,OFF}$ and $t_{b,OFF}$ are the time stamps that the sensor signal drops below the detection threshold, for sensors "a" and "b", respectively. One of the primary factors that affect the accuracy of the speed estimates is the distance between the sensors; more accurate estimates are obtained by placing sensors further away from each other. For example [87] recommends a separation of 4.9 m between two inductive loops used for speed estimation. As another example, [88] recommends a separation of $3.1 - 3.7$ m ($10 - 12$ feet) between the sensors for arterial applications and $6.1 - 7.3$ m ($20 - 24$ feet) for freeway applications. However, none of the above references specify or evaluate the accuracy of the estimates. On the other hand, the problem with a large distance between the sensors is that a vehicle may perform a maneuver which may only be detected by one sensor [86]. This phenomenon will affect the synchronization between the sensors which is required for speed estimation. It is worth mentioning that another factor in accuracy of the estimated speed is the Signal-to-Noise Ratio (SNR); the higher the SNR, the more accurate the estimates. As it was mentioned in Section 4.2, lower-level signals are obtained when placing the sensors on the side of the road compared with the case that the sensors are placed on the surface of the road, in middle of the lane and thus, the sensors outputs are amplified to get higher SNR.

In [86], a method for speed estimation is proposed based on signals from two ILDs separated by a distance of 6 m using detection times. Their method detects and drops the data points from "irregular driving vehicles" defined as vehicles that do not travel perfectly in parallel with the line connecting the center of the sensors. After dropping these data points, the maximum absolute value of the error is within 5%. However, in their experiments, over 8% of the detected vehicles were categorized as "irregular driving vehicles" and thus, their speed was not estimated. This situation is not favorable for vehicle classification based on the magnetic length of passing vehicles.

In [89], a method for speed estimation is proposed which is based on using three magnetic sensor. The accuracy of the method is measured by driving a vehicle at one constant speed of $5.5\ \mathrm{m/s}$ $(12\ \mathrm{mph})$ over the sensors multiple times. The reported estimation error varies in the range of 5% to 20% underestimating the actual speed in all cases.

In [90], another method for speed estimation is proposed which is based on using 4 magnetic sensors, two nodes are placed on one side and two nodes are placed on the other side of a one-lane road. The distance between the sensors on each side is 6 m. The results of speed estimation method show maximum errors of 13% with low test speeds ranging from $6 - 13\ \mathrm{m/s}$ $(13.4 - 29\ \mathrm{mph})$.

The goal of the proposed system in this section is to reduce the distance between the sensors to a minimum and still achieve highly accurate speed estimates by using sophisticated signal processing techniques to measure the time delay. In the designed system, the speed of each passing vehicle is determined by measuring the time delay between the signals of the two magnetic sensors placed longitudinally apart, sensors 1 and 3. The delay is calculated by taking the cross-correlation between the signals of the two sensors and then finding the time delay by looking at the value where the resulting signal from the cross-correlation is maximized. Knowing the time delay and the distance

between the two sensors, the speed of a passing vehicle is estimated. This algorithm is described in the following section.

### 4.5.1. Speed Estimation Algorithm

Consider the magnitude of the magnetic field signals from sensors 1 and 3, $B_{1mag}$ and $B_{3mag}$, respectively. We expect that $B_{3mag}$ will have the same shape as $B_{1mag}$ but be shifted in time since sensor 3 is longitudinally spaced apart from sensor 1, downstream with respect to the vehicle. Ideally, the delay in time between the signal waveforms will have the following relation with the speed of the passing vehicle $v$:

$$\delta t = \frac{d_{13}}{v}, \tag{4-2}$$

where $d_{13}$ is the distance between sensors 1 and 3, and $\delta t$ is the time delay between the signals of the sensors to be calculated. Denoting the sampling time by $T_s$, $B_{3mag}$ should be delayed by $n_d = \delta t / T_s$ samples with respect to $B_{1mag}$. A reliable method of calculating the time delay is to take the cross-correlation between the two signals. The time delay in terms of samples is given by

$$n_d = \arg\max_n f[n], \tag{4-3}$$

where

$$f[n] = \sum_{m=0}^{N-1} B_{1mag}[m] B_{3mag}[m-n] \quad \text{for} \quad -(N-1) \leq n \leq N-1, \tag{4-4}$$

and $N$ is the total number of samples for which the cross-correlation is being computed. This computation is in the order of $N^2$ calculations [91]. The Discrete Fourier Transform

(DFT) can be adopted to compute $f[n]$ which results in a significantly lower number of required calculations. The method is described in the following paragraphs.

Define

$$\begin{aligned} z_1[n] &= B_{1mag}[n] \qquad 0 \le n \le N-1, \\ z_2[n] &= B_{3mag}[(N-1)-n] \qquad 0 \le n \le N-1, \\ g[n] &= f[n-(N-1)] \qquad 0 \le n \le 2N-2. \end{aligned} \tag{4-5}$$

It can be seen that $z_2[n]$ is simply the flipped version of $B_{3mag}[n]$ and $g[n]$ is the shifted version of $f[n]$. Now, we rewrite (4-3) in terms of $g[n]$:

$$n_d = \arg\max_n f[n] = (\arg\max_n g[n]) - (N-1). \tag{4-6}$$

We can also write $g[n]$ as

$$\begin{aligned} g[n] = f[n-(N-1)] &= \sum_{m=0}^{N-1} B_{1mag}[m] B_{3mag}\big[m-\big(n-(N-1)\big)\big] \\ &= \sum_{m=0}^{N-1} B_{1mag}[m] B_{3mag}\big[m-\big(n-(N-1)\big)\big] \\ &= \sum_{m=0}^{N-1} z_1[m] z_2[n-m] = z_1[n] * z_2[n]. \end{aligned} \tag{4-7}$$

Therefore, we have written $g[n]$ in terms of linear convolution of $z_1[n]$ and $z_2[n]$. The next step is to calculate this convolution in an efficient way. From the properties of DFT [91, 92], we know that

$$x_3[n] = \sum_{m=0}^{N-1} x_1[m] x_2[(n-m)\ mod\ N] = x_1[n] \circledast x_2[n] \qquad \Leftrightarrow \tag{4-8}$$

$$X_3[k] = X_1[k]X_2[k] \qquad for \quad 0 \le n, k \le N-1,$$

where $\circledast$ denotes circular convolution and $X[k]$ is the DFT of $x[n]$:

$$X[k] = DFT(x[n]) = \sum_{m=0}^{N-1} x[m]e^{-j\left(\frac{2\pi kn}{N}\right)} \qquad for \quad 0 \le k \le N-1. \tag{4-9}$$

In general, the circular convolution differs from linear convolution. In circular convolution, the second sequence is "circularly" shifted with respect to the first sequence. However, we can use the relation in (4-8) to obtain $g[n]$ if we pad the original signals, $z_1[n]$ and $z_2[n]$, with zeros to a length equal or greater than the expected length of the linear convolution $(2N-1)$ [91, 92]. Thus, if we define:

$$\begin{aligned} \tilde{z}_1[n] &= \begin{cases} z_1[n] & 0 \le n \le N-1, \\ 0 & N \le n \le 2N-1, \end{cases} \\ \tilde{z}_2[n] &= \begin{cases} z_2[n] & 0 \le n \le N-1, \\ 0 & N \le n \le 2N-1, \end{cases} \end{aligned} \tag{4-10}$$

we have:

$$g[n] = IDFT\big(DFT(\tilde{z}_1[n]).DFT(\tilde{z}_2[n])\big). \tag{4-11}$$

Now that $g[n]$ is calculated, we can obtain $n_d$ from equation (4-6) and calculate speed from (4-2). It should be noted that using Fast Fourier Transform (FFT) and Inverse Fast Fourier Transform (IFFT) algorithms for calculation of DFT and IDFT, we can calculate $g[n]$ with computational complexity in the order of $NlogN$ compared with the original order of $N^2$ [91]. As an example, if we originally have $N = 10000$ datapoints (10 s of data sampled at 1 KHz), we will have orders of $10^8$ and $10^5$ for the original method and DFT method, respectively. This difference can be considerable when the system is implemented in a processor for real-time classification.

The main benefit of using the conventional method of finding the difference between the detection times to estimate the speed is its simplicity which allows for design of a sensor system with less complexity and reduced power consumption. These requirements are helpful in increasing the battery life of a sensor when the sensor is embedded into the pavement. However, with the sensors on the side of the road, the power can be provided by larger capacity batteries, power lines, solar cells, or a combination of these power sources. Therefore, it is possible to have more computational power available and develop much more accurate algorithms to achieve better performance in speed estimation and consequently, better performance in vehicle classification.

### 4.5.2. Speed Estimation Experimental Results

In order to check the speed estimation accuracy of the sensing system, the following experiment was conducted at MnROAD, Minnesota's Road Research Facility. The sensor system was placed adjacent to the lane as shown in Figure 4-1. A carrier phase GPS, Garmin® GPS18 LVC, was mounted on a test vehicle and its data was captured using a laptop inside the vehicle. The accuracy of the GPS speed measurement is $0.05\ \mathrm{m/s}$ and its update rate is $1\ \mathrm{Hz}$. A separate data acquisition system was used to capture the roadside sensor data similar to the previous experiments.

For each test, the driver started at a long distance away from the sensors, reached the desired speed, passed in front of the sensors with constant speed and later stopped. A sample of speed plot obtained from the GPS during one test is shown in Figure 4-5.

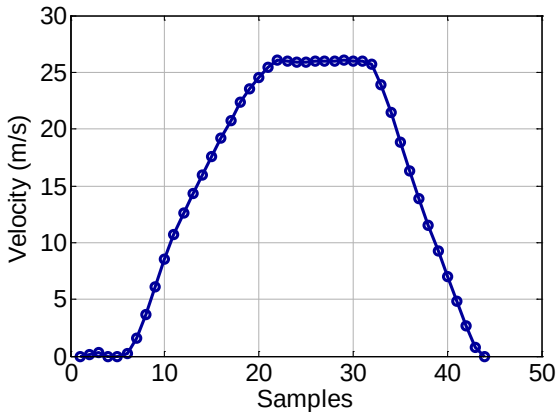


Figure 4-5. Sample GPS signal from the experiments of speed accuracy verification.

Since the speed is almost constant during the time that the vehicle passes in front of the sensors, it is possible to take the average of several data points before the vehicle decelerates and use it as the reference speed obtained from the GPS. In all the experiments, 11 satellites were in view for the GPS. The test vehicle was also equipped with cruise control system which was used for velocities above $\sim 13\ \mathrm{m/s}$ (30 mph) to achieve a more uniform speed.

The error in speed estimates can be calculated as

$$\text{Error} = 100\,\frac{v_{GPS} - v_{est}}{v_{GPS}}, \tag{4-12}$$

where $v_{GPS}$ is the reference GPS speed and $v_{est}$ is the estimated speed from the magnetic sensors.

Figure 4-6 shows the estimation error between the GPS measurement and the sensor estimates when the sensor-based speed was calculated using the simple difference in the detection times described by (4-1). As can be seen from Figure 4-6, the maximum error for speed estimation is more than 12%. As a result, the magnetic length estimates used for vehicle classification would have the same percentage error since speed estimation error directly propagates to magnetic length estimation error. Figure 4-6 also shows the estimation error when the cross-correlation method has been applied for speed estimation.

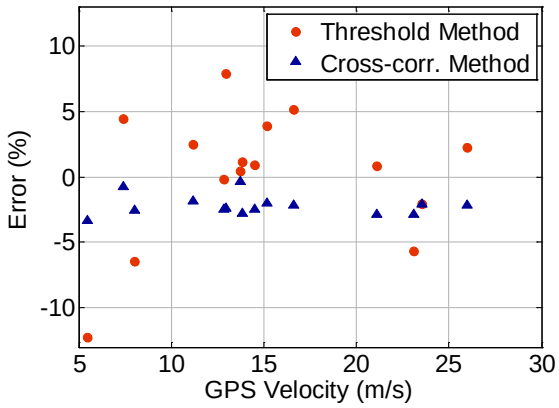


Figure 4-6. Speed estimation error from the conventional threshold method and the cross-correlation method.

As can be seen from the Figure 4-6, comparing the conventional and the cross-correlation based methods, the error range has been reduced from 12% to only 3.5%. Considering the errors of the proposed method, a negative offset is observed meaning that the estimated speed is overestimating the actual speed. This overestimation of speed can be due to the fact that the sensors are not perfectly aligned with the side of the road, as shown in Figure 4-7, which makes the actual measured distance between the sensors larger than the effective distance between the sensors.

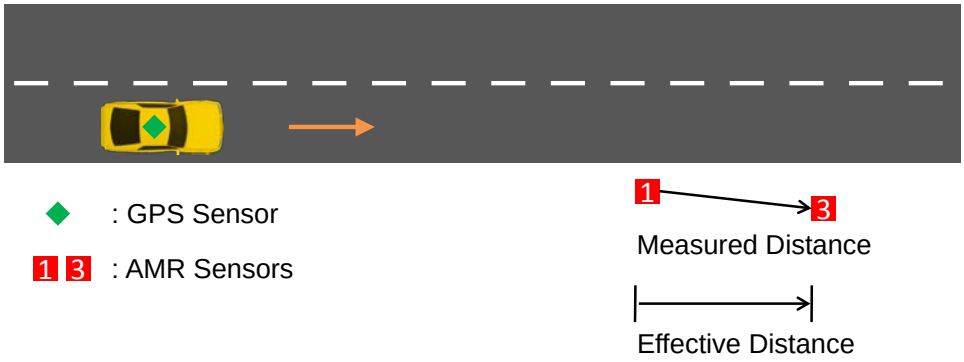


Figure 4-7. Sensor configuration for data collection and the fact that the sensors may not be perfectly aligned with the side of the road.

Multiplying the measured distance between the sensors in this test by a constant factor of 0.98, we get an almost zero-biased speed estimation error as shown in

Figure 4-8. In a general test where there is not a reference value for calibration, we can use the method described in the following paragraphs to automatically compensate for misalignment problem.

Assume that sensors 1 and 3 are perfectly aligned with the side of the road and a vehicle passes precisely parallel to the sensors. Therefore, the signals from sensors 1 and 3 should be exactly identical except for a delay which is used for speed estimation. Now assume that the sensors are not perfectly aligned. In this case, the signals of the two sensors will slightly be different. For example in the scenario depicted in Figure 4-7 where sensor 1 is closer to the road than sensor 3, we expect to see slightly higher signal levels for sensor 1 than sensor 3. We can use this difference and partially adjust for the misalignment. This method is based on using the ratio of integrated values of the 2 signals. Define

$$Bi_{int} = \int_{t_{i,1}}^{t_{i,2}} Bi\ dt \qquad i = 1,3, \tag{4-13}$$

where $t_{i,1}$ and $t_{i,2}$ are the detection times. Now defining

$$c = \min\left(\frac{B1_{int}}{B3_{int}}, \frac{B3_{int}}{B1_{int}}\right), \tag{4-14}$$

we modify $d_{13}$ as

$$d_{13-corrected} = c * d_{13}, \tag{4-15}$$

and estimate the speed as

$$v = \frac{d_{13-corrected}}{\delta t}, \tag{4-16}$$

where $\delta t$ is the time difference between the signals calculated earlier. The results from applying this method are shown in Figure 4-8. It can be seen that using this method we can get an almost zero-biased error (mean error is $-0.78\%$).

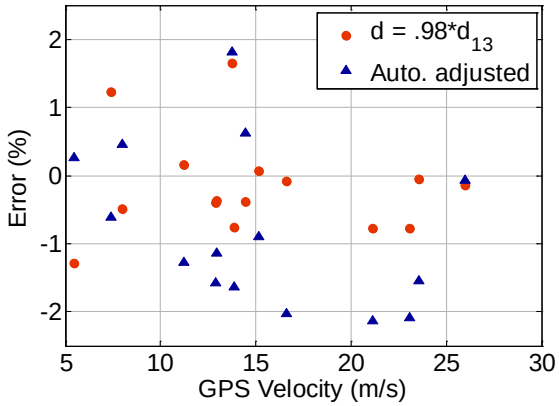


Figure 4-8. Speed estimation error in the cases where the offset is manually and automatically adjusted.

As seen from Figure 4-8, the maximum absolute error in speed estimation is less than 2.5% over the entire range of speeds, $5 - 27$ m/s ($11 - 60$ mph).

## 4.6. Vehicle Classification

Vehicle classification is useful in a number of applications, including road maintenance and management, roadway design, emissions evaluation, multimode traffic model development, traffic control, traffic signal design, and toll systems development. For example, the distribution of passing vehicles on a road is used in estimation of pavement life cycle [93]. There are different vehicle classification methods proposed in the literature based on inductive loops and vision systems. In general, the main drawbacks of using inductive loops are the high cost, the long installation process, and the intrusive nature of sensor installation. The main drawback of systems based on vision is the high sensitivity to weather conditions, as mentioned earlier in Section 4.1. The

benefit of using magnetic sensors for vehicle classification is that they are less expensive, more robust to weather conditions and easier installation process. In addition to these benefits, the sensing system proposed in this paper is portable and can be placed adjacent to the road, and thus, it is not necessary to stop the traffic.

There are existing methods in the literature for vehicle classification based on magnetic sensors. However, the main limitation of these methods is the poor performance in differentiating sedans vs. SUVs, pickups and vans and thus, these two classes are usually combined as in [79, 80] or only vans are classified as a separate class [78, 81, 94].

In [29], a vehicle classification method is proposed based on hill pattern of magnetic signatures obtained from a single magnetic sensor. Vehicles are classified into 7 classes including sedans, SUVs and vans. However, the classification rate that has been achieved is only 63%.

A classification method based on average bar and hill pattern recognition schemes is proposed in [95]. Vehicles are classified into four classes including sedans and SUVs/vans. About 95% of vehicles are classified correctly; however, the number of SUVs/vans in the dataset is only 5% of the total vehicles compared with the total number of sedans which is 84%.

The classification method proposed in this section is based on using the magnetic length and an estimate of the average vertical height of the passing vehicles. Vehicles are classified into 4 classes; Class I: sedans, Class II: SUVs, pickups and vans, Class III: Buses and 2-3 axle trucks, and Class IV: articulated buses and 4-6 axle trucks.

In Section 4.5, it was described how the speed of each passing vehicle is calculated. In addition, the time duration for which a passing vehicle's magnetic field stays above the detection threshold can be measured to calculate occupancy. The product of the vehicle's estimated speed and the occupancy provides the vehicle's magnetic length. A vehicle's magnetic length can be slightly different from its actual physical length. This is because

the vehicle magnetic field extends beyond its physical boundaries. However, the length can be calculated with sufficient accuracy for vehicle classification. Of the signals from three axes of the magnetic sensors, the magnetic signals along the $Z$-axis were observed to have a very consistent pattern for different types of vehicles. Therefore, magnetic readings of the $Z$-axis were used for measuring the magnetic length, and a threshold of 30 counts was selected for occupancy measurement. Examples of magnetic signatures are shown in Figures 4-9 to 4-12.

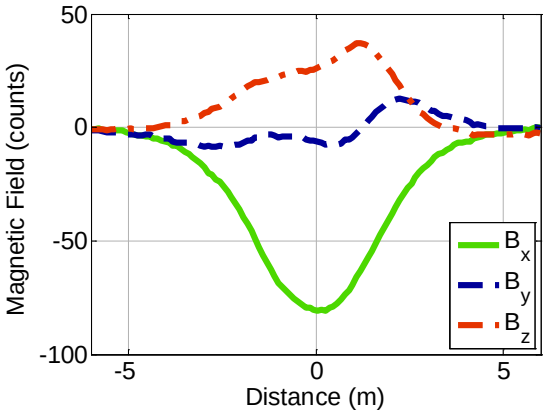


Figure 4-9. Magnetic signature of a Nissan Maxima (Class I) passing at 1.6 m from the sensors.

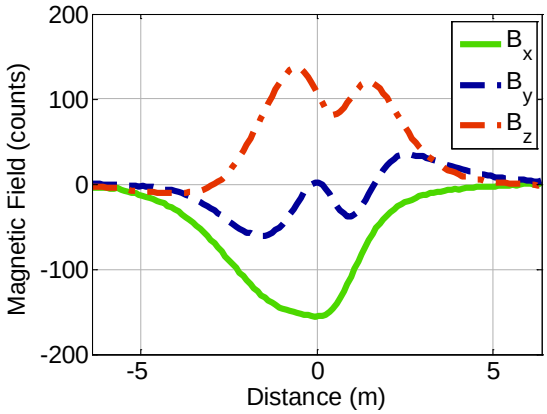


Figure 4-10. Magnetic signature of a Toyota Highlander SUV (Class II) passing at 1.4 m from the sensors.

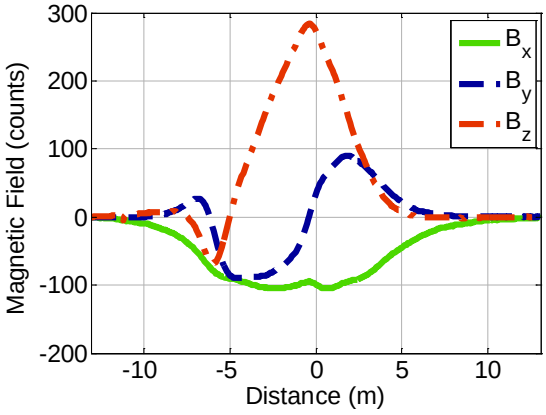


Figure 4-11. Magnetic signature of a Cement Truck (Class III) passing at 1.5 m from the sensors.

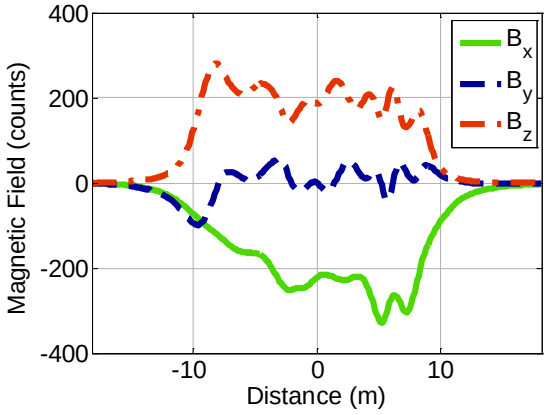


Figure 4-12. Magnetic signature of an articulated bus (Class IV) passing at 1.2 m from the sensors.

Figure 4-13 shows the measured magnetic length for various vehicles in the four classes. As seen from Figure 4-13, the magnetic lengths of vehicles in Classes III and IV are clearly distinguishable from those of vehicles in Classes I and II. As a result, by using only this single feature, it is possible to accurately classify vehicles in these two classes. This is expected since the actual lengths of the vehicles in Class I/II and vehicles in Class III and IV are very different. However, since vehicles in Class I and II have similar lengths and consequently similar magnetic lengths, it is not possible to classify them by only magnetic length. In order to improve the classification of vehicles between Classes I and II, another method is developed which is described in the following paragraphs.

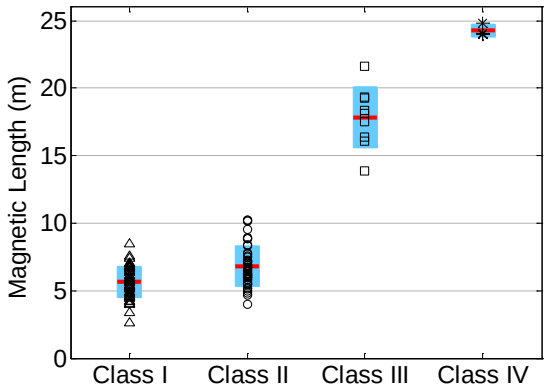


Figure 4-13. Magnetic length and classification for various types of vehicles.

It is expected that higher vertical locations of magnetic components in a vehicle in Class II leads to a higher magnetic height of these vehicles compared with vehicles in Class I. Placing another sensor, sensor 4, about 0.3 m vertically above sensor 1, it is expected that the ratio $B4_z/B1_z$ will be larger for vehicles in Class II. This ratio along with the magnetic length can be used to create more separable boundaries for the purpose of classification between vehicles in Classes I and II. The result is shown in Figure 4-14 where a support vector machine has been used to come up with a classification boundary [84]. Using these two features, 83% of the vehicles are correctly classified into Classes I and II. It is worth mentioning that the two features proposed for classification are very

easy to implement and are based on the physical magnetic properties of vehicles and not based on some heuristic features and methods like hill patterns or neural networks.

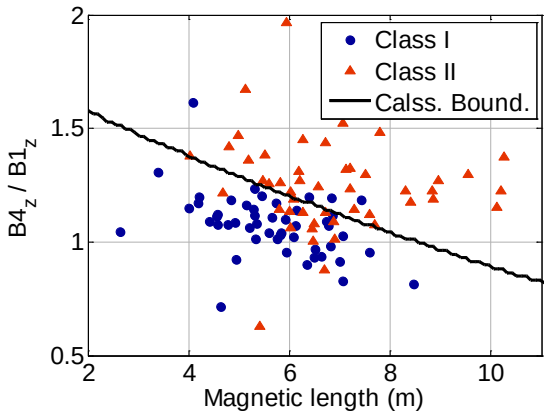


Figure 4-14. Classification of vehicles in Classes I and II.

## 4.7. Right-turn Detection

The objective of the system described in this section is to count the number of right turns vs. the number of straight-driving vehicles at a traffic intersection. This portable system can replace the current method which is based on manual counting. The number of right turns at an intersection is used for adjusting the traffic lights. The sensors are placed at an intersection as shown in Figure 4-15.

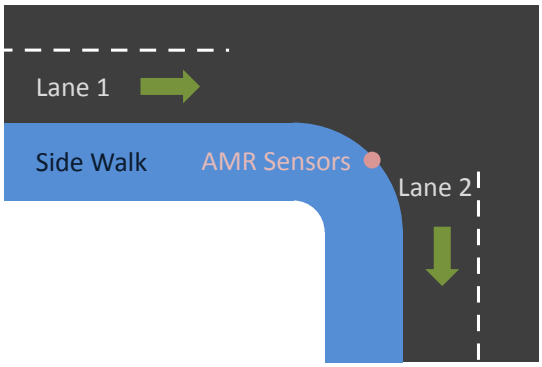


Figure 4-15. Right-turn detection and placement of the AMR sensors.

Our objective is to determine the percentage of the vehicles moving in Lane 1 and then making a right turn into Lane 2. Recall that for traffic measurement when vehicles are travelling in a straight line, the magnetic sensors could be placed on the side of road and vehicles should typically pass within a distance of 2.5 m from the sensors in order to be detected. However, when the sensors are placed at the corner of an intersection, half of the turning radius ($\sim 2-3$ m) is added to the lateral distance between the sensors and vehicles passing in Lanes 1 and 2. Thus, most of the vehicles passing straight in front of the sensors in Lanes 1 or 2 are not typically detected. The vehicles that are being detected are the vehicles making a right turn, or larger vehicles moving straight in Lane 1 or 2.

By placing one magnetic sensor at the corner side of the road as shown in Figure 4-15, the number of right turns at an intersection can be counted. During the experiments, 56 out of 59 right turns were counted correctly resulting in a detection rate of 95%. As it was mentioned earlier, typically straight-driving vehicles are not detected since they pass at a larger distance from the sensor compared with vehicles making a right turn. However, larger straight-driving vehicles can create large enough signals to be miscounted as vehicles making right turns. During the experiments, 18 straight-driving vehicles created large enough signals to be miscounted as vehicles making a right turn which results in an overdetection error of 31%.

Two methods, A and B, are proposed to identify and reject the false calls caused by straight-driving vehicles, using two and four magnetic sensors, respectively. Considering the sensor configuration shown in Figure 4-16, in method A, signals from magnetic Sensors 2 and 3 are used. In method B, signals from all the 4 magnetic sensors are used. The two methods are presented in the following sections. It should be mentioned that the sensor configuration used for right-turn detection, shown in Figure 4-16, is different from the sensor configuration shown in Figure 4-2.

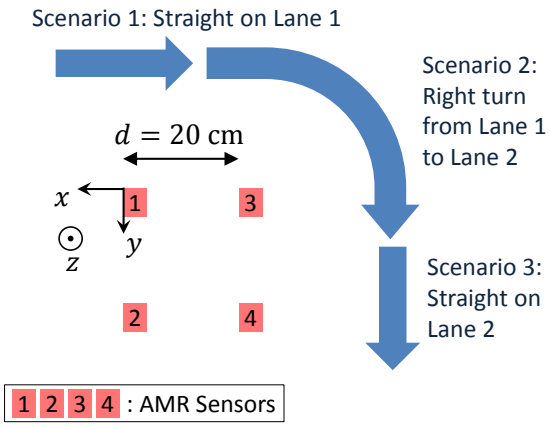


Figure 4-16. Magnetic sensors configuration for right turn detection system.

### 4.7.1. Method A

As mentioned in Section 4.4, it can be shown through both analytical modeling and experimental measurements that the magnetic field intensity around a vehicle has a relation that approximately varies as $1/x$ with distance, where $x$ is the lateral distance from the vehicle. This phenomenon was used to reject the traffic in the nonadjacent lane that creates large enough signals to affect the sensors. In a right turn detection system, generally the traffic going straight in lanes 1 and 2 will pass at a larger lateral distance from the sensors than the vehicle making a right turn. Therefore, for the magnetic sensors 2 and 3, we expect that the ratio $r = B2_{max}/B3_{max}$ be closer to 1 during Scenarios 1 and 3 comparing to Scenario 2 shown in Figure 4-16.

### 4.7.2. Method B

Using all the information from all the four magnetic sensors, the following is expected when integrating the signals of each detected vehicle:

Scenario 1: $$B1_{int} \cong B3_{int} > B2_{int} \cong B4_{int}, \tag{4-17}$$

Scenario 2: $B3_{int} > B1_{int} \cong B4_{int} > B2_{int}$, (4-18)

Scenario 3: $B3_{int} \cong B4_{int} > B1_{int} \cong B2_{int}$. (4-19)

Now consider 4 points in a 3-D space located at $(0,0,B1_{int})$, $(0,d,B2_{int})$, $(-d,0,B3_{int})$ and $(-d,d,B4_{int})$ where $x$ and $y$ of each point shows the position of the magnetic sensors with respect to the origin (sensor 1) and $z$ shows the value of $Bi_{int}$ for each sensor. Next, we fit a plane with normal vector $\hat{n}$ to these four points and define $\hat{n}_p$ as the projection of $\hat{n}$ into $XY$ plane, and $\gamma$ as the angle between $\hat{n}_p$ and the $X$-axis. It is expected that for Scenarios 1, 2 and 3, the angle $\gamma$ will be close to 90°, 45° and 0°, respectively. The equation of a plane is:

$$\hat{n} \,.\, (p - p_0) = 0, \tag{4-20}$$

where $p_0$ is the position of a known point on the plane, $\hat{n}$ is a nonzero vector normal to the plane and $p$ is a point on the plane. Expanding this equation we get:

$$n_x(x - x_0) + n_y(y - y_0) + n_z(z - z_0) = 0 \quad \Longrightarrow \quad ax + by + c = z, \tag{4-21}$$

where

$$a = -\frac{n_x}{n_z}, \qquad b = -\frac{n_y}{n_z}, \qquad c = \frac{n_x x_0 + n_y y_0}{n_z} + z_0. \tag{4-22}$$

Therefore, we get:

$$\gamma = \text{atan}\left(\frac{n_y}{n_x}\right) = \text{atan}\left(\frac{b}{a}\right). \tag{4-23}$$

To obtain $a$, $b$, and $c$, the least squares method can be applied:

$$y = Hx + v \qquad \Longrightarrow \qquad \hat{x} = (H^T H)^{-1} H^T y, \tag{4-24}$$

where

$$x = \begin{bmatrix} a \\ b \\ c \end{bmatrix}, \qquad H = \begin{bmatrix} 0 & 0 & 1 \\ 0 & d & 1 \\ -d & 0 & 1 \\ -d & d & 1 \end{bmatrix}, \qquad y = \begin{bmatrix} B1_{int} \\ B2_{int} \\ B3_{int} \\ B4_{int} \end{bmatrix}, \tag{4-25}$$

and $v$ is the measurement noise.

### 4.7.3. Experimental Results

The Methods A and B were applied to the dataset obtained from the experiments. The dataset was obtained by placing the sensors (with the configuration shown in Figure 4-16) at two different intersections and recording signals from passing vehicles. The experiments were performed during noon hours under clear sky condition. Figure 4-17 shows the results. A support vector machine is used to obtain the classification boundaries [84].

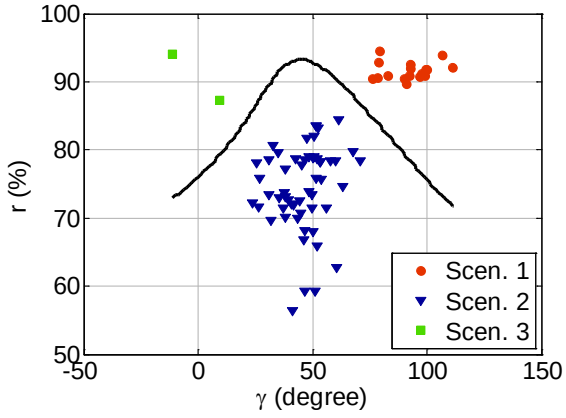


Figure 4-17. Results of applying the support vector machine algorithm to obtain classification boundaries. Scenarios 1, 2 and 3 are straight on lane 1, right turn, and straight on lane 2, respectively.

As seen from Figure 4-17, both methods can be used separately or in combination to reject the straight-driving vehicles that have created a large enough signal to be incorrectly detected as a vehicle making a right turn. If only one of the methods is used,

the separation between the classes will be smaller and the measurements will be less separated. These results show that straight-driving vehicles which have created a large enough signal to be detected by the sensors can be completely excluded reducing the 31% overdetection error to 0%.

## 4.8. Conclusion and Future Work

In this chapter, a portable and low-cost sensor system was developed based on magnetic sensors that can be placed adjacent to the road and be used for vehicle counting, speed measurement, and classification in the lane adjacent to the sensors. The vehicle classification and speed measurement are enabled by the use of multiple spatially separated magnetic sensors. Through experimental data from 188 vehicles, it was shown that the traffic counting accuracy of the system is 99%. A method was also developed to make the system robust to the traffic in the nonadjacent lane. The false calls caused by the traffic in the nonadjacent lane, if uncorrected, can cause 8% detection error. However, using the developed method, the error reduced to 1%.

Speed estimation was performed by placing two magnetic sensors longitudinally apart by 0.9 m and taking the cross-correlation between the signals from the two sensors. Digital signal processing techniques were adopted to reduce the computation effort. The speed estimation method was verified by using a test vehicle equipped with a GPS. Experimental results showed a maximum absolute error of 2.5% error in speed estimates over the speed range of $5 - 27$ m/s $(11 - 60$ mph$)$.

Vehicle classification was performed based on magnetic length and average magnetic height of vehicles in order to classify vehicles into four classes; Class I: sedans, Class II: SUVs, pickups and vans, Class III: Buses and 2-3 axle trucks, and Class IV: articulated buses and 4-6 axle trucks. Magnetic length is estimated by multiplying the

detection time by the estimated speed. It was shown that by only using the magnetic length, it is possible to classify vehicle into Classes III and IV. However, it was not possible to accurately classify vehicles in Classes I and II since they have similar length. Thus, an estimate of the average vertical magnetic height was obtained by using two magnetic sensors vertically spaced by about 0.3 m. A classification accuracy of 83% was achieved by using both the magnetic length and the average magnetic height.

Finally, it was shown that the sensor system can be used to reliably count the number of right turns at an intersection with an accuracy of 95%. The challenge in counting the number of right turns is the false calls created by larger straight-driving vehicles which, if uncorrected, cause 95% overdetection. Two methods were developed based on using two and four magnetic sensors which eliminated this error completely.

A future work of this project is to develop a robust prototype of the system which can be placed adjacent to the road for data collection over days and weeks. One recommended packaging for the sensor system is to package the sensors and electronics in traffic cones. For example, the system shown in Figure 4-2 can be packaged in two cones with sensors 1, 2 and 4 in one cone, and sensor 3 in another cone. The cones can be connected through either wired or wireless connection. For the right turn detection system shown in Figure 4-16, all the four sensors and the electronics can be packaged into one cone.

Another potential future work of this project is to analyze and optimize the power consumption of the sensor system. As an example, one can investigate the possibility of putting microcontrollers into sleep mode between detections. Similarly, since the sensors are placed adjacent to the road, use of solar cells as one of the sources of power can be investigated.

# 5. Thesis Summary

This thesis proposed a new fundamental position sensing principle based on the use of the inherent magnetic fields of ferromagnetic objects. For an individual ferromagnetic object, using (a) a mathematical model of the magnetic field around the object, (b) measurements of magnetic field at a few discrete locations around the object with inexpensive magnetic sensors, and (c) adaptive estimation techniques, the position of the ferromagnetic object can be accurately estimated. Three major applications were pursued in this thesis to show the applicability of the proposed sensing principle:

1) Imminent automotive crash detection (Chapter 2),
2) Non-intrusive Piston Position Estimation (Chapter 3), and
3) Portable road-side sensor for vehicle counting, speed measurement and classification (Chapter 4).

The work on imminent automotive crash detection was motivated by the need to develop an inexpensive sensor system for an automobile that can predict an imminent collision with another vehicle just before the collision occurs. The prediction needs to occur at least 100 ms before the collision so that there is adequate time to initiate active occupant protection measures during the crash. Examples of simple occupant protection measures that can be initiated based on this prediction include pre-tightening of seat belts and gentler inflation of air bags. In addition, active crush space enhancement systems such as active bumpers and rapid active seat back control can be utilized.

A vehicle is made of many metallic parts (such as chassis, engine, and body) which have a residual magnetic field and/or get magnetized in the Earth's magnetic field. These

magnetic fields create a net magnetic field for the whole vehicle which varies as a function of position around the vehicle. Thus, the proposed position sensing principle was utilized in order to find a vehicle's relative position, velocity and orientation with respect to another vehicle so as to predict an unavoidable crash.

As the first step, the problem of 1-D vehicle position estimation was considered. Modeling a vehicle as a rectangular block of magnets, a function was analytically derived which models the magnetic field along the longitudinal axis of a vehicle as a function of distance from the vehicle and specific vehicle parameters. The developed model was verified through experiments with several vehicles which showed that the developed model accurately fits the experimental data for many cars. Since the model included specific vehicle parameters not known a priori, an adaptive estimator was developed based on the extended Kalman filter (EKF) and uses measurements from two longitudinally spaced magnetic sensors to estimate both model parameters as well as vehicle distance as a vehicle approaches the sensors. To speed up the convergence of the developed estimator necessary for imminent crash detection, sensor fusion with a sonar sensor was used resulting in a new estimator. Several experiments with vehicles and laboratory test rigs were performed to verify the performance of the estimator. The position estimation accuracy was shown to be within 1.3 cm.

Next, the problem of 2-D vehicle position estimation was considered. The magnetic field model developed for 1-D position estimation was expanded to model the field over the 2-D plane of a vehicle. With the new model, a new sensor configuration was proposed and an estimator was developed based on the EKF that utilizes magnetic sensors and a custom-designed sonar system measurements to estimate relative 2-D position and orientation of an approaching vehicle in real time. The custom-designed sonar system is capable of measuring both distance to a vehicle as well is its orientation. The estimator was implemented using a PC and embedded microcontrollers for real-time 2-D position estimation. The sensor system achieves a refresh rate of 500 Hz and its

performance was verified through experiments with both a vehicle and laboratory test rigs.

In Chapter 3, the proposed sensing principle was applied to develop a sensor system for non-intrusive estimation of piston position in a number of systems such as engines, hydraulic cylinders, and pneumatic actuators. Piston position measurement is needed for free piston engines and for many other modern engine propulsion technologies. It is also necessary for many control and automation applications in hydraulic systems including hydraulic energy storage systems. As a case study, a sensor system was developed to estimate piston position in a free piston engine. The magnetic field of the piston was modeled as a function of distance along the axis of the motion of the piston. The model includes piston-specific parameters. Different methods were developed to identify the model parameters (offline or in real time) relying only on measurements from two longitudinally spaced magnetic sensors. Therefore, no other reference sensor is required for identification and calibration of the model parameters. The position estimation maximum absolute error was shown to be within $0.4$ mm.

Next, it was shown that for pistons without an inherent magnetic field, a small magnet can be attached to the piston head and the same developed methods be used to design a position estimation system. A pneumatic actuator with a stroke length of $50$ mm and made of paramagnetic materials (e.g. the piston and the piston rod are made of aluminum and type 303 stainless steel, respectively), and thus lacking an inherent magnetic field was used. A small magnet ($5$ mm diameter and $1$ mm thickness) was attached to the piston head to create a change in the magnetic field with the motion of the piston. An experimental setup was developed that included the pneumatic actuator, magnetic sensors, required electronics, and an LVDT used only as ground truth. The position estimation system was implemented based on the developed techniques using a PC and an embedded microcontroller. The magnetic sensors measurements were sent to

the PC and the piston position was estimated in real time. The position estimation maximum absolute error was shown to be within 0.4 mm.

A challenge in the use of magnetic sensors for position estimation is the effect of external disturbances on the magnetic sensors due to unexpected presence of other ferromagnetic objects which may cause inaccuracies in piston position estimation. It was shown that the error can be up to 10 mm depending on the disturbance intensity. A method was proposed to estimate the disturbance on the sensors to be subtracted from their readings. Two different sensor configurations were tested showing the effectiveness of the proposed method. Using an electromagnet to create a step disturbance on the sensors, it was shown that the developed method can reduce the error due to the disturbance to be less than 1 mm in 45 ms.

In Chapter 4, a portable sensor system was developed that can be placed adjacent to a road for vehicle counting, speed measurements, and classification by analyzing the magnetic signatures of passing vehicles. Existing traffic measurement systems based on magnetic sensors require the sensors to be embedded into the pavement. The sensor system developed here, on the other hand, is portable and can be placed on the sidewalk next to the road. Also, it was shown that adopting magnetic field models, some of the performance metrics can be significantly improved compared with the existing systems in which magnetic field models are not used.

The detection rate of the sensor system is 99%, verified through measured data obtained from 188 vehicles and using measurements from one magnetic sensor (sensor 1). The error due to false calls caused by larger vehicles passing in the nonadjacent lane was reduced from $8\% - 15\%$ in existing systems to only 1% using a method based on measurements from sensor 1 and another sensor laterally spaced from sensor 1. The speed of each passing vehicle was obtained by calculating the time delay between the measurements from sensor 1 and another sensor longitudinally spaced from sensor 1. The time delay was calculated by taking the cross-correlation of the signals from the two

sensors. Digital signal processing methods were utilized in order to reduce the number of required calculations for speed estimation. An algorithm to automatically correct for any small misalignment of the sensors was utilized. Using a test vehicle equipped with GPS, the speed estimation maximum absolute error was shown to be 2.5% over the entire speed range of $5 - 27$ m/s ($11 - 60$ mph). Vehicles were classified into four classes; Class I: sedans, Class II: SUVs, pickups and vans, Class III: Buses and 2-3 axle trucks, and Class IV: articulated buses and 4-6 axle trucks. Vehicles in Classes III and IV were accurately classified due to their distinct magnetic lengths which are estimated by the sensor system. However, vehicles in Classes I and II have very similar magnetic lengths and thus, classification becomes more challenging. Therefore, an additional metric was introduced corresponding to the estimated magnetic height of a vehicle obtained from measurements of sensor 1 and another sensor vertically placed from sensor 1. This additional metric improved the classification accuracy of Classes I and II to 83% compared with existing systems with classification accuracy of 63%.

Later in Chapter 4, the four magnetic sensors were used in a specific configuration to develop a new sensor system which can be placed at the corner of an intersection to count the number of right turns in the adjacent lane. Counting the number of vehicles making right turns is used to periodically adjust the traffic signals and is currently performed manually. The detection rate of the sensor system was shown to be 95%. A challenge in counting the number of right turns was the false calls created by larger straight driving vehicles which, if uncorrected, cause 31% overdetection. Two methods were developed based on using signals from two magnetic sensors or four magnetic sensors which eliminated this error completely.

This thesis has resulted in a fundamental new position sensing principle which has a large number of applications. A startup company is being planned to commercialize the technology developed in this research. Provisional and full PCT applications on the inventions in this thesis have been filed by the University of Minnesota.

# References


[1] B. M. Kreutz, "Mediterranean Contributions to the Medieval Mariner's Compass," *Technology and Culture,* pp. 367-383, 1973.

[2] K. Brown, "Animal magnetism guides migration," *Science,* vol. 294, no. 5541, pp. 283-284, 2001.

[3] J. L. Gould and C. G. Gould, *Nature's Compass: The Mystery of Animal Navigation.* Princeton University Press, 2012.

[4] K. J. Lohmann, "Q&A: Animal behaviour: Magnetic-field perception," *Nature,* vol. 464, no. 7292, pp. 1140-1142, 2010.

[5] N. F. Putman, C. S. Endres, C. M. Lohmann and K. J. Lohmann, "Longitude perception and bicoordinate magnetic maps in sea turtles," *Current Biology,* vol. 21, no. 6, pp. 463-466, 2011.

[6] K. J. Lohmann, S. D. Cain, S. A. Dodge and C. M. Lohmann, "Regional magnetic fields as navigational markers for sea turtles," *Science,* vol. 294, no. 5541, pp. 364-366, 2001.

[7] K. J. Lohmann and C. M. Lohmann, "Detection of magnetic field intensity by sea turtles," *Nature,* vol. 380, pp. 5-61, 1996.

[8] T. Alerstam, "Animal behaviour: The lobster navigators," *Nature,* vol. 421, pp. 27-28, 2003.

[9] L. C. Boles and K. J. Lohmann, "True navigation and magnetic maps in spiny lobsters," *Nature,* vol. 421, no. 6918, pp. 60-63, 2003.

[10] L. Q. Wu and J. D. Dickman, "Neural correlates of a magnetic sense," *Science,* vol. 336, no. 6084, pp. 1054-1057, 2012.

[11] C. Walcott and R. P. Green, "Orientation of homing pigeons altered by a change in the direction of an applied magnetic field," *Science,* vol. 184, no. 4133, pp. 180-182, 1974.

[12] B. R. Moore, "Is the homing pigeon's map geomagnetic?" *Nature,* vol. 285, pp. 69-70, 1980.

[13] J. L. Gould, "The map sense of pigeons," *Nature,* vol. 296, pp. 205-211, 1982.

[14] W. Wiltschko and R. Wiltschko, "Magnetic compass of European robins," *Science,* vol. 176, no. 4030, pp. 62-64, 1972.

[15] W. W. Cochran, H. Mouritsen and M. Wikelski, "Migrating songbirds recalibrate their magnetic compass daily from twilight cues," *Science,* vol. 304, no. 5669, pp. 405-408, 2004.

[16] J. B. Phillips, "Two magnetoreception pathways in a migratory salamander," *Science,* vol. 233, no. 4765, pp. 765-767, 1986.

[17] S. T. Emlen, W. Wiltschko, N. J. Demong, R. Wiltschko and S. Bergman, "Magnetic direction finding: evidence for its use in migratory indigo buntings," *Science,* vol. 193, no. 4252, pp. 505-508, 1976.

[18] M. M. Walker, "SENSORY SYSTEMS, PERCEPTION, AND LEARNING | magnetic sense in fishes," in *Encyclopedia of Fish Physiology,* A. P. Farrell, Ed. San Diego: Academic Press, 2011, pp. 726-735.

[19] R. A. Holland, K. Thorup, M. J. Vonhof, W. W. Cochran and M. Wikelski, "Navigation: Bat orientation using Earth's magnetic field," *Nature,* vol. 444, no. 7120, pp. 702-702, 2006.

[20] P. Nemec, J. Altmann, S. Marhold, H. Burda and H. H. Oelschlager, "Neuroanatomy of magnetoreception: the superior colliculus involved in magnetic orientation in a mammal," *Science,* vol. 294, no. 5541, pp. 366-368, 2001.

[21] M. Winklhofer, "An avian magnetometer," *Science,* vol. 336, no. 6084, pp. 991-992, 2012.

[22] H. Mouritsen, "Sensory biology: Search for the compass needles," *Nature,* vol. 484, no. 7394, pp. 320-321, 2012.

[23] P. D. Groves, *Principles of GNSS, Inertial, and Multisensor Integrated Navigation Systems.* Artech House, 2013.

[24] E. Ramsden, *Hall-Effect Sensors: Theory and Application.* Newnes, 2011.

[25] D. J. Sadler and C. H. Ahn, "On-chip eddy current sensor for proximity sensing and crack detection," *Sensors and Actuators A: Physical,* vol. 91, no. 3, pp. 340-345, 2001.

[26] B. Hebert, M. Brule and L. Dessaint, "A high efficiency interface for a biphase incremental encoder with error detection," *IEEE Trans. Ind. Electron.,* vol. 40, no. 1, pp. 155-156, 1993.

[27] S. Y. Yang, M. C. Lee, M. H. Lee and S. Arimoto, "Measuring system for development of stroke-sensing cylinder for automatic excavator," *Industrial Electronics, IEEE Transactions On,* vol. 45, no. 3, pp. 376-384, 1998.

[28] S. Marshall, "Vehicle detection using a magnetic field sensor," *Vehicular Technology, IEEE Transactions On,* vol. 27, no. 2, pp. 65-68, 1978.

[29] S. Y. Cheung, S. Coleri, B. Dundar, S. Ganesh, C. Tan and P. Varaiya, "Traffic measurement and vehicle classification with single magnetic sensor," *Transportation Research Record: Journal of the Transportation Research Board,* vol. 1917, no. 1, pp. 173-181, 2005.

[30] E. Sifuentes, O. Casas and R. Pallas-Areny, "Wireless magnetic sensor node for vehicle detection with optical wake-up," *Sensors Journal, IEEE,* vol. 11, no. 8, pp. 1669-1676, 2011.

[31] Z. Zhang, X. Li, H. Yuan and F. Yu, "A Street Parking System Using Wireless Sensor Networks," *International Journal of Distributed Sensor Networks,* vol. 2013, 2013.

[32] F. Goldenberg, "Geomagnetic navigation beyond the magnetic compass," in *Position, Location, and Navigation Symposium, IEEE/ION,* 2006, pp. 684-694.

[33] S. A. Rahok and O. Koichi, "Odometry correction with localization based on landmarkless magnetic map for navigation system of indoor mobile robot," in *Autonomous Robots and Agents, 2009. ICARA 2009. 4th International Conference On,* 2009, pp. 572-577.

[34] B. Gozick, K. P. Subbu, R. Dantu and T. Maeshiro, "Magnetic maps for indoor navigation," *Instrumentation and Measurement, IEEE Transactions On,* vol. 60, no. 12, pp. 3883-3891, 2011.

[35] M. Angermann, M. Frassl, M. Doniec, B. J. Julian and P. Robertson, "Characterization of the indoor magnetic field for applications in localization and mapping," in *Indoor Positioning and Indoor Navigation (IPIN), 2012 International Conference On,* 2012, pp. 1-9.

[36] C. Zhang, K. Subbu, J. Luo and J. Wu, "GROPING: Geomagnetism and cROwdsensing powered indoor NaviGation," *Mobile Computing, IEEE Transactions On*, vol. PP, *(99)*, pp. 1-1, 2014.

[37] B. D. Cullity and C. D. Graham, *Introduction to Magnetic Materials.* John Wiley & Sons, 2011.

[38] D. J. Griffiths and Reed College, *Introduction to Electrodynamics.* Upper Saddle River, NJ: Prentice Hall, 1999.

[39] W. M. Haynes, *CRC Handbook of Chemistry and Physics.* CRC press, 2012.

[40] P. D. Harvey, *Engineering Properties of Steel.* Metals Park, Ohio: American Society for Metals, 1982.

[41] H. Knoepfel, *Magnetic Fields : A Comprehensive Theoretical Treatise for Practical Use.* New York: Wiley, 2000.

[42] J. G. Buechele and G. A. Cazzell, "Automotive bumper active energy absorption system," U.S. Patent No. 6836717, Dec. 28, 2004 .

[43] D. W. Lee, Z. Ma and N. Kikuchi, "An innovative I-bumper concept for improved crashworthiness of military and commercial vehicles," *SAE Technical Paper 2008-01-0512,* 2008.

[44] L. Jakobsson, B. Lundell, H. Norin and I. Isaksson-Hellman, "WHIPS–Volvo's whiplash protection study," *Accident Analysis & Prevention,* vol. 32, no. 2, pp. 307-319, 2000.

[45] R. Mobus and U. Kolbe, "Multi-target multi-object tracking, sensor fusion of radar and infrared," in *Intelligent Vehicles Symposium, 2004 IEEE,* 2004, pp. 732-737.

[46] S. Matzka and R. Altendorfer, "A comparison of track-to-track fusion algorithms for automotive sensor fusion," in *Multisensor Fusion and Integration for Intelligent Systems.* Springer Berlin Heidelberg, 2009, pp. 69-81.

[47] G. R. Widmann, M. K. Daniels, L. Hamilton, L. Humm, B. Riley, J. K. Schiffmann, D. E. Schnelker and W. H. Wishon, "Comparison of lidar-based and radar-based adaptive cruise control systems," *SAE Technical Paper 2000-01-0345,* 2000.

[48] I. Moon, K. Yi, D. Caveney and J. K. Hedrick, "A multi-target tracking algorithm for application to adaptive cruise control," *Journal of Mechanical Science and Technology,* vol. 19, no. 9, pp. 1742-1752, 2005.

[49] D. Caveney, B. Feldman and J. K. Hedrick, "Comprehensive framework for multisensor multitarget tracking in the adaptive cruise control environment," in *Proceedings of the 6th International Symposium on Advanced Vehicle Control (AVEC)*, 2002, pp. 697-702.

[50] G. Fu, P. Corradi, A. Menciassi and P. Dario, "An integrated triangulation laser scanner for obstacle detection of miniature mobile robots in indoor environment," *Mechatronics, IEEE/ASME Transactions On*, vol. 16, no. 4, pp. 778-783, 2011.

[51] M. J. Caruso and L. S. Withanawasam, "Vehicle detection and compass applications using AMR magnetic sensors," in *Sensors Expo Proceedings*, 1999, pp. 1-13.

[52] Y. Bar-Shalom, X. R. Li and T. Kirubarajan, *Estimation with Applications to Tracking and Navigation: Theory Algorithms and Software.* John Wiley & Sons, 2004.

[53] D. Simon, *Optimal State Estimation: Kalman, H Infinity, and Nonlinear Approaches.* John Wiley & Sons, 2006.

[54] Fatality Analysis Reporting System, NHTSA. [Online]. Available: www.nhtsa.gov/FARS.

[55] S. Julier, J. Uhlmann and H. F. Durrant-Whyte, "A new method for the nonlinear transformation of means and covariances in filters and estimators," *Automatic Control, IEEE Transactions On,* vol. 45, no. 3, pp. 477-482, 2000.

[56] T. Lefebvre, H. Bruyninckx and J. De Schuller, "Comment on "A new method for the nonlinear transformation of means and covariances in filters and estimators" [with authors' reply]," *Automatic Control, IEEE Transactions On,* vol. 47, no. 8, pp. 1406-1409, 2002.

[57] A. Gelb, *Applied Optimal Estimation.* MIT press, 1974.

[58] K. Li, A. Sadighi and Z. Sun, "Active Motion Control of a Hydraulic Free Piston Engine," *Mechatronics, IEEE/ASME Transactions On,* vol. 19, no. 4, pp. 1148-1159, 2014.

[59] T. A. Johansen, O. Egeland, E. A. Johannessen and R. Kvamsdal, "Free-piston diesel engine timing and control-toward electronic cam-and crankshaft," *Control Systems Technology, IEEE Transactions On,* vol. 10, no. 2, pp. 177-190, 2002.

[60] H. Shao, H. Yamamoto, Y. Sakaida, T. Yamaguchi, Y. Yanagisawa and A. Nozue, "Automatic excavation planning of hydraulic excavator," in *Proceedings of the First International Conference on Intelligent Robotics and Applications: Part II,* 2008, pp. 1201-1211.

[61] H. Yamamoto, M. Moteki, H. Shao, T. Ootuki, H. Kanazawa and Y. Tanaka, "Basic technology toward autonomous hydraulic excavator," in *26th International Symposium on Automation and Robotics in Construction (ISARC 2009),* 2009, pp. 288-295.

[62] M. Yasin, R. Grisso and G. Lackas, "Non-contact system for measuring tillage depth," *Computers and Electronics in Agriculture,* vol. 7, no. 2, pp. 133-147, 1992.

[63] S. Malhi and K. Gill, "Placement, rate and source of N, seedrow opener and seeding depth effects on canola production," *Canadian Journal of Plant Science,* vol. 84, no. 3, pp. 719-729, 2004.

[64] A. Ouled Belgacem, M. Neffati, V. Papanastasis and M. Chaieb, "Effects of seed age and seeding depth on growth of Stipa lagascae R. & Sch. seedlings," *Journal of Arid Environments,* vol. 65, no. 4, pp. 682-687, 2006.

[65] D. Karayel and A. Ozmerzi, "Evaluation of three depth-control components on seed placement accuracy and emergence for a precision planter," *Applied Engineering in Agriculture,* vol. 2008, 2008.

[66] P. R. Pagilla, R. V. Dwivedula, Y. Zhu and L. P. Perera, "Periodic tension disturbance attenuation in web process lines using active dancers," *Journal of Dynamic Systems, Measurement, and Control,* vol. 125, no. 3, pp. 361-371, 2003.

[67] K. Ducotey and J. Good, "Predicting traction in web handling," *Journal of Tribology,* vol. 121, no. 3, pp. 618-624, 1999.

[68] V. Gassmann, D. Knittel, P. R. Pagilla and M. Bueno, "Fixed-order tension control in the unwinding section of a web handling system using a pendulum dancer," *Control Systems Technology, IEEE Transactions On,* vol. 20, no. 1, pp. 173-180, 2012.

[69] D. Kuhm and D. Knittel, "New design of robust industrial accumulator for elastic webs," in *18th World Congress of the International Federation of Automatic Control (IFAC),* 2011, pp. 8645-8650.

[70] Digital Signal Processing Tricks. [Online]. Available: http://www.dspguru.com/comp.dsp/tricks.

[71] S. Schaible and J. Shi, "Fractional programming: the sum-of-ratios case," *Optimization Methods and Software,* vol. 18, no. 2, pp. 219-229, 2003.

[72] D. Simon, "Kalman filtering with state constraints: a survey of linear and nonlinear algorithms," *Control Theory & Applications, IET,* vol. 4, no. 8, pp. 1303-1318, 2010.

[73] S. Jeng and S. G. Ritchie, "Real-time vehicle classification using Inductive loop signature data," *Transportation Research Record: Journal of the Transportation Research Board,* vol. 2086, no. 1, pp. 8-22, 2008.

[74] S. Gupte, O. Masoud, R. F. Martin and N. P. Papanikolopoulos, "Detection and classification of vehicles," *Intelligent Transportation Systems, IEEE Transactions On,* vol. 3, no. 1, pp. 37-47, 2002.

[75] H. Cheng, H. Du, L. Hu and C. Glazier, "Vehicle detection and classification using model-based and fuzzy logic approaches," *Transportation Research Record: Journal of the Transportation Research Board,* vol. 1935, no. 1, pp. 154-162, 2005.

[76] J. Medina, M. Chitturi and R. Benekohal, "Effects of fog, snow, and rain on video detection systems at intersections," *Transportation Letters,* vol. 2, no. 1, pp. 1-12, 2010.

[77] S. Kaewkamnerd, J. Chinrungrueng, R. Pongthornseri and S. Dumnin, "Vehicle classification based on magnetic sensor signal," in *Information and Automation (ICIA), 2010 IEEE International Conference On,* 2010, pp. 935-939.

[78] M. Bottero, B. Dalla Chiara and F. Deflorio, "Wireless sensor networks for traffic monitoring in a logistic centre," *Transportation Research Part C: Emerging Technologies,* vol. 26, pp. 99-124, 2013.

[79] Y. He, Y. Du and L. Sun, "Vehicle Classification Method Based on Single-Point Magnetic Sensor," *Procedia-Social and Behavioral Sciences,* vol. 43, pp. 618-627, 2012.

[80] J. Lan and Y. Shi, "Vehicle detection and recognition based on a MEMS magnetic sensor," in *Nano/Micro Engineered and Molecular Systems, 2009 (NEMS 2009), 4th IEEE International Conference On,* 2009, pp. 404-408.

[81] Z. Feng and W. Mingzhe, "A new SVM algorithm and AMR sensor based vehicle classification," in *Intelligent Computation Technology and Automation, 2009. ICICTA'09. Second International Conference On,* 2009, pp. 421-425.

[82] J. C. Medina, A. Hajbabaie and R. (. F. Benekohal, "Detection Performance of Wireless Magnetometers at Signalized Intersection and Railroad Grade Crossing Under Various Weather Conditions," *Transportation Research Record: Journal of the Transportation Research Board*, vol. 2259, no. 1, pp. 233-241, 2011.

[83] F. Ahdi, M. K. Khandani, M. Hamedi and A. Haghani, "Traffic data collection and anonymous vehicle detection using wireless sensor networks," University of Maryland, College Park, MD, 2012.

[84] E. Alpaydin, *Introduction to Machine Learning*. MIT press, 2004.

[85] X. Sun and R. Horowitz, "Set of new traffic-responsive ramp-metering algorithms and microscopic simulation results," *Transportation Research Record: Journal of the Transportation Research Board*, vol. 1959, no. 1, pp. 9-18, 2006.

[86] Y. Ki and D. Baik, "Model for accurate speed measurement using double-loop detectors," *Vehicular Technology, IEEE Transactions On*, vol. 55, no. 4, pp. 1094-1101, 2006.

[87] L. A. Klein, M. K. Mills and D. R. P. Gibson, *Traffic Detector Handbook: Third Edition - Volume II*. McLean, VA: Federal Highway Administration, 2006.

[88] VSN240 Wireless Flush-Mount Sensor. [Online]. Available: http://www.sensysnetworks.com/downloads/data-sheets/Datasheet-VSN240-Sensor.pdf.

[89] D. Nan, T. Guozhen, M. Honglian, L. Mingwen and S. Yao, "Low-power vehicle speed estimation algorithm based on wsn," in *Intelligent Transportation Systems, 2008 (ITSC 2008), 11th International IEEE Conference On*, 2008, pp. 1015-1020.

[90] L. Zhang, R. Wang and L. Cui, "Real- time Traffic Monitoring with Magnetic Sensor Networks," *Journal of Information Science & Engineering*, vol. 27, no. 4, pp. 1473-1486, 2011.

[91] S. Engelberg, *Digital Signal Processing: An Experimental Approach*. Springer, 2008.

[92] A. V. Oppenheim and A. V. Oppenheim, *Discrete-Time Signal Processing*. Upper Saddle River, N.J: Prentice Hall, 2010.

[93] C. Sun, "An investigation in the use of inductive loop signatures for vehicle classification," California Partners for Advanced Transit and Highways (PATH), 2000.

[94] W. Zhang, G. Tan, H. Shi and M. Lin, "A Distributed Threshold Algorithm for Vehicle Classification Based on Binary Proximity Sensors and Intelligent Neuron Classifier." *Journal of Information Science & Engineering*, vol. 26, no. 3, pp. 769-783, 2010.

[95] I. Jolevski, A. Markoski and R. Pasic, "Smart vehicle sensing and classification node with energy aware vehicle classification algorithm," in *Proceedings of the Information Technology Interfaces (ITI) 2011, 33rd International Conference On*, 2011, pp. 409-414.